HAL
open science

Crowd motion modeling by conservation laws

Matthias Mimault

To cite this version:

Matthias Mimault. Crowd motion modeling by conservation laws. General Mathematics [math.GM]. Université Nice Sophia Antipolis, 2015. English. NNT : 2015NICE4102 . tel-01291658

HAL Id: tel-01291658

https://theses.hal.science/tel-01291658v1

Submitted on 21 Mar 2016

HAL is a multi-disciplinary open access archive for the deposit and dissemination of scientific research documents, whether they are published or not. The documents may come from teaching and research institutions in France or abroad, or from public or private research centers.

L'archive ouverte pluridisciplinaire **HAL**, est destinée au dépôt et à la diffusion de documents scientifiques de niveau recherche, publiés ou non, émanant des établissements d'enseignement et de recherche français ou étrangers, des laboratoires publics ou privés.

Université de Nice-Sophia Antipolis - UFR Sciences

École Doctorale en Sciences Fondamentales et Appliquées

THÈSE

Pour obtenir le titre de

Docteur en Sciences

de l'Université de Nice-Sophia Antipolis

Spécialité : Mathématiques Appliquées

Présentée et soutenue par

Matthias Mimault

Lois de conservation pour la modélisation des mouvements de foule

(Crowd motion modeling by conservation laws)

Thèse dirigée par Paola Goatin
soutenue le 14 décembre 2015

JURY :

Mme. Paola GOATIN,	DR HDR	Dir. de thèse
Mme. Simone GÖTTLICH,	Professeur, U. de Mannheim	Rapporteur
M. Boniface NKONGA,	Professeur, UNS	Examinateur
M. Nicolas SEGUIN,	MDC HDR, UMPC	Rapporteur
M. Andrea TOSIN,	Ass. Pr., Polytech. de Turin	Examinateur

Aux parents, aux amis,
et à une certaine idée de l'Homme

Remerciements

Mes remerciements vont d'abord à Paola Goatin, pour m'avoir accompagné durant ces trois années et demi passées à sortir les mathématiques d'une problématique captivante. J'ai ainsi pu découvrir touche par touche le métier difficile mais passionnant de chercheur, et eu l'opportunité de voyager pour découvrir d'autres gens en d'autres lieux. Merci à Nicolas Seguin et Simone Göttlich pour avoir relu mon manuscrit et permis de soutenir ma thèse. Merci encore à Simone pour m'avoir accueilli à Mannheim pour travailler et approfondir mes sujets. Je remercie aussi Boniface Nkonga et Andrea Tosin pour avoir accepté de faire partie de mon jury.

Merci aux membres de l'équipe ACUMES, Abderrahmane, Guillaume, Jean-Antoine et Régis de m'avoir répondu quand j'avais des questions et permis de participer activement à la vie scientifique du centre. Merci aussi à Agnès, Jean-Luc, Ornella et Philippe, mais aussi Karim et Rutger, pour m'avoir permis de m'investir dans la vie associative du centre et monter différentes activités et expériences. Merci à Clausewitz, Sun Tzu, Paul Halmos et Nadège pour leurs pertinents conseils et remarques, qui m'ont permis de repenser ma manière d'écrire et travailler.

Merci à Guillaume et Romuald pour leurs bêtises et la mienne, pour les méthas, les karaokés et les jeux. Ça aide bien. Merci aussi à Elise et José, compagnons d'infortune doctorale. On se serre les coudes ! On rit, on pleure et on boit du café (ou du coca). Merci aussi à tout ceux avec qui j'ai partagé ce café, avant que la cafetière ne rende l'âme, Aekta, Boutheina, Camilla, Daigo (どうもありがとう), Enrico, Fatima, Jennifer, Maria Laura, Sheila et Stefano. Merci aussi à Simon pour le gros tas de bouquins et de .mp3 qu'il m'a suggéré en me les collant dans les mains.

Merci aussi à ma famille, parents, grand-parents, frères et soeurs pour leur constant soutien et la quantité astronomique de nourriture qui en découle. Je suis heureux d'être un genre de fierté locale, même si le rôle est parfois difficile à tenir. Je suis heureux d'avoir trouvé en ma maman et ma marraine un auditoire aussi attentif que passionné à l'idée du paradoxe de Braess. Merci aussi à mon oncle. Je suis aussi heureux d'annoter quelque part le rapprochement familial de ces derniers mois.

Ces recherches ont été financées par le Conseil Européen de la Recherche via le European Union's Seventh Framework Program (FP/2007-2013) / ERC Grant Agreement n. 257661.

Abstract

In this thesis, we consider nonclassical problems brought out by the macroscopic modeling of pedestrian flow. The first model consists of a conservation law with a discontinuous flux, the second is a mixed hyperbolic-elliptic system of conservation laws and the last one is a nonlocal equation.

In the first chapter, we use the Hughes model in one space-dimension to represent the evacuation of a corridor with two exits. The model couples a conservation law with discontinuous flux to an eikonal equation. The solution of the eikonal equation represents the fastest path to leave the room and their tendency to choose one exit rather the other. The solution is know to show nonclassical behavior at the discontinuity point, and we implement the wave front tracking scheme, treating explicitly the solution behavior at the turning point, to provide a reference solution, which is used to numerically test the convergence of classical finite volume schemes.

In the second chapter, we model the crossing of two groups of pedestrians walking in opposite directions with a system of conservation laws whose flux depends on the two densities. This system loses its hyperbolicity for certain density values, leading to nonclassical solutions hardly captured by classical numerical schemes. We assist to the rising of persistent but bounded oscillations, that lead us to the recast of the problem in the framework of measure-valued solutions.

Finally we study a nonlocal model of pedestrian flow in two space-dimensions. Pedestrians are assumed to deviate from a prescribed trajectory according to an evaluation of the density gradient around them. The model consists of a conservation law whose flux depends on a convolution of the density. This model is used in the optimization of a room evacuation where we minimize the total travel time by controlling the initial distribution of density. We compute approximate solutions with a Lax-Friedrichs type scheme whose convergence to a weak solution is proved. Finally, we solve the optimization problem with a descent method, evaluating the impact of the explicit computation of the cost function gradient with the adjoint state method rather than approximating it with finite differences.

Keywords: *Adjoint state method, Conservation laws, Finite volume methods, Macroscopic models, Mixed hyperbolic-elliptic systems, Nonlocal flux, Pedestrian flow models, Wave front tracking*

Résumé

Les modèles macroscopiques décrivent des phénomènes d'ensemble à partir de quantités conservées. Ainsi, comme les modèles hydrodynamiques pour la mécanique des fluides, on étudie les mouvements d'un trafic à partir de l'évolution de la densité.
Helbing proposa en 1992 [49] une première explication macroscopique du comportement des piétons basée sur la théorie cinétique des gaz développée par Boltzmann. Il calculait ainsi la *vitesse désirée* d'un piéton en fonction d'une reformulation *sociale* de la pression et de la température. Plus tard, en 2002, devant les incidents récurrents se déroulant au pont de Jamaraat à la Mecque, Hughes proposa un modèle [56] incorporant les mécaniques décrites par Lighthill, Witham et Richards [66, 76] dans leur modèle macroscopique de trafic routier. Il y inclut le mouvement dans les deux dimensions de l'espace, la notion d'*objectif* et la *stratégie* mise en place pour l'atteindre.

Dans cette thèse, on étudiera des lois de conservation avec des flux non-classiques. Dans la première partie, on décrira l'implémentation de la méthode de suivi des fronts pour le modèle de Hughes en 1D. Ensuite on étudiera le caractère mixte hyperbolique-elliptique d'un système de lois de conservation décrivant le croisement de deux groupes de piétons marchant dans une direction opposée. Dans la dernière partie, un modèle non-local de trafic piétonnier décrira comment les piétons dévient d'une trajectoire prédéfinie selon la perception de la densité qu'ils ont autour d'eux.

On décrira dans la première partie l'évacuation d'un couloir avec deux sorties à l'aide du modèle de Hughes 1D. Il consiste en une loi de conservation dont le flux comporte une discontinuité mobile dépendant de la distribution de la densité.
On considère le couplage suivant

$$u_t - \left(uv(u) \frac{\phi_x}{|\phi_x|} \right)_x = 0, \tag{1a}$$

$$|\phi_x| = c(u), \tag{1b}$$

où $t \geq 0$, $x \in]-1, 1[$, $u = u(t, x) \in [0, 1[$ est la densité normalisée et $v(u) = 1 - u$ la vitesse moyenne des piétons. On définit le flux $f(u) = uv(u) = u(1-u)$ dont la direction dépendra de ϕ, solution de l'équation eikonale (1b). $c : [0, 1[\mapsto [1, +\infty[$ est une *fonction coût*, qui pondère la distance que parcourent les piétons par la densité. C'est une fonction régulière telle que $c(0) = 1$ et $c'(u) \geq 0$. Un choix courant dans la littérature est

$$c(u) = \frac{1}{v(u)},$$

voir [23, 35, 56, 57].
On complète les équations (1) avec la distribution initiale $u(0, \cdot) = u^0 \in \mathbf{BV}([0, 1])$ et les conditions aux limites faibles suivantes

$$u(t, \pm 1) = 0, \tag{2a}$$

$$\phi(t, \pm 1) = 0. \tag{2b}$$

Une des hypothèses principales du modèle de Hughes postule que chaque piéton connait l'exacte distribution de densité dans le domaine afin de définir son trajet. [2] montra que pour

le cas 1D la solution de l'équation eikonale donne deux sous-domaines convexes orientant la vitesse vers la gauche et vers la droite, séparés par le *point de rebroussement* ξ. On assure ainsi qu'aucun piéton ne va à l'encontre de la vitesse choisie par son groupe, à moins que sa trajectoire ne croise celle de ξ.
Ainsi l'unique solution de viscosité au problème de Dirichlet (1b,2b) est donnée par

$$\phi(t,x) = \begin{cases} \int_{-1}^{x} c(u(t,y))\,\mathrm{d}y & \text{si} \quad -1 \le x \le \xi(t), \\ \int_{x}^{1} c(u(t,y))\,\mathrm{d}y & \text{si} \quad \xi(t) \le x \le 1, \end{cases}$$

où $\xi \in \Omega$ est implicitement défini par l'identité

$$\int_{-1}^{\xi(t)} c(u(t,y))\,\mathrm{d}y = \int_{\xi(t)}^{1} c(u(t,y))\,\mathrm{d}y.$$

Au final, l'équation (1a) peut être réécrite comme une loi de conservation scalaire avec un flux discontinu dépendant du temps, de l'espace et de la densité

$$u_t + F(t,x,u)_x = 0,$$

où $F(t,x,u) = \operatorname{sgn}(x - \xi(t))\, f(u)$.
La position de la discontinuité n'est pas déterminée a priori, car elle dépend non-localement de la densité. Ainsi les résultats de convergence connus pour cette configuration ne s'appliquent pas ici. Le problème (1) présente le couplage non-trivial d'une loi de conservation avec une équation eikonale, ce qui pose des questions concernant l'existence, l'unicité, l'approximation et la construction de solutions. Quelques résultats préliminaires ont été obtenus dans [2, 39], où l'on a discuté de la notion de solution entropique faible pour ce problème et produit un algorithme pour construire une solution autosimilaire locale en temps dans un voisinage du point de rebroussement.
On s'intéresse ici au calcul numérique d'une solution faible pour le problème non-régularisé. On apportera des preuves numériques que l'application directe de schémas de volumes finis permettrait de recouvrer les solutions exactes. Comme celles-ci ne sont pas connues explicitement, on comparera les résultats des schémas de volumes finis avec une approximation précise de la solution faible entropique obtenue via la méthode de suivi des fronts, voir [54]. Ce schéma capture par construction le comportement de la solution au voisinage de ξ.

Dans le chapitre suivant, on considère un système de lois de conservation de type mixte hyperbolique-elliptique décrivant le croisement de deux groupes de personnes se déplaçant en sens opposé dans un couloir. Le flux $\mathbf{F}$ dépend de chaque densité. On a ainsi

$$\begin{aligned} (u_1)_t + f(u_1,u_2)_x &= 0, \\ (u_2)_t - f(u_2,u_1)_x &= 0. \end{aligned} \tag{3}$$

avec $t \ge 0$ et $x \in \mathbb{R}$. Les densités $U = (u_1, u_2)$ prennent leurs valeurs dans

$$\Omega_u = \left\{ (u_1,u_2) \in \mathbb{R}^2 : u_1 \ge 0,\ u_2 \ge 0,\ u_1 + u_2 \le 1 \right\}$$

et le flux est donné par

$$\mathbf{F}(U) = \begin{pmatrix} f(u_1,u_2) \\ -f(u_2,u_1) \end{pmatrix}$$

où $f(a,b) = a(1-a-b)$.
On remarque de fortes oscillations bornées lors de la discrétisation du système (3) par des schémas volumes finis classiques. [15] a suggéré que ce phénomène soit relié à la formation de groupes lors des croisements de foules.
Les valeurs propres du système (3) deviennent complexes pour les valeurs d'un sous-ensemble de Ω_u, noté $\mathcal{E}$. On retrouve ainsi trois zones véritablement nonlinéaires qui sont séparées par $\mathcal{E}$. Pour des densités initiales se trouvant dans les régions hyperboliques, la solution évolue de manière similaire à un système hyperbolique classique. Mais si la donnée initiale se trouve trop près du bord du sous-domaine, ou séparée dans des sous-domaines différents, plusieurs chocs non-classiques se forment. [67] établit un critère géométrique basé sur l'intersections des courbes de Lax et la vitesse des chocs pour sélectionner les solutions acceptables. L'unicité de la solution reste cependant un problème ouvert.
On s'intéressera donc en particulier aux propriétés des solutions du problème de Riemann associé à (3) avec

$$U^0(x) = \begin{cases} U_L = (u_{L,1}, u_{L,2}) & \text{si} \quad x < 0, \\ U_R = (u_{R,1}, u_{R,2}) & \text{si} \quad x \geq 0. \end{cases}$$

afin d'étudier les conditions d'apparitions des approximations oscillantes. Elles conduiront à la reformulation de la solution du problème dans le cadre des *mesures de Young*. On considèrera les oscillations des approximations sous l'angle des *mesures de probabilité*, par le calcul de la moyenne de la densité et du flux, voir [36, 81]. Dans [43], les auteurs fournirent une formule explicite pour calculer la mesure de probabilité associée à une approximation de solution dans le cas du problème de Riemann.

Dans la dernière partie, on considèrera un système non-local de lois conservation, où les piétons suivent une trajectoire prédéfinie mais dévient selon la répartition de densité autour d'eux. On cherchera ensuite à optimiser l'évacuation d'une salle en contrôlant la distribution initiale de piétons. On considère le système général de N équations de continuité sur $\Omega \subset \mathbb{R}^2$

$$U_t + \mathrm{div}_{x,y} F\left(t, x, y, U, U * \eta\right) = 0 \tag{4}$$

Le flux F dépend de manière non-locale de la distribution de densité $U \in \mathbb{R}^N$, avec $t \geq 0$, $(x,y) \in \mathbb{R}^2$, $\eta : \mathbb{R}^2 \mapsto \mathbb{R}^{m \times N}$ et le couplage se fait avec le terme non-local $\eta * U$ donné pour $\ell = 1, ..., m$ par

$$(\eta * U)_\ell(t,x,y) = \int_{\mathbb{R}^2} \sum_{k=1}^{N} \eta^{\ell,k}(x-x', y-y') U^k(t,x',y') \, \mathrm{d}x' \mathrm{d}y'$$

Les modèles non-locaux de trafic piétonnier sont remarquables pour former spontanément des files de piétons, mais aussi pour perdre plusieurs propriétés usuelles des modèles macroscopiques. Dans [28], les auteurs ont remarqué la perte du principe du maximum et le fait que la non-localité permet virtuellement aux informations de voyager à une vitesse infinie. Le caractère bien posé du problème de Cauchy a été statué dans [26, 28, 29] avec une étude poussée de la dépendance continue de la solution par rapport à la donnée initiale et sa stabilité par rapport au champ vectoriel.
On s'intéresse particulièrement à la représentation de l'évacuation des piétons à l'aide d'une loi de conservation dont la non-localité du flux prend la forme d'une déviation de la trajectoire

du piéton. Celui-ci décide d'éviter les fortes densités en fonction de la perception qu'il a des piétons autour de lui. On se concentre sur l'équation (4) pour $N = 1$ avec

$$F\left(t, x, y, U, U * \eta\right) = \left(V_{\max} U \left(1 - \frac{U}{U_{\max}}\right)\left(\nu + \mathcal{I}(\eta * U)\right)\right).$$

La vitesse scalaire ne dépend uniquement que de la densité locale, avec un maximum $U_{\max} > 0$ et la vitesse maximale $V_{\max} > 0$. Le champ vectoriel $\nu(x, y)$ représente la direction privilégiée des piétons et $\mathcal{I}$ est une déviation dûe à la *densité perçue* telle que

$$\mathcal{I}(\eta * U) = -\varepsilon \frac{\nabla(\eta * U)}{\sqrt{1 + \|\nabla(\eta * U)\|^2}},$$

avec $\varepsilon > 0$ et $\|\cdot\|$ la norme Euclidienne pour $\mathbb{R}^2$. η est un noyau de convolution lisse, non-négatif et à support compact qui représente la manière dont les piétons évaluent la densité autour d'eux pour ajuster leur trajectoire, par exemple

$$\eta(x, y) = \left(1 - \left(\frac{x}{r}\right)^2\right)^3 \left(1 - \left(\frac{y}{r}\right)^2\right)^3, \; r > 0.$$

Le domaine se partitionne en Ω_{ped} où les piétons se déplaçent et Ω_{wall} où ils ne peuvent pas. On définit $\Gamma_w = \partial\Omega_{\text{wall}} \cap \partial\Omega_{\text{ped}}$ comme l'interface entre les murs et la zone pédestre, et $\Gamma_o = \partial\Omega \cap \partial\Omega_{\text{ped}}$ la sortie. On complète (4) avec les conditions de bord suivantes

$$\begin{cases} U(t, x, y) = 0, & \forall\,(x, y) \in \Gamma_o, \quad \forall\, t \geq 0, \\ \langle F, \vec{n} \rangle = 0, & \forall\,(x, y) \in \Gamma_w, \quad \forall\, t \geq 0. \end{cases}$$

On cherchera à optimiser l'évacuation de la salle en contrôlant la donnée initiale sur $\Omega_{\text{ctrl}} \subset \Omega_{\text{ped}}$. On pose ainsi les conditions sur la donnée initiale $U(0, x, y) = U^0(x, y) \in \mathbb{L}^\infty(\mathbb{R}^2; \mathbb{R})$

$$\begin{cases} 0 \leq U^0(x, y) \leq U_{\max}, & \forall\,(x, y) \in \Omega_{\text{ctrl}}, \\ \int_{\Omega_{\text{ctrl}}} U^0(x, y)\,\mathrm{d}x\,\mathrm{d}y = U_{\text{init}} & \\ U^0(x, y) = 0 & \forall\,(x, y) \notin \Omega_{\text{ctrl}} \end{cases}$$

où U_{init} est une constante positive fixée représentant le nombre d'individus. Le problème d'optimisation consistera à minimiser le temps total de parcours $\mathcal{J}$

$$\min_{U^0 \in \mathbf{L}^\infty(\Omega_{\text{ctrl}}; [0, U_{\max}])} \mathcal{J}(U^0) = \min_{U^0 \in \mathbf{L}^\infty(\Omega_{\text{ctrl}}; [0, U_{\max}])} \int_{\mathbb{R}^+} \int_{\Omega} U_{U^0}(t, x, y)\,\mathrm{d}t\,\mathrm{d}x\,\mathrm{d}y$$

où U_{U^0} représente la solution associée à la donnée initiale U^0, que l'on contrôle dans Ω_{ctrl}.

Contents

Introduction **1**

1 The one dimensional Hughes' model applied to a corridor evacuation **9**
1.1 Introduction . . . 10
1.2 Analytical study . . . 12
1.2.1 Basic properties of solutions . . . 12
1.2.2 The Riemann solver at the turning point . . . 13
1.3 Numerical Study . . . 17
1.3.1 Wave front tracking . . . 17
1.3.2 Finite volume schemes . . . 20
1.4 Numerical convergence . . . 22
1.4.1 Data processing . . . 22
1.4.2 Convergence of the wave front tracking . . . 22
1.4.3 Convergence of finite volume schemes . . . 24
1.4.4 More general initial data . . . 25
1.5 Numerical application: a pedestrian tracking . . . 27
1.5.1 Algorithm . . . 27
1.5.2 Results . . . 28
1.6 Conclusion . . . 28

2 A mixed-type system of conservation laws modeling crossing flows of pedestrians **31**
2.1 Introduction . . . 32
2.2 Analytical study . . . 33
2.2.1 Rarefaction waves . . . 35
2.2.2 Shocks . . . 36
2.2.3 Fognals, umbilic points and crossing shocks . . . 37
2.3 Solutions of the Riemann problem . . . 38
2.3.1 Description of the solution . . . 38
2.3.2 Partial analytical proofs . . . 42
2.4 Numerical Study . . . 50
2.5 Numerical results . . . 54
2.5.1 Distributional solutions . . . 54
2.5.2 Measure-valued solutions . . . 59
2.6 Conclusion . . . 65

3 Finite volume approximation of a nonlocal model of pedestrian traffic applied to the initial data optimization of an evacuation problem. 67
3.1 Introduction . . . 68
3.2 Approximation of the solutions with a finite volume scheme . . . 68
3.2.1 The algorithm . . . 68
3.2.2 Existence of solutions . . . 70
3.2.3 Numerical convergence of the numerical scheme . . . 74
3.3 Optimization of the initial data for an evacuation problem . . . 75
3.3.1 Settings . . . 75
3.3.2 Formulation of the optimization problem . . . 78
3.3.3 Discrete formulation . . . 78
3.3.4 Formulation of the cost function gradient . . . 78
3.3.5 Numerical validation of the gradient . . . 80
3.3.6 Optimization results . . . 82
3.4 Conclusion . . . 88

Conclusion and perspectives 91

Conclusion et perspectives 93

A Proofs of technical lemmas 95

B Lagrange multipliers computation 107

C Generating the velocity vector field using the eikonal equation 111
C.1 Numerical method . . . 111
C.2 Convergence of the numerical scheme . . . 112
C.3 Computing the discomfort vector field . . . 114

D Anisotropic convolution kernel 117
D.1 Numerical integrations . . . 117

List of Figures

1.1 Wave front tracking solution of (1.8) with $u^0(x) = 0$ for $x \in]-1,0[$ and $u^0(x) = 0.9$ for $x \in]0,1[$, and mesh sizes $\Delta u = 2^{-4}$ (left) and $\Delta u = 2^{-10}$ (right). The white curve is the trajectory $x = \xi(t)$. 18

1.2 Density profile at time $t = 0.8$ with initial density $u^0(x) = 0$ for $x \in]-1,0[$ and $u^0(x) = 0.9$ for $x \in]0,1[$, computed using wave front tracking scheme with mesh sizes $\Delta u = 2^{-4}$ (left) and $\Delta u = 2^{-10}$ (right). The position of the turning point $x = \xi(t)$ coincides with the first downward jump discontinuity from the left. 18

1.3 When a choc appears at the turning point, the total variation increases. Here $TV(u_{n+1}) = TV(u_n) + 2(u_2 - u_1)$ 19

1.4 Definition of $\tilde{u}_{WFT}$ at the point (t_{FV}, x_{FV}) of the reference cartesian grid: after finding the last interaction time $t^m \leq t_{VF}$ in u_{WFT}, one has to compare the positions of the corresponding interfaces $x_i(t_{FV}) = x_i^m + s_i(t_{FV} - t^m)$ with respect to x_{FV}, where $s_i = 1 - u_i - u_{i+1}$ are the speeds of the wave fronts. Here $\tilde{u}_{WFT} = u_2^m = u_2^{m-1}$. 23

1.5 $\mathbf{L_1}$-error ϵ_ν between two subsequent discretization meshes $2^{-\nu}$ and $2^{-\nu-1}$, for $\nu = 5, \ldots, 12$, corresponding to the initial datum given by (1.31). 24

1.6 $\mathbf{L_1}$-norm of the error in logarithmic scale for mesh sizes $\Delta x = 1/50, \ldots, 1/1500$, for Godunov and Rusanov schemes corresponding to the initial datum given by (1.31). 25

1.7 Zoom of the numerical approximations in a neighborhood of the turning point $x = \xi(t)$ for the initial datum (1.31) at time $t = 0.8$. The wave front tracking profile is given by the mesh $\Delta u = 2^{-10}$, and the finite volume space step is $\Delta x = 1/1500$. 25

1.8 Wave front tracking scheme for u^0 given by (1.32) with $\Delta u = 2^{-10}$. 26

1.9 Godunov scheme for u^0 given by (1.32) with $\Delta x = 10^{-3}$. 26

1.10 Rusanov schemes for u^0 given by (1.32) with $\Delta x = 10^{-3}$. 26

1.11 Representation of the different parameters used in the algorithm. Flux direction 27

1.12 Trajectory in black during the evolution of 1.31 and its position in red circle on the density profile of a single pedestrian starting at $x_0 = 0.4$. The simulation parameters are $u^0(x) = 0$ for $x \in]-1,0[$ and $u^0(x) = 0.9$ for $x \in]0,1[$, $t = 1.2$ on right and $\Delta x = 0.005$. 29

2.1 The triangular domain Ω_u, the elliptic region $\mathcal{E}$ and the sides L, M_1 and M_2. . 34

2.2 1-rarefaction curves (dark lines), 2-rarefaction curves (fair lines) and fognals (dashed lines). 35
2.3 Eigenvector fields of r_1 (left) and r_2 (right) outside the elliptic region $\mathcal{E}$, oriented so that $\nabla\lambda_i \cdot r_i \geq 0$. 36
2.4 Hugoniot locus for $U_L = (0.2, 0.1)$ in blue, $U_L = (0.8, 0.1)$ in red and $U_L = (0.1, 0.8)$ in green. 37
2.5 The regions Ω_1^a and Ω_1^b in Ω_1. 39
2.6 Hugoniot curve of $\mathcal{H}(0.1, 0.01)$. The curve crosses $\mathcal{E}$ and Ω_2. 39
2.7 Hugoniot curve of $\mathcal{H}(0.55, 0.02)$. The curve crosses Ω_2 with a secondary branch next to $(1, 0)$. 39
2.8 Partitioning of $\Omega_u \setminus \mathcal{E}$, corresponding to the solution of the Riemann problem with $U_L \in \Omega_1/(\Omega_1^a \cup \Omega_1^b)$. 40
2.9 Partitioning of $\Omega_u \setminus \mathcal{E}$, corresponding to the solution of the Riemann problem with $U_L \in \Omega_1^a$. Ω_1^6 is not depicted. 40
2.10 Partitioning of $\Omega_u \setminus \mathcal{E}$, corresponding to the solution of the Riemann problem with $U_L \in \Omega_1^b$. Some regions of Ω_1 are to small to be depicted. 41
2.11 Partitioning of $\Omega_u \setminus \mathcal{E}$, corresponding to the solution of the Riemann problem with $U_L \in \Omega_2$. 42
2.12 Partitioning of $\Omega_u \setminus \mathcal{E}$, corresponding to the solution of the Riemann problem with $U_L \in \Omega_3$. 43
2.13 Density distribution at $T = 0.7$ for $U_L = (0.2, 0.1)$ and $U_R = (0.8, 0)$ 43
2.14 Density distribution at $T = 0.7$ for $U_L = (0.55, 0.02)$ and $U_R = (0.95, 0)$ 44
2.15 Density distribution at $T = 1$ for $U_L = (0.4, 0)$ and $U_R = (0.8, 0.1)$ 45
2.16 Hugoniot curve $\mathcal{H}(0.9, 0)$. 45
2.17 Sign of $P(U_R)$ for $U_L = (0.2, 0)$. Blue is the positive region and red is the negative one. 46
2.18 Density distribution at $T = 1$ for $U_L = (0.8, 0.1)$ and $U_R = (0.8, 0.2)$ 47
2.19 Density distribution at $T = 1$ for $U_L = (0.2, 0.8)$ and $U_R = (0.1, 0.8)$ 47
2.20 Hugoniot curve $\mathcal{H}(0, 0.2)$. 48
2.21 Sign of $P_{\text{bis}}(U_R)$ for $U_L = (0, 0.8)$. Blue is the positive region and red is the negative one. 48
2.22 Density distribution at $T = 1$ for $U_L = (0.1, 0.8)$ and $U_R = (0, 0.4)$ 48
2.23 Density distribution at $T = 1$ for $U_L = (0, 0.7)$ and $U_R = (0.2, 0.1)$ 49
2.24 Solution of (2.1)-(2.4) with $U_L = (0.2, 0.1)$ and $U_R = (0.1, 0.2)$. We observe a classical configuration consisting of a 1-rarefaction and a 2-rarefaction separated by an intermediate state. 54
2.25 Solution of (2.1)-(2.4) with $U_L = (0.2, 0.1)$ and $U_R = (0.1, 0.3)$. We observe a 1-shock, a crossing shock, a contact discontinuity, another crossing shock and a 2-shock. 55
2.26 Solution of (2.1)-(2.4) with $U_L = (0.2, 0.1)$ and $U_R = (0.1, 0.8)$. We observe a 1-shock, a crossing shock, a contact discontinuity and a 2-shock. 55
2.27 Solution of (2.1)-(2.4) with $U_L = (0.2, 0.1)$ and $U_R = (0.85, 0.1)$. We observe a 1-shock, a crossing shock and a 2-shock. 56
2.28 Solution of (2.1)-(2.4) with $U_L = (0.2, 0.1)$ and $U_R = (0.75, 0.1)$. We observe a 1-shock, a crossing shock and a 2-shock. 57
2.29 The Hugoniot locus $\mathcal{H}(U_L)$ for $U_L = (0.4, 0.5) \in \mathcal{E}$. Remark that $\mathcal{H}(U_L) \cap \mathcal{E} = U_L$. 57

2.30 Distributional solution of (2.1)-(2.4) with $U_L = (0.2, 0.1)$ and $U_R = (0.6, 0.1) \in \mathcal{E}$. We observe a 1-shock in the hyperbolic region, followed by a shock connecting the state U_R in the elliptic region. 58
2.31 Distributional solution of (2.1)-(2.4) with $U_L = (0.2, 0.1)$ and $U_R = (0.1, 0.6) \in \mathcal{E}$. We observe a 1-shock, a crossing shock and a contact discontinuity in the hyperbolic region, followed by a shock joining directly U_R. 58
2.32 Distributional solution of (2.1)-(2.4) with initial data in the elliptic region: $U_L = (0.2, 0.5) \in \mathcal{E}$ and $U_R = (0.6, 0.1) \in \mathcal{E}$. We observe two shocks joining U_L and U_R with an intermediate state in the hyperbolic region. 59
2.33 Solution of (2.1)-(2.4) with initial data $U_L = (0.1, 0.2)$ and $U_R = (0.4, 0.5) \in \mathcal{E}$ for $\Delta x = 0.001$ (top) and $\Delta x = 0.0002$ (bottom). 60
2.34 Solution of (2.1)-(2.4) with initial data $U_L = (0.4, 0.5) \in \mathcal{E}$ and $U_R = (0.1, 0.2)$ for $\Delta x = 0.001$ (top) and $\Delta x = 0.0002$ (bottom). 61
2.35 Average (top for density values (2.19) and bottom right for flux (2.20)) and variance (2.21) (bottom left) corresponding to initial data $U_L = (0.1, 0.2)$ and $U_R = (0.4, 0.5)$ and $N = 4 \cdot 10^6$ iterations. 62
2.36 Average (top for density values (2.19) and bottom right for flux (2.20)) and variance (2.21) (bottom left) corresponding to initial data $U_L = (0.4, 0.5)$ and $U_R = (0.1, 0.2)$ and $N = 4 \cdot 10^6$ iterations. 63

3.1 Computational domain for convergence tests. 72
3.2 Solution to (3.1) at times $t = 0$, 2, 4, 16, 18 and 20 with absorbing boundary conditions and space mesh $\Delta x = \Delta y = 0.0125$, $\alpha = \beta = 0.333$ and CFL= 1/7. . 73
3.3 Solution to (3.1) at times $t = 0$, 2, 4, 16, 18 and 20 with zero flux boundary conditions and space mesh $\Delta x = \Delta y = 0.0125$, $\alpha = \beta = 0.333$ and CFL= 1/7. . 73
3.4 Representation of the domain Ω and its different subdivisions. 76
3.5 Control domain Ω_{ctrl} in Ω. 77
3.6 Numerical domain partition in Ω. 77
3.7 The 7×5 domain Ω. 81
3.8 Control domain Ω_{ctrl} in Ω. 81
3.9 Numerical domain partition in Ω. 82
3.10 The domain Ω. 83
3.11 Numerical domain partition on Ω. 83
3.12 Control domain Ω_{ctrl} in Ω with an initial mass of pedestrian $U_{\text{init}} = 20\,000$ ped. 84
3.13 Discomfort region along the walls (unscaled). 84
3.14 Vector field ν on Ω_{ped}. 85
3.15 Optimal solution with 24 control cells and $\varepsilon = 0$ computed with finite differences on the left side and adjoint state method on the right side. 86
3.16 Evolution of J for 24 control cells with $\varepsilon = 0$ for finite differences and adjoint state method. 86
3.17 Optimal solution with 24 control cells and $\varepsilon = 8$ computed with finite differences on the left side and adjoint state method on the right side. 86
3.18 Evolution of J for 24 control cells with $\varepsilon = 8$ for finite differences and adjoint state method. 87
3.19 Optimal solution with 600 control cells and $\varepsilon = 8$ computed with finite differences on the left side and adjoint state method on the right side. 88

3.20 Evolution of J for 600 control cells with $\varepsilon = 8$ for finite differences and adjoint state method. 88

C.1 The domain Ω, with $\Omega_{\text{disc}} \subset \Omega$ and the boundaries Γ_w, Γ_d and Γ_o. 112
C.2 The potential φ on Ω. 113
C.3 The potentials φ_{disc}. 114
C.4 The vector field ν. 115

D.1 Initial data and vector field for all tests. 118
D.2 Kernel for $\bar{\alpha} = \frac{\pi}{8}$ and $\nu_{\text{dir}} = (1, 0)$. 119
D.3 Snapshots of the evacuation for $\bar{\alpha} = \pi$ and $\nu_{\text{dir}} = (1, 0)$ at $T = 10$ and $T = 20$. . 119
D.4 Snapshots of the evacuation for $\bar{\alpha} = \frac{\pi}{4}$ and $\nu_{\text{dir}} = (1, 0)$ at $T = 10$ and $T = 20$. 119
D.5 Snapshots of the evacuation for $\bar{\alpha} = \frac{\pi}{8}$ and $\nu_{\text{dir}} = (1, 0)$ at $T = 10$ and $T = 20$. 120
D.6 Snapshots of the evacuation for $\bar{\alpha} = \frac{\pi}{16}$ and $\nu_{\text{dir}} = (1, 0)$ at $T = 10$ and $T = 20$. 120
D.7 Snapshots of the evacuation for $\bar{\alpha} = \frac{\pi}{8}$ and $\nu_{\text{dir}} = (-1, 0)$ at $T = 10$ and $T = 20$. 120
D.8 Snapshots of the evacuation for $\bar{\alpha} = \frac{\pi}{8}$ and $\nu_{\text{dir}} = (0, -1)$ at $T = 10$ and $T = 20$. 120

List of Tables

1.1 $\mathbf{L_1}$-error ϵ_ν for wave front tracking method between two subsequent discretization meshes $2^{-\nu}$ and $2^{-\nu-1}$. The comparison is done on a cartesian grid with $\Delta x = 10^{-3}$ and $\Delta t = 0.5\Delta x$. 23

1.2 $\mathbf{L_1}$-norm of the error for Godunov and Rusanov schemes for (1.31) depending on the space step Δx, and corresponding convergence order. Above ϵ_X stands for the error of the finite volume scheme and $\gamma_X = \frac{|\ln X|}{|\ln \Delta x|}$ the order of convergence of the flux, with G for the Godunov scheme and R for the Rusanov flux. 24

2.1 Conservation errors (2.22) at time $t = 1$. 64

2.2 Convergence rates (2.23) at time $t = 1$. 64

3.1 Convergence rate γ for the numerical scheme (3.5) on the domain $[0, 10] \times [-1, 1]$ at time $t = 1.0$ for the approximate solutions to the problem (3.1,3.10) with $\lambda_x = \lambda_y = 0.15$ and absorbing boundary conditions. 74

3.2 Convergence rate γ for the scheme (3.5) on the domain $[0, 10] \times [-1, 1]$ at time $t = 1.0$ for the approximate solutions to the problem (3.1,3.10) with $\lambda_x = \lambda_y = 0.15$ and zero flux boundary conditions 75

3.3 Convergence results for the cost function gradient. 81

3.4 Outputs of the optimization procedure for 24 control cells with and $\varepsilon = 0$ for finite differences and adjoint state method. 85

3.5 Outputs of the optimization procedure for 24 control cells with and $\varepsilon = 8$ for finite differences and adjoint state method. 87

3.6 Outputs of the optimization procedure for 600 control cells with and $\varepsilon = 8$ for finite differences and adjoint state method. 89

C.1 Order of convergence of φ. 113

C.2 Order of convergence of $\nabla\varphi$. 113

Introduction

Pedestrian flow models

Nowadays the management of crowds is a complex and crucial task. With the explosion of the urban density and its characterizing demand in transportation, the crowd is all the more a fascinating subject, and its primordial element is *a priori* unpredictable: the man.

It is at the end of the XIXth century that rise up the firsts studies on the crowd. Le Bon [64] studied the crowd not as a mindless and unpredictable aggregate, but as unite entity moved by internal laws of behavior. The crowd was then in the heart of the great events of the XXth century. Alternately courted or oppressed, it was considered with gravity by every totalitarian and democratic regime. Everywhere one wants to see what is behind the alleged stupidity of the crowd.

Helbing proposed in 1992 [49] a macroscopic explanation of the pedestrian behavior based on the gas kinetic described by Boltzmann. He computes the *desired speed* of pedestrians, according to a *pressure* and a *temperature* reformulated to model the tendency that every pedestrian has to variate her speed. It is latter in 2002 and because of the recurring incidents occurring at the Jamaraat Bridge that Hughes proposed a model [56] incorporating the mechanics of the Lighthill-Witham-Richards [66, 76] model of car traffic. He includes the mobility in two dimensions of space, the notion of *objective* and the *strategy* to reach it.

The literature on pedestrian modeling is very extensive. One sorts three major classes of models, each one based on a different scale choice of description. On one side the microscopic approach reduces the crowd to its minimal constituents: the pedestrians. One tracks the trajectory of each walker through *state variables*, usually the speed and the position. One denotes *differential* models such as *force models* [50, 70, 71, 72, 73, 74, 85] using an ordinary differential equations' system to describe the pedestrians' displacement, and *cellular automata* [19] handling preferences and choices of the pedestrians. The precision of the microscopic models allows to describe the *one-to-one* or *one-to-some* interactions between pedestrians, but can be handicapping when the quantity of pedestrians increases. The large amount of particles leads to fastidious calibration of parameters and considerable computation costs.

The mesoscopic representation describes the pedestrians through their statistical distribution. The function of distribution is derived from the Boltzmann *gas kinetic*, and pointed out by Henderson [52]. One can refer to recent models, mixing continuous density with microscopic vector field obtained with *stochastic interactions*, see [11, 33, 37]. With the mesoscopic rep-

resentation, one keeps looking at the crowd interaction through a microscopic point of view without modeling a single pedestrian. However the pedestrians are not in a sufficient number to be statistically independent.

The higher scale of representation of a crowd is the macroscopic modeling. The crowd is considered as a continuous entity through average quantities as density. The individual behavior becomes negligible with respect to the crowd dynamics. The question is then to link the speed to the density through some *fundamental diagram* and to determine the *direction* of the pedestrian flux. In this setting Colombo and Rosini [30] studied the arise of panic by introducing nonconcave fluxes, with a *normal* traffic phase and another corresponding to the *panic* regime. We mention also the work of Maury et al. [68] who projected the flux direction on a space of *acceptable* directions and the Bellomo and Dogbé's one on a *second order model* [12], integrating another equation for the acceleration of the pedestrian. Finally, there exist also *nonlocal* models based on the integration of the density on a neighborhood of each space location, in order to adjust the scalar speed or deviate the direction of motion, see Colombo et al. [26].

Conservation laws

The problems belonging to the macroscopic approach are formulated as *partial differential equations* (PDE). They express the conservation of one or several quantities under the effect of various phenomena, such as the fluid dynamic, the heating transfer or the gravity effect. We focus here on quantities evolving in time from a given initial data.

Typically the mechanics of transport, also called *convection*, are expressed under the form of flux terms. They are characterized by a *closure law*, linking for instance the speed to the density. Formally a system of conservation laws on N quantities is given by

$$\partial_t u_i + \mathrm{div} f_i(t, \mathbf{x}, u) = 0, \ i = 1, ..., N,$$

where f the flux of the model, $t \in \mathbb{R}^+$ is the time variable, $\mathbf{x} \in \mathbb{R}^d$ the space variable in d dimensions (in case of crowd movements we will set $d = 1$ or 2), and $u = (u_1, ...u_N) \in \mathbb{R}^N$ is the vector of unknown.

Frequently an analytical solution can not be computed for a given Cauchy or initial-boundary value problem. Numerical algorithms are then developed to compute approximate solutions. Several methods exist to numerically solve (systems of) conservation laws. In the present thesis, we based our analysis on the *wave front tracking* (WFT) and the *finite volume* (FV) schemes.

The wave front tracking has been proposed by Dafermos [34] in the 70s, and one can refer to Holden and Risebro's book [54] for a detailed study. It consists of exactly solving a 1D evolution problem with a piecewise constant initial datum and a piecewise linear flux. The resulting solution is therefore piecewise constant and its discontinuities constitute the *wave fronts*. They are computed by solving the *Riemann problem* associated at each interface, i.e. defining a *shock* or a *rarefaction* (discrete rarefaction here, namely a *fan*) wave separating two

constant states. Analyzing the behavior of the solution amounts to track those wave fronts, whose trajectories are straight (in the $x - t$ plane). When two wave trajectories cross, the intermediate state disappears and the resolution of a new Riemann problem establishes new wave fronts.

The finite volume method has been elaborated to solve conservation laws thanks to their integral formulation. It has been introduced in the 60s by Tichonov and Samarskii [82]. Its theoretical study has been then widely addressed. One can refer to the books of Eymard, Gallouet and Herbin [40], of Goldewski et Raviart [45] and of Leveque [65]. The method relies on the use of the integral balance of the conserved quantities on small portions of a domain called finite volumes or *cells*. One evaluates then the *numerical fluxes*, which are the exchanges between two cells at regular intervals, the *time steps*, to obtain the evolution of the solution. To guarantee the stability of the scheme, the information must not travel through several cells before the next time step. Usually this condition is usually given by the *Courant-Friedrichs–Lewy* condition, limiting the size of the time step with respect to the space step. Implicit and high order time discretizations as Runge-Kutta can be also used.

Contribution and description of the chapters

The present thesis focuses on the analytical and numerical study of equations appearing in pedestrian modeling. Traffic flow features go beyond the classical framework of conservation laws. In particular, we consider first a flux with a *moving discontinuity*, then a *mixed-type hyperbolic-elliptic* system whose flux depends on the density of two groups of pedestrians, and finally a model with a *nonlocal* flux whose direction depends on a convolution of the density.

The first chapter treats the capture of flux discontinuity in the evacuation using the wave front tracking method. The crowd behavior is described with the one dimensional Hughes' model for a corridor with two exits. The direction of the flux is given by the gradient of the solution of an eikonal equation, with the associated cost function depending on the density. A discontinuity, the *turning point*, arises between the two directions of evacuation. We use the wave front tracking to numerically test the convergence of finite volume schemes for this problem. It provides *reference* solutions because it computes explicitly the solution of the Riemann problem at the turning point. We will see that classical finite volume schemes are able to catch the general behavior of the solution without such treatment.

The next chapter concerns a system of conservation laws of mixed-type modeling a crossing of pedestrian groups walking in opposite directions in a corridor. The flux of the system depends on the density of both groups, and its eigenvalues become complex for densities located in an elliptic region of the *phase space*. The phase space is divided in hyperbolic regions gathered around the elliptic region. We conjecture the solution of the associated Riemann problem, which adds to the classical shocks and rarefactions a third type of wave: the *crossing shocks*. The integration of the model with a classical Lax-Friedrichs type scheme shows persistent but bounded oscillations for initial densities in the elliptic domain. The solution remaining in the physical domain, we investigate then the existence of a solution in the sense of *measures*.

In the third chapter, we address the integration of a *nonlocal* model of pedestrian movement in two dimensions of space for an evacuation optimization. This model assumes that pedestrians adapt their trajectory according to the density around them. Thus the direction of the flux, initially prescribed by the domain geodesics, is *deviated* by a term depending nonlocally on the gradient of the density. In order to solve an optimization problem, we integrate this model with a nonlocal numerical scheme based on Lax-Friedrichs, whose convergence is proved. Then we use it to optimize the evacuation time by controlling the initial distribution of pedestrians by means of a *gradient descent method*. We use the *discrete adjoint state* method to provide the gradient of the associated cost function. We then compare the efficiency of the `fmincon` MATLAB optimization solver with and without providing the computed gradient.

List of publications

During this PhD the following articles have been published:

- P. Goatin, M. Mimault. A wave front tracking algorithm for Hughes model of pedestrian motion, *SIAM Journal on Scientific Computing*, **35**, (2013), B606–B622.
- P. Goatin, M. Mimault. A mixed-system modeling two-directional pedestrian flows, *Mathematical Bioscience and Engineering*, **12(2)**, (2015), 375-392.

The following conference proceedings have been published:

- M. Mimault. Scalar conservation law with discontinuity arising in pedestrian modeling, *ESAIM: PROCEEDINGS*, **45**, (2014), 493-501.
- M. Mimault. Modélisation macroscopique de mouvements de foule. Une application à une foule composée de deux groupes., *Actes du colloque Edp-Normandie*, **Caen 2013**, (2014), 264-271.

Introduction

Modèles de trafic piétonnier

De nos jours la gestion des mouvements de foule est une tâche des plus complexes et cruciales. Avec l'explosion de la densité urbaine et sa demande caractéristique en transport, la foule est d'autant plus un fasciant sujet d'étude que son élément primordial est *a priori* imprévisible : l'homme.

C'est à la fin du XIXème siècle que sont apparus les premières études comportementales sur la foule. Le Bon [64] a étudié la foule non plus comme un agréggat imprévisible et sans intelligence, mais comme une entité unie, mue par ses propres lois internes. La foule se trouve alors au coeur des grands évènements du XXème siècle. Tour à tour courtisée ou oppressée, elle a été considérée avec gravité par chaque régime totalitaire et démocratique. Partout on veut découvrir ce qui se cache derrière la prétendue stupidité de la foule.

Helbing a proposé en 1992 [49] une explication macroscopique du comportement des piétons basée sur la cinétique des gaz décrite par Boltzmann. Il calcule ainsi la *vitesse désirée* des piétons à partir d'une *pression* et d'une *température* reformulée pour expliquer la tendance qu'ont les piétons à faire varier leur vitesse. C'est en 2002 et devant les incidents récurrents du pont de Jaramaat que Hughes a proposé un modèle [56] incorporant la mécanique du modèle de trafic routier de Light-Whitham-Richards [66, 76]. Il y adjoint la mobilité en deux dimensions, la notion d'*objectif* et la *stratégie* pour y parvenir.

La littérature concernant la modélisation des piétons est très étendue. On distingue trois grandes classes de modèles, chacun basé sur une échelle différente de description. On trouve en premier l'approche microscopique, qui réduit la foule à ses constituants minimaux: les piétons. On suit la trajectoire de chaque marcheur au travers de *variables d'état*, usuellement la vitesse et la position. On dénote les *modèles différentiels* tels que les *modèles à force* [50, 70, 71, 72, 73, 74, 85] utilisant un système d'équation différentielles ordinaires pour décrire les déplacements du piéton, et les *automates cellulaires* [19] qui gèrent les préférences et les choix des piétons. La précision des modèles microscopiques permet de décrire des interactions *un-à-un* ou *un-à-plusieurs* entre les piétons, mais peut se révéler handicapante quand la quantité de piétons augmente. Les larges quantités de particules conduisent à de fastidieuses calibrations des paramètres et de considérables coûts en calcul.

La représentation mésoscopique décrit les piétons à l'aide de leur distribution statistique. La fonction de distribution de densité dérive de la *cinétique des gaz* de Boltzmann, et proposée

une première fois par Henderson [52]. On peut se référer à des modèles récents regroupant une densité continue avec un champ de vecteur microscopique obtenu par *interactions stochastiques*, voir [11, 33, 37]. Avec la représentation mésoscopique, on regarde toujours les interactions entre piétons avec un point de vue microscopique, sans pour autant modéliser le moindre piéton. Cependant, les piétons ne sont pas suffisamment nombreux pour être statistiquement indépendants.

Le plus haut de gré de représentation de la foule est la modélisation macroscopique. La foule est considérée comme une entité continue, via des quantités moyennes comme la densité. Le comportement individuel devient négligeable par rapport à la dynamique de la foule. La question est de relier la vitesse de déplacement à la densité via un *diagramme fondamental* et de déterminer la *direction du flux* de piétons. Dans cette configuration, Colombo et Rosini [30] ont étudié l'apparition de panique en introduisant un flux non-concave composé d'une phase *normale*, et d'une autre correspondant à un régime de *panique*. Mentionnons aussi le travail de Maury et al. [68] qui ont projeté la direction du flux dans un espace de *directions acceptables*, et celui de Bellomo et Dogbé sur un *modèle de second ordre* [12] intégrant une équation additionnelle pour l'accélération des piétons. Finalement, il existe aussi des modèles *non-locaux* basés sur l'intégration de la densité sur un voisinage de chaque point de l'espace, de manière à ajuster la vitesse scalaire ou dévier la direction du mouvement, voir [26].

Lois de conservation

Les problèmes tirés de l'approche macroscopique sont donnés sous la forme d'*équations aux dérivées partielles* (PDE). Elles expriment la conservation d'une ou plusieurs quantités sous l'effet de phénomènes variés, tels que la dynamique des fluides, les transferts de chaleur ou l'effet de la gravité. On se concentre ici sur des quantités évoluant dans le temps à partir d'une certaine donnée initiale.

Typiquement, les mécaniques du transport, aussi appelé *convection* s'expriment sous la forme de flux. Ils se caractérisent par une *loi de fermeture*, reliant par exemple la vitesse à la densité. Formellement, un système de N quantités est donné par

$$\partial_t u_i + \operatorname{div} f_i(t, \mathbf{x}, u) = 0, \ i = 1, ..., N,$$

où f est le flux du modèle, $t \in \mathbb{R}^+$ la variable de temps, $\mathbf{x} \in \mathbb{R}^d$ la variable d'espace en d dimensions (dans le cas du mouvement piétonnier, on définit $d = 1$ ou 2) et $u = (u_1, ..., u_N) \in \mathbb{R}^N$ le vecteur des inconnues.

Souvent une solution analytique ne peut être calculée pour un problème donné. Les algorithmes numériques ont été développés pour calculer des solutions approchées. Plusieurs méthodes existent pour résoudre numériquement des (systèmes de) lois de conservation. Dans la présente thèse, on basera notre analyse sur la *méthode de suivi des fronts* (WFT) et les schémas aux *volumes finis* (FV).

La méthode de suivi de fronts a été proposée par Dafermos [34] dans les années 70, et l'on peut se référer au livre de Holden et Risebro [54] pour une étude détaillée. Elle consiste à résoudre

exactement un problème d'évolution en une dimension dont la donnée initiale est constante par morceaux et le flux linéaire par morceaux. La solution résultante est donc aussi constante par morceaux et ses discontinuités constituent les *fronts d'onde*. Ils sont calculés en résolvant le *problème de Riemann* associé à chaque interface, c.a.d. définir une onde de *choc* ou de *détente* (ici une détente discrétisée, un *faisceau*) séparant deux états constants. Analyser le comportement de la solution revient à suivre ces fronts d'onde, dont les trajectoires sont rectilignes (dans le plan $x - t$). Quand deux trajectoires de fronts se croisent, l'état intermédiaire disparait et la résolution d'un nouveau problème de Riemann établit de nouveaux fronts.

La méthode des volumes finis a été élaborée pour résoudre des lois de conservation grâce à leur formulation intégrale. Elle a été introduite dans les années 60 par Tichonov et Samarskii [82]. Son étude théorique a ensuité été largement abordée. On peut se référer aux livres de Eymard, Gallouët et Herbin [40], celui de Goldewski et Raviart [45] et celui de Leveque [65]. Cette méthode repose sur la balance intégrale de quantités conservées sur de petites portions du domaine, appelés volumes finis ou *cellules*. On calcule les *flux numériques*, qui sont les échanges entre deux cellules, à des intervalles réguliers, les *pas de temps*, pour obtenir l'évolution de la solution. Pour garantir la stabilité du schéma, l'information ne doit pas traverser plusieurs cellules avant le prochain pas de temps. Usuellement, cette condition est donnée par la condition de *Courant-Friedrichs-Lewy*, limitant la taille du pas de temps par rapport au pas de temps. On peut aussi utiliser des discrétisations temporelles implicites ou d'ordre supérieur comme Runge-Kutta.

Contribution et description des chapitres

La présente thèse se concentre sur l'étude analytique et numérique d'équations apparaissant dans les modèles de trafic piétonnier. Ces problèmes vont au delà du cadre classique des lois de conservation. En particulier, on considèrera en premier un flux avec une *discontinuité mobile*, ensuite un système de type *mixte hyperbolique-elliptique* dont le flux dépend de la densité de plusieurs groupes de piétons, et finalement un modèle avec un *flux nonlocal* dont la direction dépend d'une convolution de la densité.

Le premier chapitre traite de la capture d'une discontinuité de flux dans une évacuation utilisant le WFT. Le comportement de la foule est décrit par le modèle de Hughes en une dimension pour un couloir avec deux sorties. La direction du flux est donnée par le gradient de la solution d'une équation eikonale dont la fonction coût associée dépend de la densité. Une discontinuité, le *point de rebroussement*, apparait entre les deux directions d'évacuation. On utilisera le WFT pour tester numériquement la convergence de schémas FV classiques pour ce problème. Il fournit une *solution de référence*, en calculant explicitement la solution du problème de Riemann au point de rebroussement. On verra que les schémas FV sont capable de capturer le comportement général de la solution sans recourir à de tels traitements.

Le chapitre suivant concerne un système de lois de conservation de type mixte modélisant le croisement de deux groupes de piétons marchant en direction opposée dans un couloir. Le flux du système dépend de la densité des deux groupes, et ses valeurs propres prennent deviennent complexes pour des densités localisées dans une région elliptique de l'*espace des phases*.

Cet espace est divisé en sous-régions hyperboliques autour d'une sous-région elliptique. On conjecturera la solution du problème de Riemann associé, qui ajoute aux ondes classiques de chocs et de détentes un troisième type : les *chocs de croisement*. L'intégration numérique du modèle se fera par un schéma classique type Lax-Friedrichs retournant des solutions aux oscillations persistantes mais bornées pour des données initiales dans la zone elliptique. La solution restant dans le domaine physique, on étudiera l'existence d'une solution dans le sens de *mesures de probabilités*.

Dans le troisième chapitre, on abordera l'intégration d'un *modèle non-local* de mouvements piétonniers en deux dimension d'espace pour l'optimisation d'une évacuation. Ce modèle suppose que les piétons adaptent leur trajectoire selon le gradient de la densité autour d'eux. Ainsi la direction du flux, initialement dirigée selon les géodésiques du domaine, est *déviée* par un terme dépendant non-localement du gradient de la densité. Afin de résoudre un problème, on intégre le modèle avec un algorithme non-local basé sur Lax-Friedrichs dont la convergence vers une solution faible a été prouvée. Ensuite on l'utilisera pour optimiser le temps d'une évacuation en contrôlant la distribution initiale de piéton au moyen d'une *méthode de descente*. On utilisera la *méthode de l'état adjoint discret* pour calculer le gradient de la fonction coût. On comparera ensuite l'efficacité du solveur de problème d'optimisation de MATLAB `fmincon` avec et sans l'apport du gradient de la fonction coût.

Liste des publications

Durant cette thèse, les articles suivants ont été publiés :

- P. Goatin, M. Mimault. A wave front tracking algorithm for Hughes model of pedestrian motion, *SIAM Journal on Scientific Computing*, **35**, (2013), B606–B622.

- P. Goatin, M. Mimault. A mixed-system modeling two-directional pedestrian flows, *Mathematical Bioscience and Engineering*, **12(2)**, (2015), 375-392.

Les actes de conférences suivants ont été publiés :

- M. Mimault. Scalar conservation law with discontinuity arising in pedestrian modeling, *ESAIM: PROCEEDINGS*, **45**, (2014), 493-501.

- M. Mimault. Modélisation macroscopique de mouvements de foule. Une application à une foule composée de deux groupes., *Actes du colloque Edp-Normandie*, **Caen 2013**, (2014), 264-271.

Chapter 1

The one dimensional Hughes' model applied to a corridor evacuation

Contents

1.1 Introduction **10**
1.2 Analytical study **12**
1.2.1 Basic properties of solutions 12
1.2.2 The Riemann solver at the turning point 13
1.3 Numerical Study **17**
1.3.1 Wave front tracking 17
1.3.2 Finite volume schemes 20
1.4 Numerical convergence **22**
1.4.1 Data processing 22
1.4.2 Convergence of the wave front tracking 22
1.4.3 Convergence of finite volume schemes 24
1.4.4 More general initial data 25
1.5 Numerical application: a pedestrian tracking **27**
1.5.1 Algorithm 27
1.5.2 Results 28
1.6 Conclusion **28**

1.1 Introduction

In this chapter, we consider a generalization of the Hughes' macroscopic pedestrian flow model [56] in one space dimension. The pedestrian density $u = u(t, x)$ evolves according to a scalar conservation law, where the preferred direction of motion is given by an eikonal equation. The model reads as:

$$u_t - \left(uv(u) \frac{\phi_x}{|\phi_x|} \right)_x = 0, \tag{1.1a}$$

$$|\phi_x| = c(u), \tag{1.1b}$$

in the spatial domain $\Omega =]-1, 1[$. Above, $x \in \Omega$ is the space variable, $t \geq 0$ is the time, $u = u(t, x) \in [0, 1]$ is the normalized crowd density, $c = c(u)$ is the cost function, $v(u) = (1-u)$ is the mean velocity and we set $f(u) = uv(u) = u(1-u)$. We assume that $c : [0, 1[\to [1, +\infty[$ is a smooth function such that $c(0) = 1$ and $c'(u) \geq 0$ for $u \in [0, 1[$. Recall that the literature usually proposes the choice

$$c(u) = \frac{1}{v(u)} \tag{1.2}$$

as in [23, 35, 56, 57]. It comes from the third hypothesis Hughes made about the nature of pedestrian motion, knowing that pedestrians try to minimize their travel time according to a potential proportional to the inverse of the speed. (1.2) is equivalent to [56, Eq. 2.5b], in one dimension with the discomfort $g(u) = 1$.

Equations (1.1) must be completed with an initial density profile $u(0, \cdot) = u^0 \in \mathbf{BV}(\mathbb{R})$ and homogeneous weak Dirichlet boundary conditions at $x = \pm 1$, which represent the exit locations. We set

$$u(t, -1) = u(t, 1) = 0, \tag{1.3a}$$

$$\phi(t, -1) = \phi(t, 1) = 0. \tag{1.3b}$$

We remark here that condition (1.3a) has to be intended in the weak sense introduced in [9], which is detailed in Section 1.2.1. In particular, (1.3a) stands for simple absorbing boundary conditions at the ends of the walking domain, to model the fact that pedestrians exit the corridor. More complicate conditions could be imposed to model the reduced flux capacity induced by the presence of doors at the exits: the results presented in this part could be easily generalized in this sense following [27] and references therein.

One of the assumptions of the Hughes' model is that every pedestrian knows the exact distribution of density to evaluate her path. For the one dimensional case, [2] showed that the solution of the eikonal equation, gives two connex subdomains, one with the speed orientated towards the left and the other one to the right. It makes sure that no pedestrian goes against the chosen direction of its group, until her trajectory crosses the turning curve, see Ch. 5. [25] shows introduced local limitations to induce a more natural behavior.

We observe that (1.1a) can be rewritten as

$$u_t - (f(u) \operatorname{sgn}(\phi_x))_x = 0, \tag{1.4}$$

and the unique viscosity solution to the Dirichlet problem (1.1b), (1.3b) is given by the value function of the corresponding control problem with discontinuous coefficient $c(u)$, i.e.

$$\phi(t,x) = \begin{cases} \displaystyle\int_{-1}^{x} c\left(u(t,y)\right)\ dy & \text{if } -1 \le x \le \xi(t), \\ \displaystyle\int_{x}^{1} c\left(u(t,y)\right)\ dy & \text{if } \xi(t) \le x \le 1, \end{cases} \tag{1.5}$$

where $\xi(t) \in \Omega$ is implicitly defined by the identity

$$\int_{-1}^{\xi(t)} c\left(u(t,y)\right)\ dy = \int_{\xi(t)}^{1} c\left(u(t,y)\right)\ dy. \tag{1.6}$$

Therefore, equation (1.1a) can be written as a scalar conservation law with discontinuous space-time dependent flux:

$$u_t + F(t,x,u)_x = 0, \tag{1.7}$$

where $F(t,x,u) = \operatorname{sgn}\left(x - \xi(t)\right) f(u)$. Observe that the position of the discontinuity is not *a priori* fixed, as assumed in previous results on conservation laws with discontinuous fluxes (see for example [60] and references therein), but depends nonlocally on u itself. Therefore, known convergence results for finite volume schemes do not apply in this setting.

From the mathematical point of view, problem (1.1) presents a nontrivial coupling between a scalar conservation law and an eikonal equation, that poses several challenging questions concerning existence, uniqueness, numerical approximation and construction of the solutions. Some preliminary results concerning properties of solutions have been obtained in [2, 39]. In particular, they provide a notion of entropy weak solutions, a discussion on their qualitative behavior, and an algorithm to construct locally in time a self-similar solution in a neighborhood of the turning point $x = \xi(t)$ (see [2, Theorem 1]).

Here we are interested in computing numerically the weak solutions of the nonregularized hyperbolic problem (1.1). As remarked above, classical finite volume techniques for discontinuous fluxes do not apply here due to the fact that the discontinuity location is not a priori fixed, but depends nonlocally on the solution itself. Nevertheless, we show evidence that a direct application of classical schemes allows to recover the exact solutions. Since these are not known explicitly, the convergence of the finite volume schemes is numerically tested on accurate approximations of entropy weak solutions computed using the wave front tracking algorithm (for a detailed review of the method we refer to [54]). [3] provides existence results for the model (1.1) for the cases where the trace of the density distribution is zero along the turning curve. Even if a general analytical proof of convergence of wave front tracking approximate solutions is not available at the moment, this approximation method captures by construction the exact behavior of the solution at the turning point, without producing the oscillations observed with the use of finite volume schemes.

These schemes will be coupled with a tracking algorithm to show the path of a single pedestrian during an evacuation, giving a better insight of the *turning phenomenon* which happens during an evacuation.

1.2 Analytical study

1.2.1 Basic properties of solutions

For sake of simplicity, we refer to the initial-boundary value problem

$$\begin{array}{ll} u_t + F(t,x,u)_x = 0, & \\ |\phi_x| = c(u), & x \in \Omega\ , t \geq 0, \\ u(0,x) = u^0(x), & x \in \Omega \\ u(t,-1) = u(t,1) = 0, & \\ \phi(t,-1) = \phi(t,1) = 0, & t \geq 0, \end{array} \tag{1.8}$$

Following [39], we look for the following class of solutions.

Definition 1.2.1 (Entropy Weak Solutions).
A function $u \in \mathbb{C}^0\left(\mathbb{R}^+; \mathbf{L_1}(\Omega)\right) \cap \mathbf{BV}\ \left(\mathbb{R}^+ \times \Omega; [0,1]\right)$ is an entropy weak solution of the initial-boundary value problem (1.8) *if the following Kružkov-type entropy inequality holds for all $k \in [0,1]$ and all test functions $\psi \in (\mathbb{R} \times \Omega; \mathbb{R}^+)$:*

$$\begin{aligned} 0 \leq & \int_0^{+\infty}\int_{-1}^{1} \left(|u-k|\psi_t + \Phi(t,x,u,k)\psi_x\right)\ dx\ dt + \int_{-1}^{1} \left|u^0(x) - k\right|\psi(0,x)\ dx \\ & + \operatorname{sgn}(k) \int_0^{+\infty} \left(f\left(u(t,1-)\right) - f(k)\right)\psi(t,1)\ dt \\ & + \operatorname{sgn}(k) \int_0^{+\infty} \left(f\left(u(t,-1+)\right) - f(k)\right)\psi(t,-1)\ dt \\ & + 2\int_0^{+\infty} f(k)\psi\left(t,\xi(t)\right)\ dt. \end{aligned} \tag{1.9}$$

Above, $\Phi(t,x,u,k) = \operatorname{sgn}(u-k)\left(F(t,x,u) - F(t,x,k)\right)$ and the boundary conditions are intended in weak form as in [9]. In particular, the traces of the solution at the boundary points must satisfy

$$\begin{array}{rl} f\left(u(t,-1+)\right) \geq f(k), & \text{for all } k \in [0, u(t,-1+)], \\ f\left(u(t,1-)\right) \geq f(k), & \text{for all } k \in [0, u(t,1-)]. \end{array}$$

This in particular implies $u(t,-1+) \leq 1/2$ and $u(t,1-) \leq 1/2$.
Besides, by taking suitable test functions ψ vanishing along $x = \xi(t)$, it is easy to recover the Rankine-Hugoniot condition

$$f\left(u^+\right) + f\left(u^-\right) = \dot{\xi}(t)\left(u^+ - u^-\right), \tag{1.10}$$

where we have denoted by $u^+ = u^+(t) = u\left(t,\xi(t)+\right)$ and $u^- = u^-(t) = u\left(t,\xi(t)-\right)$ the right and left traces of u at $x = \xi(t)$. We remark here that if $u(t,\cdot)$ is continuous at $x = \xi(t)$, then (1.10) gives $f\left(u\left(t,\xi(t)\right)\right) = 0$ and therefore $u\left(t,\xi(t)\right) \in \{0,1\}$.
We refer to [39] for more specific properties of the entropy solution.

1.2.2 The Riemann solver at the turning point

The argument proposed in [2] is based on the observation that, due to finite wave propagation speed, for every fixed $\bar{t} \geq 0$ the solution $u(t,x)$ is well defined away from the turning point $\bar{\xi} = \xi(\bar{t})$ for $t > \bar{t}$ sufficiently small, say on $[-1, \bar{\xi} - \delta[\cup]\bar{\xi} + \delta, 1]$ for some $\delta > 0$. Therefore, the following quantity is well defined

$$\left\{ \int_{\bar{\xi}+\delta}^{1} - \int_{-1}^{\bar{\xi}-\delta} \right\} \partial_t[c(u(t,y))]dy =: \Psi^*.$$

Moreover, let us assume that the the function $u(\bar{t}, x)$ is constant in a left and right neighbors of $\bar{\xi}$, let's say

$$u(\bar{t}, x) = \begin{cases} u_L & \text{if } \bar{\xi} - 2\delta < x < \bar{\xi}, \\ u_R & \text{if } \bar{\xi} < x < \bar{\xi} + 2\delta. \end{cases} \tag{1.11}$$

Assuming Ψ^* to be constant for small times $t > \bar{t}$, the solution around the turning point will be self-similar, behaving as a solution of a Riemann problem. This assumption is met when there are no interacting patterns in the whole interval $[-1, 1]$. Therefore, deriving (1.6) w. r. to t, we have for small times $t > \bar{t}$

$$\dot{\xi}(t)\left(c(u_L) + c(u_R)\right) = \Psi[u] := \Psi^* + \left\{ \int_{\xi(t)}^{\bar{\xi}+\delta} - \int_{\bar{\xi}-\delta}^{\xi(t)} \right\} \partial_t[c(u(t,y))]dy. \tag{1.12}$$

The term Ψ^* depends on $u(\bar{t}, \cdot)$ in a nonlocal way and may range all over $\mathbb{R}$, independently of u_L and u_R. The solution around $\bar{\xi}$ will be classified according to the value of Ψ^*.
Assuming that (1.11) holds, a self-similar solution around $(\bar{t}, \bar{\xi})$ is constructed locally in time using identity (1.12) as follows:

a. If $u_L > u_R$, the following cases occur.

   1a) If

$$\Psi* < \frac{f(u_R) + f(u_L)}{u_R - u_L}[c(u_R) + c(u_L)], \tag{1.13}$$

   then there exists a unique intermediate value u_M, with $u_L > u_M > u_R$, such that the solution is given by the turning curve ξ followed by a rarefaction between u_M and u_R. The state u_M is computed solving the equation

$$\frac{f(u) + f(u_L)}{u - u_L}[c(u_L) + c(u)] + q(u_R) - q(u) = \Psi^*$$

   for $u \in]u_R, u_L[$, where the function q is taken such that $q' = c'f'$. The speed of the turning curve is then given by

$$\dot{\xi} = \frac{f(u_M) + f(u_L)}{u_M - u_L}.$$

1b) If

$$\begin{aligned} \frac{f(u_R)+f(u_L)}{u_R-u_L}[c(u_R)+c(u_L)] &\leq \Psi* \\ \leq -v(u_L)(1+c(u_L)) - v(u_R)(1-c(u_R)), \end{aligned} \tag{1.14}$$

then a unique intermediate value $u_M \in [0, u_R]$ exists, such that the solution is given by the turning curve ξ followed by a shock of speed $1 - u_M - u_R$ between u_M and u_R. More precisely, u_M is the solution of the equation

$$\frac{f(u)+f(u_L)}{u-u_L}[c(u)+c(u_L)] - (1-u-u_R)[c(u)-c(u_R)] = \Psi^*$$

for $u \in [0, u_R]$. Notice that, if the equality holds in the r.h.s. of (1.14), then $u_M = 0$ and a vacuum appears between the turning point and the shock. The speed of the turning curve is computed using Rankine-Hugoniot condition as

$$\dot{\xi} = \frac{f(u_M)+f(u_L)}{u_M-u_L}.$$

1c) If

$$\begin{aligned} -v(u_L)(1+c(u_L)) - v(u_R)(1-c(u_R)) &< \Psi* \\ < v(u_R)(1+c(u_R)) + v(u_L)(1-c(u_L)), \end{aligned} \tag{1.15}$$

then the solution is given by a shock of speed $u_L - 1$ followed by ξ and by a shock of speed $1 - u_R$, the intermediate state around ξ being $u_M = 0$. The speed of the turning curve is computed by

$$2\dot{\xi} = \Psi^* + (1-u_L)[c(u_L)-1] + (1-u_R)[1-c(u_R)].$$

1d) Finally, if

$$\Psi* \geq v(u_R)(1+c(u_R)) + v(u_L)(1-c(u_L)), \tag{1.16}$$

then the solution is given by a shock of speed $u_L + u_M - 1$ between u_L and $u_M \in [0, u_R]$ followed by ξ. The value of u_M is the zero of the equation

$$\frac{f(u_R)+f(u)}{u_R-u}[c(u)+c(u_R)] + (1-u-u_L)[c(u)-c(u_L)] = \Psi^*.$$

If the equality holds in (1.16), then $u_M = 0$, otherwise $u_M > 0$. The speed of the turning curve is given by

$$\dot{\xi} = \frac{f(u_R)+f(u_M)}{u_R-u_M}.$$

b. If $u_L < u_R$, the following cases occur.

2a) If

$$\Psi* \leq -v(u_L)(1+c(u_L)) - v(u_R)(1-c(u_R)), \tag{1.17}$$

then a unique intermediate value $u_M \in [0, u_L]$ exists, such that the solution is given by ξ followed by a shock of speed $1 - u_M - u_R$ between u_M and u_R. The stateu_M is given by the solution of the equation

$$\frac{f(u)+f(u_L)}{u-u_L}[c(u)+c(u_L)] - (1-u-u_R)[c(u)-c(u_R)] = \Psi^*.$$

If the equality holds in (1.17), then $u_M = 0$ and a vacuum appears between the turning point and the shock. The speed of the turning curve is computed using Rankine-Hugoniot condition as

$$\dot{\xi} = \frac{f(u_M)+f(u_L)}{u_M - u_L}.$$

2b) If

$$\begin{aligned} -v(u_L)(1+c(u_L)) - v(u_R)(1-c(u_R)) &< \Psi* \\ &< v(u_R)(1+c(u_R)) + v(u_L)(1-c(u_L)), \end{aligned} \tag{1.18}$$

then the solution is given by a shock of speed $u_L - 1$ followed by ξ and by a shock of speed $1 - u_R$, the intermediate state being $u_M = 0$. The speed of the turning curve is given by the equality

$$2\dot{\xi} = \Psi^* + (1-u_L)[c(u_L)-1] + (1-u_R)[1-c(u_R)].$$

2c) If

$$\begin{aligned} v(u_R)(1+c(u_R)) + v(u_L)(1-c(u_L)) &\leq \Psi* \\ &\leq \frac{f(u_R)+f(u_L)}{u_R-u_L}[c(u_R)+c(u_L)], \end{aligned} \tag{1.19}$$

then the solution is given by a shock of speed $u_L + u_M - 1$ between u_L and $u_M \in [0, u_L]$, followed by the turning curve ξ. In particular, u_M is the solution of the equation

$$\frac{f(u_R)+f(u)}{u_R-u}[c(u)+c(u_R)] + (1-u-u_L)[c(u)-c(u_L)] = \Psi^*.$$

If equality holds in the l.h.s. of (1.19), then $u_M = 0$, otherwise $u_M > 0$. The speed of the turning curve is given by

$$\dot{\xi} = \frac{f(u_R)+f(u_M)}{u_R-u_M}.$$

2d) Finally, if

$$\Psi* > \frac{f(u_R)+f(u_L)}{u_R-u_L}[c(u_R)+c(u_L)], \tag{1.20}$$

then there exists a unique intermediate value u_M, with $u_R > u_M > u_L$, such that the solution is given by a rarefaction between u_L and u_M followed by the turning curve ξ. The state u_M is the solution of the equation

$$\frac{f(u_R)+f(u)}{u_R-u}[c(u)+c(u_R)]+q(u)-q(u_L)=\Psi^*$$

for $u \in]u_L, u_R[$, where the function q is taken such that $q' = c'f'$. The speed of the turning curve is then given by

$$\dot{\xi} = \frac{f(u_R)+f(u_M)}{u_R-u_M}\,.$$

c. If $u_L = u_R = u^*$, the following cases occur.

3a) If

$$\Psi* \leq -2v(u^*), \tag{1.21}$$

then a unique intermediate value $u_M \in [0, u^*]$ exists, such that the solution is given by the turning curve ξ followed by a shock of speed $1-u_M-u^*$ between u_M and u^*. The value of u_M is the zero of the equation

$$\frac{f(u)+f(u^*)}{u-u^*}[c(u)+c(u^*)]-(1-u-u^*)[c(u)-c(u^*)]=\Psi^*,$$

and the speed of the turning curve is

$$\dot{\xi} = \frac{f(u_M)+f(u^*)}{u_M-u^*}\,.$$

If the equality holds in (1.21), then $u_M = 0$ and a vacuum appears between the turning point and the shock.

3b) If

$$-2v(u^*) < \Psi* < 2v(u^*), \tag{1.22}$$

then the solution is given by a shock of speed u^*-1 followed by ξ and by a shock of speed $1-u^*$, the intermediate state across ξ being $u_M = 0$. In this case,

$$\dot{\xi} = \Psi^*/2\,.$$

3c) Finally, if

$$\Psi* \geq 2v(u^*), \tag{1.23}$$

then the solution is given by a shock of speed $u^* + u_M - 1$ between u^* and $u_M \in [0, u^*]$ followed by ξ.

$$\frac{f(u^*) + f(u)}{u^* - u}[c(u) + c(u^*)] + (1 - u - u^*)[c(u) - c(u^*)] = \Psi^*.$$

If equality holds in the l.h.s. of (1.23), then $u_M = 0$, otherwise $u_M > 0$. The speed of the turning curve is given by

$$\dot{\xi} = \frac{f(u^*) + f(u_M)}{u^* - u_M}.$$

Further details on the above construction, such as the proof of existence and uniqueness of the intermediate state u_M, can be found in [2, Theorem 1].

1.3 Numerical Study

1.3.1 Wave front tracking

The wave front tracking technique for classical scalar conservation laws consists in constructing piecewise constant exact solutions of an approximated problem with piecewise constant initial datum and piecewise linear flux f^ν, coinciding with $f = uv(u)$ on the mesh $\mathcal{M}_\nu = \{u_i^\nu\}_{i=0}^{2^\nu} \subset [0, 1]$ defined by

$$\mathcal{M}_\nu = \left(2^{-\nu}\mathbb{N} \cap [0, 1]\right)$$

for $\nu \in \mathbb{N}$, $\nu > 0$. We refer the reader to [20, 54] for a general overview of the technique. We describe here the extension of the method to the case of the coupled problem (1.1).

Initialization. The algorithm is started taking a piecewise constant approximation of the initial datum u^0 in the form

$$u^{\nu,0} = \sum_{j\in\mathbb{Z}} u_{0,j}^\nu \, \chi_{]x_{j-1},x_j]}, \quad \text{with } u_{0,j}^\nu \in \mathcal{M}_\nu,$$

where the density values $u_{0,j}^\nu$ and the jump points x_j are chosen so that $u^{\nu,0}$ approximates u^0 in the sense of the strong $\mathbf{L_1}$ topology, that is

$$\lim_{\nu\to\infty} \|u^{\nu,0} - u^0\|_{\mathbf{L_1}(\Omega)} = 0,$$

and $\mathbf{TV}(u^{\nu,0}) \leq \mathbf{TV}(u^0)$. Unlike classical finite volume schemes, the points x_j do not coincide with a uniform grid, and approximation refinement will be performed not on the space mesh size, but on the density mesh $\mathcal{M}_\nu$.
Moreover, we set $x_0 = \xi_0$ (even if it needs not to be a jump point for $u^{\nu,0}$). The initial position of the turning point, $\xi_0 = \xi(0)$, is calculated from the cost balance equation (1.6) at $t = 0$:

$$\int_{-1}^{\xi_0} c\left(uu^{\nu,0}(y)\right) \, dy = \int_{\xi_0}^{1} c\left(uu^{\nu,0}(y)\right) \, dy,$$

which reduces to

$$\sum_{j\leq 0} c(u_{0,j}^\nu)(x_j - x_{j-1}) = \sum_{j>0} c(u_{0,j}^\nu)(x_j - x_{j-1}).$$

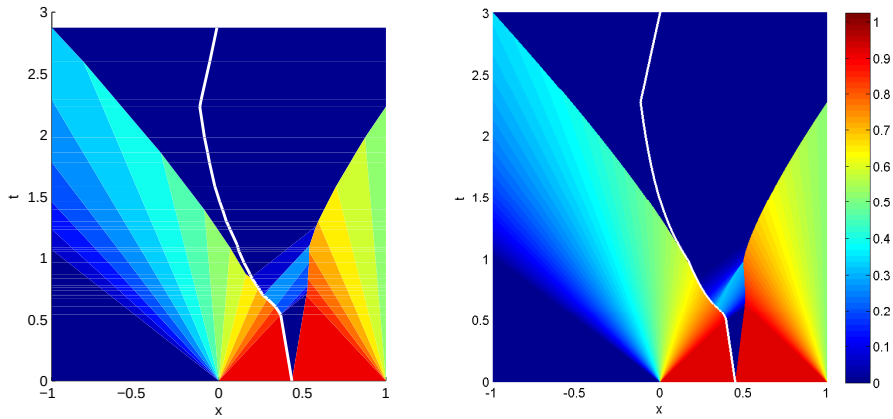

Figure 1.1: Wave front tracking solution of (1.8) with $u^0(x) = 0$ for $x \in]-1, 0[$ and $u^0(x) = 0.9$ for $x \in]0, 1[$, and mesh sizes $\Delta u = 2^{-4}$ (left) and $\Delta u = 2^{-10}$ (right). The white curve is the trajectory $x = \xi(t)$.

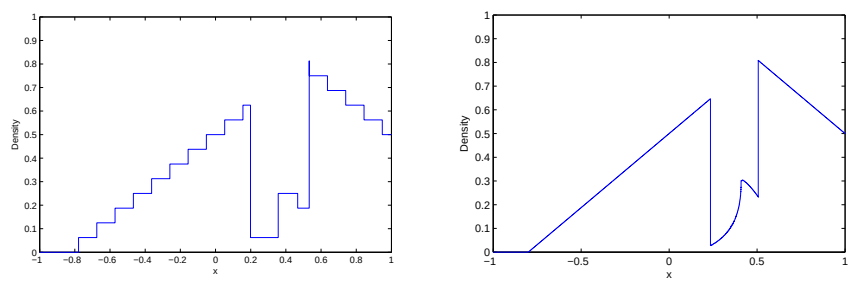

Figure 1.2: Density profile at time $t = 0.8$ with initial density $u^0(x) = 0$ for $x \in]-1, 0[$ and $u^0(x) = 0.9$ for $x \in]0, 1[$, computed using wave front tracking scheme with mesh sizes $\Delta u = 2^{-4}$ (left) and $\Delta u = 2^{-10}$ (right). The position of the turning point $x = \xi(t)$ coincides with the first downward jump discontinuity from the left.

Observe that we may have $u^\nu_{0,0} = u^\nu_{0,1}$.
For small times $t > 0$, a piecewise approximate solution (u^ν, ξ_ν) to (1.8) is constructed piecing together the solutions to the local Riemann problems

$$\begin{cases} \partial_t u + \partial_x \left(\operatorname{sgn}(x - \xi_0) f^\nu(u)\right) = 0, \\ u(0, x) = \begin{cases} u^\nu_{0,0} & \text{if } x < \xi_0, \\ u^\nu_{0,1} & \text{if } x > \xi_0, \end{cases} \\ \dot{\xi}(u^+ - u^-) = \Psi[u], \end{cases} \qquad \begin{cases} \partial_t u + \partial_x \left(\operatorname{sgn}(x_j - \xi_0) f^\nu(u)\right) = 0, \\ u(0, x) = \begin{cases} u^\nu_{0,j} & \text{if } x < x_j, \\ u^\nu_{0,j+1} & \text{if } x > x_j, \end{cases} \\ j \neq 0. \end{cases} \tag{1.24}$$

Solving the Riemann problems above (where the original flux function f has been substituted by the piecewise linear approximation f^ν) replaces smooth rarefaction fronts by rarefaction fans of constant values $u^\nu_{1,j}$, $j = l_1, \ldots, l_{N_\nu}$, such that $\left|u^\nu_{1,j} - u^\nu_{1,j-1}\right| = 2^{-\nu}$, separated by jump discontinuities moving with speeds $s_{1,j} = -\operatorname{sgn}(\phi_x)(1 - u^\nu_{1,j} - u^\nu_{1,j-1})$, see Figures 1.1 and 1.2. Note that the solution to the Riemann problem in (1.24), left, is constructed by

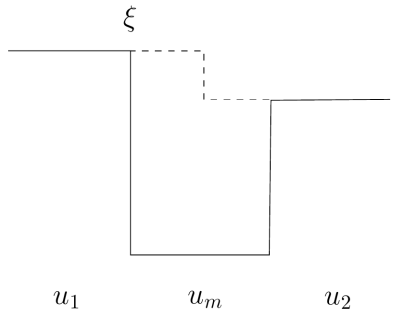

Figure 1.3: When a choc appears at the turning point, the total variation increases. Here $TV(u_{n+1}) = TV(u_n) + 2(u_2 - u_1)$

means of the Riemann solver described previously in Section 1.2.2, where the value of the intermediate state u_M is approximated by the closest point of the mesh $\mathcal{M}_\nu$. This introduces an error in the resolution of the linearized problem, but guarantees that all density values of the approximate solution keeps belonging to $\mathcal{M}_\nu$.
The new density values $u^\nu_{1,j_1}, \dots, u^\nu_{1,j_{N_\nu}}$ resulting from the solution of each Riemann problem are interposed to the corresponding density values $u^\nu_{0,j}, u^\nu_{0,j+1}$, and all are relabeled $u^\nu_{1,j}$, $j \in \mathbb{Z}$. To each couple of subsequent density values, we associate the speed of the corresponding wave $s_{1,j}$ or $\dot{\xi}_\nu$, and the corresponding departure point x_j. This allows to compute the corresponding wave trajectories $x_j(t) = x_j + s_{1,j}t$ and respectively $x_0(t) = \xi_\nu(t) = \xi_0 + \dot{\xi}_\nu t$ for the turning curve, and to update the solution

$$u^\nu(t,\cdot) = \sum_{j\in\mathbb{Z}} u^\nu_{1,j}\ \chi_{]x_{j-1}(t),x_j(t)]},$$

for small $t > 0$.

Iterations. The piecewise constant approximate solution u^ν constructed in the previous step can be prolonged up to the first time $\bar{t} > 0$, when two waves collide, or a wave hits the turning curve ξ^ν. In both cases, the intermediate density value is deleted, a new Riemann problem arises and its solution, obtained in the former case with the classical Riemann solver and in the latter by means of the solver described in Section 1.2.2, allows to extend (u^ν, ξ_ν) further in time, up to the next wave interaction. We point out that the absorbing boundary conditions (1.3a) are taken into account by simply dropping the waves hitting the left and right boundaries.

The proof of convergence of the wave front tracking solution to the exact solution of (1.8) needs a bound of the numerical solution total variation, in order to apply Helly's compactness theorem for **BV** functions. In matter of fact, the total variation increases when shocks appear at the turning point.
We rely on numerical proofs to support this convergence, which can be found in the tests reported in Section 1.4.2.
The MATLAB code used for the numerical tests presented in Section 1.4 can be downloaded at the following URL:
`http://www-sop.inria.fr/members/Paola.Goatin/wft.html`.

1.3.2 Finite volume schemes

In this section, we describe the algorithm used in [39] for numerical simulations of the model (1.1). Finite volume schemes are commonly used to compute numerically solutions of the 2D version of the model, see for example [55, 59] and references therein for more details and results.
Here we aim at investigating the behavior of classical schemes near the turning curve, and whether they manage to capture correctly the behavior of the solution constructed via the wave front tracking algorithm.
Given an initial datum $u(0,x) = u^0(x)$ and homogeneous Dirichlet boundary conditions (1.3), we solve (1.1) in an iterative manner at each time step, i.e.

a. Given u, solve the eikonal equation (1.1b) by the fast sweeping method, see Section 1.3.2.

b. Given ϕ, solve the nonlinear conservation law (1.1a) using Godunov or Rusanov scheme.

The domain $[-1,1]$ is divided into N uniform cells $I_j = [x_{j-1/2}, x_{j+1/2}]$ with centers at points $x_j = j\Delta x$, with $\Delta x = 2/N$. The explicit algorithm used to generate the approximations u_j^n was introduced by Towers in [83] and is written in conservation form

$$u_j^{n+1} = u_j^n - \frac{\Delta t^n}{\Delta x}\left(k^n_{j+\frac{1}{2}}\mathrm{h}^n_{j+\frac{1}{2}} - k^n_{j-\frac{1}{2}}\mathrm{h}^n_{j-\frac{1}{2}}\right), \tag{1.25}$$

where $\Delta t^n = t^{n+1} - t^n$ is chosen to satisfy the following CLF condition

$$\Delta t^n < 0.5\ \frac{\Delta x}{\max\left\{\max_j\left|f'(u_j^n)\right|, |\dot{\xi}^n|\right\}}\ . \tag{1.26}$$

Aiming to have just a qualitative representation of the solution, in our computations we force $\xi^n = \xi(t^n)$ to be located at the middle of the cell it belongs to at each time step, i.e. $\xi(t^n) = x_j$, for j such that $\mathrm{sgn}(\phi_x(x_{j-1/2})) > \mathrm{sgn}(\phi_x(x_{j+1/2}))$. In the above formula (1.26), the coefficient 0.5 is chosen to avoid interactions of ξ^n with the cell boundaries, and $|\dot{\xi}^n|$ is estimated at each time step by deriving the implicit expression (1.6), which gives

$$\dot{\xi}(t)\left(c(u^-) + c(u^+)\right) = \left\{\int_{\xi(t)}^{1} - \int_{-1}^{\xi(t)}\right\}\partial_t\left[c(u(t,y))\right]\mathrm{d}y$$

From the above identity we recover the sharp upper bound

$$|\dot{\xi}^n| \le \frac{1}{2}\left|\sum_j (1 - u_j^n - u_{j+1}^n)\left(c(u_j^n) - c(u_{j+1}^n)\right)\right|\ .$$

In (1.25), we set $k^n_{j\pm1/2} = \mathrm{sgn}\left(\phi^n_x(x_{j\pm1/2})\right)$, where

$$\phi^n_x(x_{j+1/2}) \simeq \frac{\phi^n(x_{j+1}) - \phi^n(x_j)}{\Delta x}\ .$$

The numerical flux $\mathrm{h}^n_{j+1/2} = h(u_j^n, u_{j+1}^n)$ is chosen to be monotone and consistent, i.e. $h(u,u) = f(u) = uv(u)$. In order to maintain the monotonicity of the scheme, we transpose the arguments when $k_{j+1/2}$ sign changes, i.e.

$$\mathrm{h}_{j+\frac{1}{2}} = \begin{cases} h\left(u_j, u_{j+1}\right) & \text{if } k_{j+\frac{1}{2}} \ge 0, \\ h\left(u_{j+1}, u_j\right) & \text{if } k_{j+\frac{1}{2}} < 0. \end{cases} \tag{1.27}$$

The Fast Sweeping algorithm

The method described in [86] uses a Godunov upwind difference scheme to discretize the partial differential equation at interior points of the domain:

$$[(\phi_j^{\Delta x} - \phi_{xmin}^{\Delta x})^+]^2 = c(u_i)^2 \Delta x^2, \qquad j = 2, ..., N-1, \tag{1.28}$$

where $\phi_j^{\Delta x} \simeq \phi(x_j)$ and $\phi_{xmin}^{\Delta x} = \min(\phi_{j-1}^{\Delta x}, \phi_{j+1}^{\Delta x})$ and

$$(x)^+ = \begin{cases} x, & x > 0, \\ 0, & x \leq 0. \end{cases}$$

Initialization. We assign exact values at boundary grid points $x = \pm 1$ to enforce boundary condition $\phi(\pm 1) = 0$. We assign sufficiently large positive values at all other grid points. These points will be updated later.

Iterations. At each grid point x_j whose value is not fixed during the initialization, compute the solution of (1.28), denoted by $\bar{\phi}_j$, from the current values of its neighbors $\phi_{j\pm 1}^{\Delta x}$ and then update $\phi_j^{\Delta x}$ to be the smaller one between $\bar{\phi}_j$ and $\phi_j^{\Delta x}$, i.e. $\phi_j^{\text{new}} = \min(\phi_j^{\text{old}}, \bar{\phi}_j)$. We sweep the whole domain with two alternating orderings repeatedly:

$$(1)\ j = 1 : N, \quad (2)\ j = N : 1,$$

and we stop when the fixed error threshold is met. One can refer to Sec. C to a review of a fast sweeping algorithm for an eikonal equation on a two dimensional space.

Godunov scheme

The Godunov scheme [46] for a conservation law of type $u_t + \mathbf{F}(u)_x = 0$ is classically obtained by using the exact solution with piecewise constant initial data. The numerical flux is $h(u_1, u_2) = \mathbf{F}\left(\mathcal{R}(0; u_1, u_2)\right)$, where $\mathcal{R}(0; u_1, u_2)$ is the solution of the Riemann problem with left and right states u_1 and u_2 evaluated at $x = 0$, where a jump on the initial data occurs. The Godunov flux is given by

$$h(u_1, u_2) = \begin{cases} \min_{[u_1,u_2]} \mathbf{F}(w) & \text{if } u_1 \leq u_2, \\ \max_{[u_1,u_2]} \mathbf{F}(w) & \text{if } u_1 \geq u_2. \end{cases} \tag{1.29}$$

We remark that in the case of problem (1.1) an explicit Riemann solver at the ξ interface would require to code all the possible cases detailed in Section 1.2.2, and would be very expensive. Fortunately, we get rid of this inconvenience by assuming ξ inside the cell, at the center.

Rusanov scheme

In [83], the author proves convergence of Engquist-Oscher scheme for conservation laws with discontinuous flux. These results can be used in the second step to solve the conservation law. For our simulations we have used a variant introduced by Rusanov [77], whose flux is given by

$$h(u_1, u_2) = \frac{1}{2}\left(f(u) + f(v)\right) + \frac{1}{2}\max\left\{\left|f'(u)\right|, \left|f'(v)\right|\right\}(u - v), \tag{1.30}$$

and is known to be robust but diffusive. The main appeal of this scheme lies in the explicit form of the equation flux in the numerical flux, which will be used in the following of this thesis.

1.4 Numerical convergence

In this section we provide some numerical tests showing the convergence of the wave front tracking algorithm and finite volume schemes described in the previous Sections 1.3.1, 1.3.2. To this end, we choose an initial datum u^0 that gives a nontrivial behavior at the turning curve. In fact, if the solution u of (1.8) is continuous at $x = \xi(t)$, that is, $u(t, \xi(t)-) = 0 = u(t, \xi(t)+)$, we deal with classical solutions on each side of the turning curve, and the convergence is standard.
In the following, we consider the Riemann-type initial datum

$$u^0(x) = \begin{cases} 0 & \text{if } -1 < x < 0, \\ 0.9 & \text{if } 0 < x < 1, \end{cases} \tag{1.31}$$

and the cost function $c(u) = 1/v(u) = 1/(1-u)$. We run simulations up to time $T = 3$, when all pedestrians have left the domain Ω and $u(T, x) \equiv 0$, see Fig. 1.1.

1.4.1 Data processing

Wave front tracking solutions are not defined on a standard cartesian grid in space and time, but rather as constant values on polygonal regions delimited by wave fronts (see Fig. 1.4.1). In order to compare the approximate solutions obtained via wave front tracking at different mesh sizes, and finite volume approximations with the wave front tracking reference solution, we have to convert these data sets into values defined on a reference cartesian grid.
In what follows we denote by X_{WFT} the data obtained from the wave front tracking procedure, by $\widetilde{X}_{WFT}$ the processed data and by X_{FV} those obtained from finite volume schemes. Values for $\tilde{u}^{\nu}_{WFT}$ are obtained by taking the corresponding values of u^{ν}_{WFT} at the cartesian grid nodes, see Fig. 1.4.1. Finally, we operate a $\mathbf{L_1}$-norm comparison, according to the following formula:

$$\epsilon(\nu, \Delta x) = \int_0^T \int_{-1}^1 |\tilde{u}^{\nu}_{WFT} - u^{\Delta x}_{FV}| dx dt = \sum_{n=1}^{N} \sum_{j=1}^{J} \left| (\tilde{u}^{\nu}_{WFT})^n_j - (u^{\Delta x}_{FV})^n_j \right| \Delta x \Delta t^n,$$

where ν refers to the wave-front tracking mesh size and Δx denotes the space-mesh size of the cartesian grid used for the finite volume scheme.
We remark that the above procedure inevitably introduces an approximation error in the computation of the $\mathbf{L_1}$-error, since

$$\int_0^T \int_{-1}^1 |\tilde{u}^{\nu}_{WFT} - u^{\Delta x}_{FV}| dx dt \neq \int_0^T \int_{-1}^1 |u^{\nu}_{WFT} - u^{\Delta x}_{FV}| dx dt.$$

1.4.2 Convergence of the wave front tracking

Here, we just show that the $\mathbf{L_1}$-error between two subsequent discretization meshes $2^{-\nu}$ and $2^{-\nu-1}$

$$\epsilon_\nu = \left| \tilde{u}^{\nu+1}_{WFT} - \tilde{u}^{\nu}_{WFT} \right|_{\mathbf{L_1}}$$

decreases to zero as ν increases, thus supporting the expected convergence result.
Table 1.1 and Fig. 1.5 show that the sequence $\{\tilde{u}^{\nu}_{WFT}\}$ is a Cauchy sequence in $\mathbf{L_1}$. The decreasing is not monotonic because of new front appearing with the refinement of u.

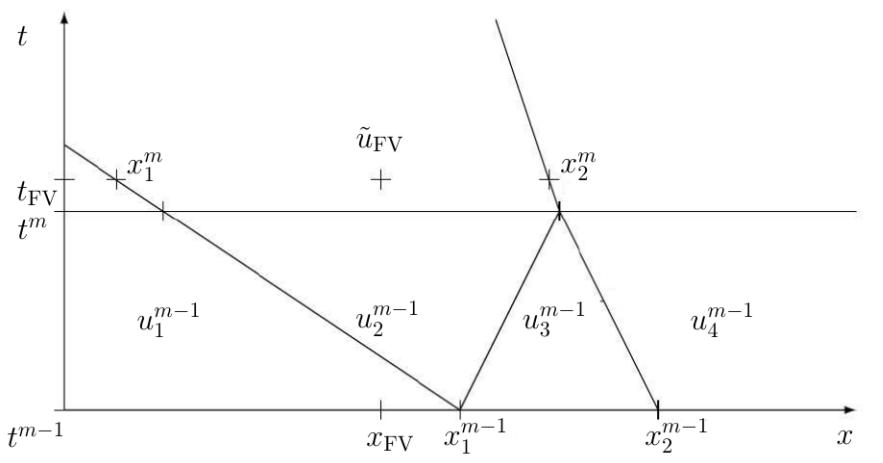

Figure 1.4: Definition of $\tilde{u}_{WFT}$ at the point (t_{FV}, x_{FV}) of the reference cartesian grid: after finding the last interaction time $t^m \leq t_{VF}$ in u_{WFT}, one has to compare the positions of the corresponding interfaces $x_i(t_{FV}) = x_i^m + s_i(t_{FV} - t^m)$ with respect to x_{FV}, where $s_i = 1 - u_i - u_{i+1}$ are the speeds of the wave fronts. Here $\tilde{u}_{WFT} = u_2^m = u_2^{m-1}$.

ν	Δu	ϵ_ν
5	2^{-5}	$4.280e-2$
6	2^{-6}	$2.164e-2$
7	2^{-7}	$6.141e-3$
8	2^{-8}	$5.048e-3$
9	2^{-9}	$1.755e-3$
10	2^{-10}	$2.091e-3$
11	2^{-11}	$4.305e-4$
12	2^{-12}	$4.347e-4$

Table 1.1: $\mathbf{L_1}$-error ϵ_ν for wave front tracking method between two subsequent discretization meshes $2^{-\nu}$ and $2^{-\nu-1}$. The comparison is done on a cartesian grid with $\Delta x = 10^{-3}$ and $\Delta t = 0.5\Delta x$.

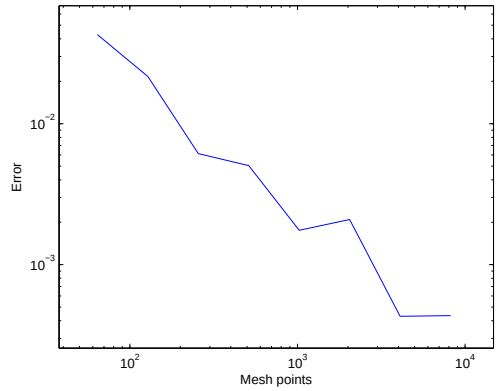

Figure 1.5: $\mathbf{L_1}$-error ϵ_ν between two subsequent discretization meshes $2^{-\nu}$ and $2^{-\nu-1}$, for $\nu = 5, \ldots, 12$, corresponding to the initial datum given by (1.31).

Δx	ϵ_G	γ_G	ϵ_R	γ_R
1/50	$7.24e-2$	0.66	$7.44e-2$	0.67
1/100	$4.56e-2$	0.66	$4.68e-2$	0.67
1/250	$2.49e-2$	0.66	$2.55e-2$	0.67
1/500	$1.52e-2$	0.67	$1.55e-2$	0.67
1/1000	$9.03e-3$	0.68	$9.12e-2$	0.68
1/1500	$6.66e-3$	0.69	$6.62e-3$	0.68

Table 1.2: $\mathbf{L_1}$-norm of the error for Godunov and Rusanov schemes for (1.31) depending on the space step Δx, and corresponding convergence order. Above ϵ_X stands for the error of the finite volume scheme and $\gamma_X = \frac{|\ln X|}{|\ln \Delta x|}$ the order of convergence of the flux, with G for the Godunov scheme and R for the Rusanov flux.

1.4.3 Convergence of finite volume schemes

Assuming the convergence of the wave front tracking scheme, which treats explicitly the dynamics at the turning point, we take as reference "exact" solution the one obtained with density mesh size $\Delta u = 2^{-10}$, and we compare it to the approximations computed by Godunov and Rusanov schemes for different space mesh sizes, computing the $\mathbf{L_1}$-norm of the difference. The following Table 1.2 Fig. 1.6 report the values of the $\mathbf{L_1}$-error computed on the time interval $[0, T]$ with $T = 1.2$, in order to focus on the nonclassical behavior of the solution. Indeed, at $T = 1.2$ vacuum has appeared around the turning point ξ, and the solution has become classical. For a set of space meshes ranging from $\Delta x = 1/50$ to $\Delta x = 1/1500$, we observe a linear decrease on logarithmic scale. This gives a numerical convergence order of about 0.67 for both Godunov and Rusanov schemes, without an explicit treatment of the solution's behavior at $x = \xi(t)$. Fig. 1.7 shows the profiles of the three numerical approximations in a neighborhood of the turning point. We observe that Godunov scheme displays small oscillations close to $x = \xi(t)$.

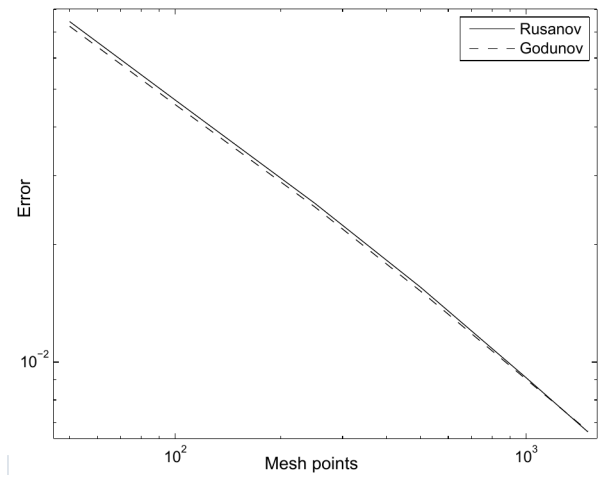

Figure 1.6: $\mathbf{L_1}$-norm of the error in logarithmic scale for mesh sizes $\Delta x = 1/50, \ldots, 1/1500$, for Godunov and Rusanov schemes corresponding to the initial datum given by (1.31).

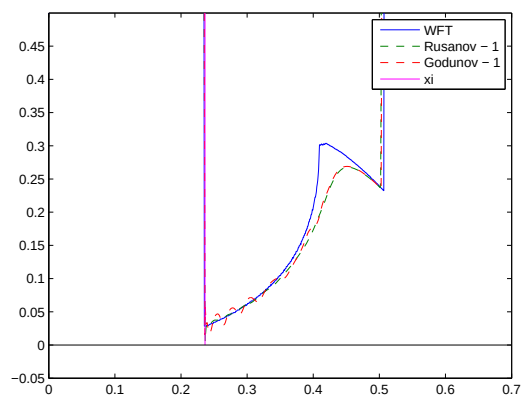

Figure 1.7: Zoom of the numerical approximations in a neighborhood of the turning point $x = \xi(t)$ for the initial datum (1.31) at time $t = 0.8$. The wave front tracking profile is given by the mesh $\Delta u = 2^{-10}$, and the finite volume space step is $\Delta x = 1/1500$.

1.4.4 More general initial data

We provide here the results of simulations performed considering a more general initial datum. We have taken

$$u^0 = \begin{cases} 0.8 & \text{if } -0.8 \leq x \leq -0.5, \\ 0.6 & \text{if } -0.3 \leq x \leq 0.3, \\ 0.9 & \text{if } 0.4 \leq x \leq 0.75, \\ 0 & \text{elsewhere}, \end{cases} \tag{1.32}$$

as in [35, Figure 6] in order to simulate the behavior of three mixed-density groups.

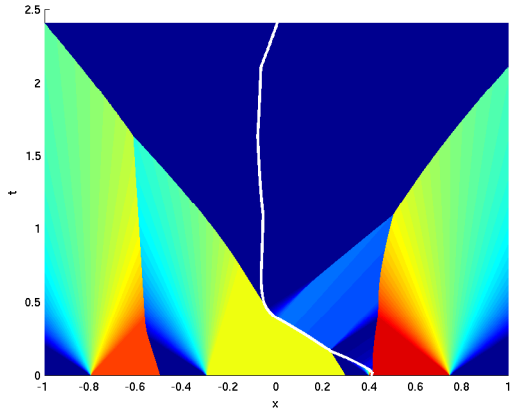

Figure 1.8: Wave front tracking scheme for u^0 given by (1.32) with $\Delta u = 2^{-10}$.

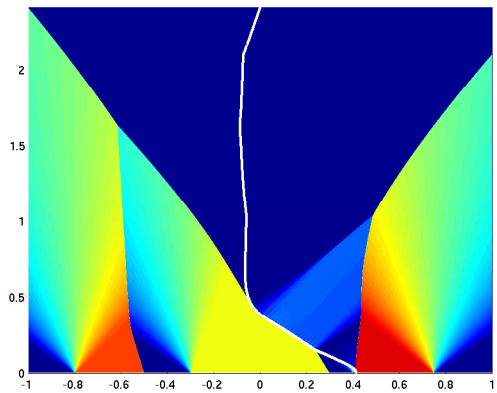

Figure 1.9: Godunov scheme for u^0 given by (1.32) with $\Delta x = 10^{-3}$.

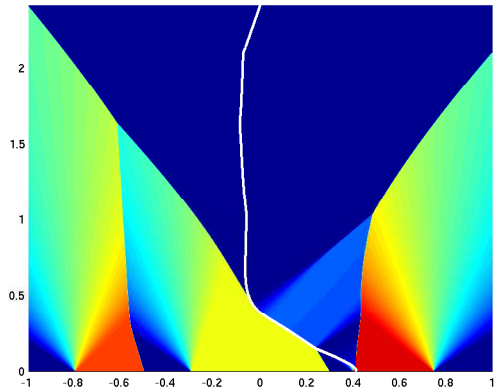

Figure 1.10: Rusanov schemes for u^0 given by (1.32) with $\Delta x = 10^{-3}$.

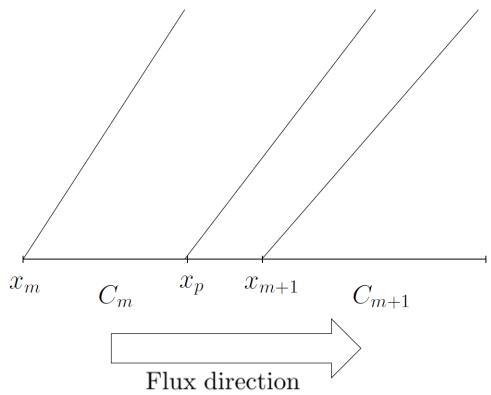

Figure 1.11: Representation of the different parameters used in the algorithm. Flux direction

We can see that the two finite volume simulations are evolving like the wave front tracking one, modeling two *turning phenomena*. We can also observe that the diffusion of Rusanov counterbalances severely Godunov's oscillations.

1.5 Numerical application: a pedestrian tracking

In paper [21], Bretti and Piccoli proposed an algorithm to trace the trajectory of a single vehicle in traffic flow. We extend this procedure to our pedestrian model with a discontinuous flux function. Assuming that the pedestrian moves according to the average speed $v = v(u)$, its trajectory will be the solution of the ordinary differential equation

$$\begin{cases} \dot{x}(t) = v(u(t, x(t))), \\ x_0 = x_p. \end{cases} \tag{1.33}$$

where $x = x(t)$ is the position of the particle at time t and x_p its position at the beginning of the time step. Its speed depends on the density u but it does not affect the density distribution, so the ODE will be weakly coupled to the PDE. The parameters are represented on the Fig. 1.11.

1.5.1 Algorithm

The model (1.1a), (1.1b) has a bidirectional flux discontinuous in $x = \xi(t)$. The computation of the pedestrian's trajectory with a concave flux will be symmetric with respect to a convex flux, so everything can be transposed to the other direction of movement.
We define x_p the position of the particle at the beginning of the time step, m the index of the cell C_m containing x_p, x_m the starting point of the wave following x_p, u_m the density in C_m, and u_{m+1} the density in the C_{m+1} cell.
At each time step we compute the new position of the pedestrian. On either side of the turning point, the flow is monotone, so that a particle can interact only with the x_{m+1} wave.

To check if the pedestrian interacts with the wave during the time step, we compute $\bar{\Delta t} = \frac{x_m - x_p}{v(u_m) - s_m}$, where

$$s_m = \begin{cases} \frac{f(u_{m+1}) - f(u_m)}{u_{m+1} - u_m} & \text{if } u_m < u_{m+1} \\ f'(u_m) & \text{if } u_m > u_{m+1} \end{cases}$$

the speed of the x_{m+1} wave, is computed. $\bar{\Delta t}$ represents the time when the particle interacts with the next wave. s_m is the speed of this wave and we distinguish two cases:

- if $\bar{\Delta t} > \Delta t$ the particle does not cross the wave. Its new position is $x_p^* = x_p + v(u_m)\Delta t$,
- if $\bar{t} < \Delta t$ we discern two additional cases:
  - if $u_m < u_{m+1}$ the wave is a shock an $x_p^* = x_p + \bar{\Delta t} v(u_m) + (\Delta t - \bar{\Delta t}) v(u_{m+1})$,
  - if $u_m > u_{m+1}$ the pedestrian interacts with a rarefaction. We have to define if at the end of the time step, the pedestrian has crossed it or it is still inside it. We define $\bar{\bar{\Delta t}}$ the time when the pedestrian exits the rarefaction wave. It is defined implicitly by

$$\frac{x(\bar{\bar{\Delta t}}) - x_m}{\bar{\bar{\Delta t}}} = f'(u_{m+1}), \tag{1.34}$$

  where $x(t) = x_m + (t - t_0) - \bar{\Delta t} \frac{\sqrt{t - t_0}}{\sqrt{\bar{\bar{\Delta t}}}} (1 - v(u_m))$ and t_0 the global time at the beginning of the time step.

The computation of the trajectory is automatic at ξ because, by assumption, it is located at the center of its cell. What matters to the computation of x_p's trajectory is the flux direction at its cell's extremities. If $x_p = \xi$, we apply the concave flux f.

1.5.2 Results

We apply the tracking algorithm to the turning situation considered in Sec. 1.4. On Fig. 1.12, the trajectory and the location of a pedestrian is depicted. At the beginning, the pedestrian chooses to move towards the left exit but he turns for an other direction when the balance of the costs changes in favor of the right one.

1.6 Conclusion

The evacuation of a crowd in a long narrow corridor with two opposite exits can be modeled by a system of partial differential equations in one space-dimension, coupling a scalar conservation law describing mass conservation and an eikonal equation assigning the direction of motion depending on the density distribution. The system can be rewritten as a scalar conservation law with space-discontinuous flux function, for which the discontinuity location depends nonlocally on the density profile.
Exact entropy weak solutions are difficult to compute even for simple initial data of Riemann type. Therefore, we have coded an adapted wave front tracking scheme, which is reasonably

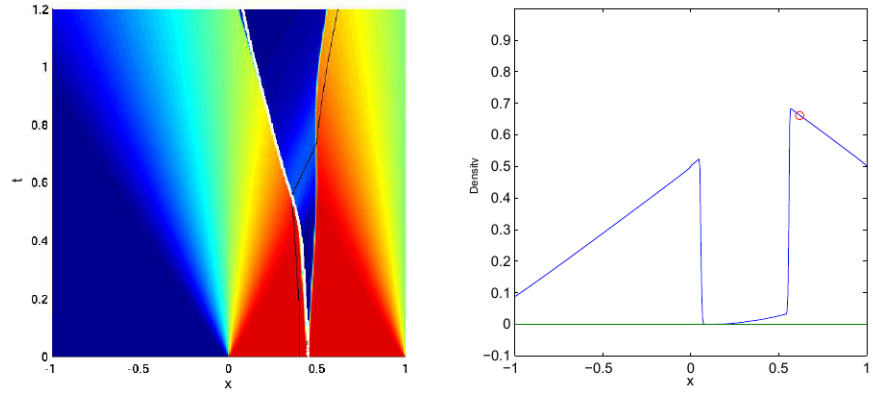

Figure 1.12: Trajectory in black during the evolution of 1.31 and its position in red circle on the density profile of a single pedestrian starting at $x_0 = 0.4$. The simulation parameters are $u^0(x) = 0$ for $x \in]-1, 0[$ and $u^0(x) = 0.9$ for $x \in]0, 1[$, $t = 1.2$ on right and $\Delta x = 0.005$.

assumed to give a good approximation of the problem's solution. These wave front tracking approximations are used as reference solutions to show numerically the convergence of classical finite volume schemes, which do not treat explicitly the dynamic at the turning point.
These results support the use of classical finite volume schemes for the computation of solutions of Hughes' model on more complex geometries in two space dimensions, see for example [55, 59].
The bound of the total variation is crucial to use Helly's theorem, and proving convergence of wave front tracking approximation is still an open question.
Being able to follow the path of a single pedestrian reveals clearly the change of direction operated by a person choosing a different exit to evacuate. The choice is made according to the evolution of the density profile during the evacuation. The evacuation at the doors makes the density decrease but the spreading of pedestrians along the corridor increases dramatically the relative cost of a travel to join the first chosen exit.

Chapter 2

A mixed-type system of conservation laws modeling crossing flows of pedestrians

Contents

2.1 Introduction **32**
2.2 Analytical study **33**
2.2.1 Rarefaction waves 35
2.2.2 Shocks 36
2.2.3 Fognals, umbilic points and crossing shocks 37
2.3 Solutions of the Riemann problem **38**
2.3.1 Description of the solution 38
2.3.2 Partial analytical proofs 42
2.4 Numerical Study **50**
2.5 Numerical results **54**
2.5.1 Distributional solutions 54
2.5.2 Measure-valued solutions 59
2.6 Conclusion **65**

2.1 Introduction

Systems of conservation laws that are not everywhere hyperbolic in the phase space arise naturally in the modeling of physical phenomena. Two well-known examples are the two-fluid single-pressure model for two-phase flow [80], and the model for three-phase porous medium flow that has been widely used in petroleum reservoir simulation [10]. It arises also in modeling two-directional traffic flows [15, 17]. These models display an elliptic region in the phase space, where the Jacobian matrix of the vector-valued flux function has complex eigenvalues. The set of all elliptic points forms the elliptic region. This type of systems has been addressed since several decades now, see [41, 61, 62] for a general overview. Nevertheless, their solutions have not been completely understood yet. The construction of nonclassical solutions involving *crossing shocks* is described. Rapidly oscillating but bounded numerical approximations suggest that solutions could be defined in the framework of Young measures [42, 43].
In this part, we consider a mixed type system of conservation laws describing two populations of pedestrians moving in opposite directions, adapted from [14, 17]. Let

$$\begin{cases} (u_1)_t + f(u_1, u_2)_x = 0, \\ (u_2)_t - f(u_2, u_1)_x = 0, \end{cases} \tag{2.1}$$

be the governing equations, together with the initial conditions

$$\begin{cases} u_1(0, x) = u_{1,0}(x), \\ u_2(0, x) = u_{2,0}(x), \end{cases} \tag{2.2}$$

where $t \in \mathbb{R}^+$, $x \in \mathbb{R}$. The flux function is therefore given by

$$\mathbf{F}(U) = \begin{pmatrix} f(u_1, u_2) \\ -f(u_2, u_1) \end{pmatrix}, \tag{2.3}$$

where $f(a, b) = a(1 - a - b)$, and $U = (u_1, u_2)$ are densities of the two groups of pedestrians that take values in

$$\Omega_u = \{(u_1, u_2) \in \mathbb{R}^2 \colon u_1 \geq 0, u_2 \geq 0 \text{ and } u_1 + u_2 \leq 1\}.$$

As announced, the main feature of system (2.1) lies in the loss hyperbolicity of for certain density values. Indeed, the Jacobian of the flux exhibits complex eigenvalues in the elliptic region $\mathcal{E}$ of the phase space Ω_u. It was suggested in [15] that oscillations arising in the elliptic region could be related to the lane formation phenomenon observed in groups of pedestrians moving in opposite directions [51, 69].
We aim to investigate solutions properties in relation with the modeled pedestrian dynamics, also relying on numerical simulations. In particular, we will study the solutions of (2.1)-(2.2) corresponding Riemann-like initial data $U^0 = (u_1^0, u_2^0)$ of the form

$$U^0(x) = \begin{cases} U_L = (u_{1,L}, u_{2,L}), & \text{if } x < 0, \\ U_R = (u_{1,R}, u_{2,R}), & \text{if } x > 0. \end{cases} \tag{2.4}$$

A similar problem was addressed by Vinod [84], who considered a slightly different version of model (2.1) including a parameter $\beta > 0$ which sensibly changes the solutions behavior,

and by Appert-Rolland et al [6], who studied an extension of the Aw-Rascle model to this situation with cyclic boundary conditions and diffusive correction.
The chapter is organized as follows. Section 2.2 contains the basic analytical study of the models properties. In Section 2.3, we propose a conjecture of the Riemann problem solution, illustrating the nonclassical solutions of mixed-type system of conservation laws. In Section 2.4, we introduce a Lax-Friedrichs finite volume scheme and we prove an $\mathbf{L}_\infty$ bound on the corresponding approximate solutions, ensuring the convergence towards Young measures. In Section 2.5 we give examples of weak solutions in distributional sense and present two examples of initial data generating persisting oscillations. Finally we give conclusions in Section 2.6.

2.2 Analytical study

This section is devoted to the study of the basic properties of system (2.1)-2.4, and to the identification of the wave types appearing in the solutions of the corresponding Riemann problem (2.1)-(2.4). This study does not pretend to be exhaustive, the problem being nonclassical and still not completely understood. In particular, we cannot give any global existence result for weak solutions, and their uniqueness is not expected. Some examples of solutions displaying the described features will be showed through numerical computations in Section 2.5.
First of all, we compute the Jacobian of the flux (2.3):

$$J(u_1,u_2) = \begin{pmatrix} 1-2u_1-u_2 & -u_1 \\ u_2 & -1+u_1+2u_2 \end{pmatrix}$$

and its characteristic polynomial

$$p(\lambda) = \lambda^2 + (u_1-u_2)\lambda - 2(u_1)^2 - 2(u_2)^2 + 3u_1 + 3u_2 - 4u_1u_2 - 1. \tag{2.5}$$

The discriminant of (2.5) is

$$\Delta(u_1,u_2) = 4 + 14u_1u_2 - 12u_1 - 12u_2 + 9(u_1)^2 + 9(u_2)^2,$$

so when it is negative, the equation loses its hyperbolicity. In the phase space, the set of densities satisfying $\{\Delta \le 0\}$ is called this region

$$\mathcal{E} = \left\{(u_1,u_2) \in \mathbb{R}^2 \colon 4 + 14u_1u_2 - 12u_1 - 12u_2 + 9(u_1)^2 + 9(u_2)^2 \le 0\right\} \subset \Omega_u,$$

see Fig. 2.1.
We call the triangular domain's sides M_1 for $[(0,0),(1,0)]$, M_2 for $[(0,0),(0,1)]$ and L for $[(1,0),(0,1)]$. Therefore the eigenvalues can take complex values:

$$\lambda_1(u_1,u_2) = \frac{1}{2}\left(u_2 - u_1 - \sqrt{4 + 14u_1u_2 - 12u_1 - 12u_2 + 9(u_1)^2 + 9(u_2)^2}\right),$$
$$\lambda_2(u_1,u_2) = \frac{1}{2}\left(u_2 - u_1 + \sqrt{4 + 14u_1u_2 - 12u_1 - 12u_2 + 9(u_1)^2 + 9(u_2)^2}\right),$$

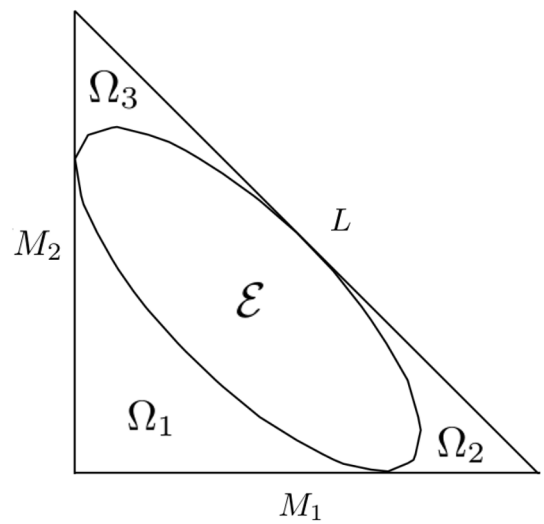

Figure 2.1: The triangular domain Ω_u, the elliptic region $\mathcal{E}$ and the sides L, M_1 and M_2.

and corresponding eigenvectors are:

$$\begin{aligned} r_1(u_1,u_2) &= 2\begin{pmatrix} u_1 \\ 1-2u_1-u_2-\lambda_1 \end{pmatrix} = \begin{pmatrix} 2u_1 \\ 2-3u_1-3u_2+\sqrt{\Delta(u_1,u_2)} \end{pmatrix} \\ &= 2\begin{pmatrix} 1-u_1-2u_2+\lambda_1 \\ u_2 \end{pmatrix} = \begin{pmatrix} 2-3u_1-3u_2-\sqrt{\Delta(u_1,u_2)} \\ 2u_2 \end{pmatrix}, \\ r_2(u_1,u_2) &= 2\begin{pmatrix} u_1 \\ 1-2u_1-u_2-\lambda_2 \end{pmatrix} = \begin{pmatrix} 2u_1 \\ 2-3u_1-3u_2-\sqrt{\Delta(u_1,u_2)} \end{pmatrix} \\ &= 2\begin{pmatrix} 1-u_1-2u_2+\lambda_2 \\ u_2 \end{pmatrix} = \begin{pmatrix} 2-3u_1-3u_2+\sqrt{\Delta(u_1,u_2)} \\ 2u_2 \end{pmatrix}. \end{aligned}$$

The gradient of the eigenvalues are:

$$\nabla\lambda_1(u_1,u_2) = \frac{1}{2}\begin{pmatrix} 1-\dfrac{9u_1+7u_2-6}{\sqrt{\Delta(u_1,u_2)}} \\ 1-\dfrac{7u_1+9u_2-6}{\sqrt{\Delta(u_1,u_2)}} \end{pmatrix},$$

$$\nabla\lambda_2(u_1,u_2) = \frac{1}{2}\begin{pmatrix} -1+\dfrac{9u_1+7u_2-6}{\sqrt{\Delta(u_1,u_2)}} \\ 1+\dfrac{7u_1+9u_2-6}{\sqrt{\Delta(u_1,u_2)}} \end{pmatrix}.$$

For seek of clarity, we recall here the notion of distributional solution.

Definition 2.2.1 *A function $U \in \mathbf{L_1}(\mathbb{R}^+ \times \mathbb{R}, \Omega_u)$ is a weak solution of* (2.1)-(2.2) *if for all*

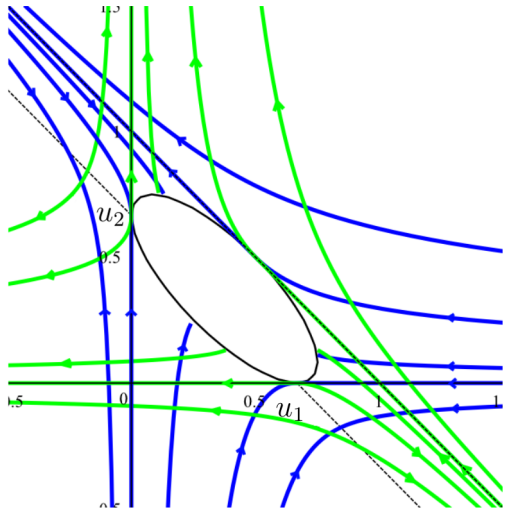

Figure 2.2: 1-rarefaction curves (dark lines), 2-rarefaction curves (fair lines) and fognals (dashed lines).

$\phi \in \mathbf{C_c^1}(\mathbb{R}^2;\mathbb{R})$ *we have*

$$\int_{\mathbb{R}^+}\int_{\mathbb{R}} \left(U\phi_t + \mathbf{F}(U)\phi_x\right)(t,x)\ \mathrm{d}x\mathrm{d}t + \int_{\mathbb{R}} U^0(x)\phi(0,x)\ \mathrm{d}x = 0.$$

Weak solutions of the Riemann problem (2.1)-(2.4) consist of a combination of rarefactions, shock waves and crossing shocks, see [58], which are described below.

2.2.1 Rarefaction waves

The solution of a Riemann problem (2.1)-(2.4) can be a *rarefaction* wave $U = U(x,t)$ of the i-th family if it reads

$$U(x,t) = \begin{cases} U_L, & \text{if} \quad x < \lambda_i(U_L)t, \\ T(x/t), & \text{if} \quad \lambda_i(U_L)t \le x \le \lambda_i(U_R)t \\ U_R, & \text{if} \quad x > \lambda_i(U_R)t, \end{cases} \tag{2.6}$$

where $T(\xi)$ satisfies

$$\dot{T} = r_i(T(\xi)),\ T(\lambda_i(U_L)) = U_L,\ T(\lambda_i(U_R)) = U_R,\ i = 1 \text{ or } i = 2. \tag{2.7}$$

Let $R_i(U_L)$ denote the solutions of (2.7). The integral curves of $r_i(U)$ are illustrated on Fig. 2.2. The arrows indicate directions of increase of the corresponding eigenvalue. The direction is reversed across specific straight lines called *fognals* $\mathcal{F}$, see Sec. 2.2.3.
Vector fields $r_i(U)$, $i = 1, 2$, oriented so that $\nabla\lambda_i \cdot r_i(U) \ge 0$, are given in Fig. 2.3, which gives the orientation of rarefaction curves.

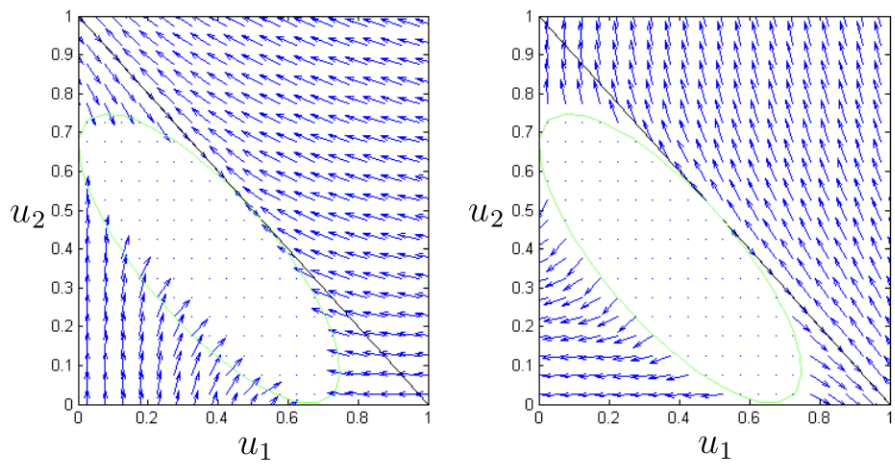

Figure 2.3: Eigenvector fields of r_1 (left) and r_2 (right) outside the elliptic region $\mathcal{E}$, oriented so that $\nabla\lambda_i \cdot r_i \geq 0$.

2.2.2 Shocks

The discontinuous function

$$U(x,t) = \begin{cases} U_L, & \text{if } x < st, \\ U_R, & \text{if } x > st. \end{cases}$$

is a weak solution of (2.1)-(2.4) called *shock* wave if and only if it satisfies the Rankine-Hugoniot relation

$$s(U_R - U_L) = \mathbf{F}(U_R) - \mathbf{F}(U_L) \tag{2.8}$$

for some speed $s = s(U_L, U_R) \in \mathbb{R}$. Given any point $U_L \in \Omega_u$, the *Hugoniot locus* [20] is defined by

$$\mathcal{H}(U_L) = \left\{ U \in \mathbb{R}^2 : \exists\, s = s(U_L, U) \in \mathbb{R} \text{ s. t. } s(U - U_L) = \mathbf{F}(U) - \mathbf{F}(U_L) \right\}.$$

A Hugoniot locus is composed of three disjoint branches. When U_L lies in the hyperbolic region, one of them has a loop closing at U_L, which crosses the elliptic region. Another branch can also cross a different hyperbolic region but the three branches can never be in Ω_u at the same time. One can see it on Fig. 2.4.

Proposition 2.2.1 *$U = (u_1, u_2)$ satisfies the Rankine-Hugoniot relation* (2.8) *if and only if*

$$\begin{aligned} u_2 =& u_{2,\pm}(u_1) = \frac{1}{2(2u_1 - u_{1,L})} \left(u_{1,L}\left(u_{1,L} + u_{2,L} - 2\right) + u_1(u_{1,L} + u_{2,L} - 2u_1 + 2) \right. \\ & \pm (u_1 - u_{1,L}) \sqrt{\left(u_{1,L} + 3u_{2,L} - 2\right)^2 + 4u_{1,L}u_{2,L} + (u_{1,L} + u_{2,L} + u_1 - 2)} \end{aligned}$$

The Hugoniot locus $\mathcal{H}(U_L)$ has an horizontal asymptote $\left\{u_2 = \frac{u_{2,L}}{2}\right\}$, a vertical asymptote $\left\{u_1 = \frac{u_{1,L}}{2}\right\}$ and an asymptote $u_1 + u_2 = 1$.

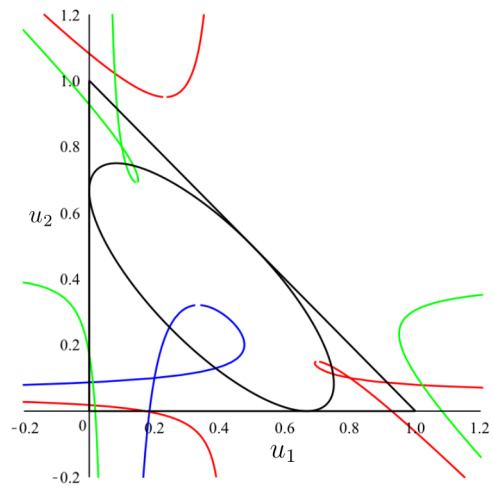

Figure 2.4: Hugoniot locus for $U_L = (0.2, 0.1)$ in blue, $U_L = (0.8, 0.1)$ in red and $U_L = (0.1, 0.8)$ in green.

Since the system is not genuinely nonlinear (and not even hyperbolic), the entropy admissible branch can be selected using the Liu-Oleinik condition [67]:

Definition 2.2.2 *$U_R \in \mathcal{H}(U_L)$ is joined to U_L by an entropy admissible shock if and only if*

$$s(U_L, U_R) \leq s(U_L, U) \tag{2.9}$$

for each $U \in \mathcal{H}(U_L)$ between U_L and U_R

Anyway, each branch section of $\mathcal{H}(U_L)$ belonging to Ω_u lies in a region were the corresponding field is genuinely non-linear, as shown in Fig. 2.4. Therefore, if U_R belongs to the same branch as U_L, condition (2.9) coincides with the usual Lax geometric condition

$$\lambda_i(U_R) \leq s(U_L, U_R) \leq \lambda_i(U_L) \quad \text{for } i = 1 \text{ or } i = 2.$$

2.2.3 Fognals, umbilic points and crossing shocks

Due to the mixed nature of system (2.1), weak solutions can display others types of discontinuity. Combinations of contact discontinuities moving with zero speed appear along *fognals*:

$$\mathcal{F} = \left\{ U \in \mathbb{R}^2 : \nabla \lambda_i(U) \cdot r_i(U) = 0 \right\}, \; i = 1, 2.$$

We define

$$\mathcal{F} = \mathcal{F}_1 \cup \mathcal{F}_2 = \left\{ (u_1, u_2) \in \mathbb{R}^2 : u_1 + u_2 = 1 \right\} \cup \left\{ (u_1, u_2) \in \mathbb{R}^2 : u_1 + u_2 = \frac{2}{3}, (u_1, u_2) \notin \mathcal{E} \right\}.$$

$\mathcal{F}$ coincides with the line $u_1 + u_2 = 1$ and crosses $\partial\mathcal{E}$ and $\partial\Omega_u$ at points called *umbilic points*. One can see the change of the orientation on the eigenvector field in Fig. 2.3 and observe

that the wave type on the u_1 and the u_2-axis changes at points $\left(\frac{2}{3},0\right)$, $\left(0,\frac{2}{3}\right)$ and $\left(\frac{1}{2},\frac{1}{2}\right)$. In particular, we will call *crossing shocks* the discontinuities satisfying

$$\Sigma(U_L) = \left\{ U \in \mathcal{H}(U_L) \colon \begin{array}{c} \lambda_1(U_L) \leq s(U_L,U) \leq \lambda_2(U_L) \\ \lambda_1(U) \leq s(U_L,U) \leq \lambda_2(U) \end{array} \right\},$$

see [58]. For example, if $U_L = (u_{1,L}, 0)$ for some $U_L \in [0, 2/3[$, we have

$$\Sigma(U_L) = \left\{ U = (u_1, 0) \colon 1 - \frac{u_{1,L}}{2} \leq u_1 \leq 2 - 2u_{1,L} \right\},$$

and for $U_L = (0, u_{2,L})$ with $u_{2,L} \in]2/3, 1]$

$$\Sigma(U_L) = \left\{ U = (0, u_2) \colon 2 - 2u_{2,L} \leq u_2 \leq 1 - \frac{u_{2,L}}{2} \right\}.$$

2.3 Solutions of the Riemann problem

The solution of the Riemann problem (2.1)-(2.4) for U_L, $U_R \in \Omega_u \setminus \mathcal{E}$ consists of various combinations of shock and rarefaction waves connecting two U_L, U_R. To describe the solution, for each fixed $U_L \in \Omega_u \setminus \mathcal{E}$ we divide the U_R plane into regions in which the solution is essentially of the same form. This is obtained by first solving locally the problem around U_L and subsequently adding new waves to the previously constructed ones, following Liu's construction in [67]. A basic fact when adding a new wave to the right of the previous one (along the x-axis) is that the speed must increase.

2.3.1 Description of the solution

We shall start the construction for $U_L \in \Omega_1$, for $U_L \in \Omega_2$ and finally for $U_L \in \Omega_3$ and recall that:

- $R_i(U)$ is the ith-rarefaction represented with dots,
- $S_i(U)$ the ith-shock with lines,
- Σ the crossing shock.

In Ω_1, we have to distinguish two specific cases depending on the position of $U_L \in \Omega_1$, see Fig. 2.5 (those two regions can overlap). The region Ω_1^a is defined as the region of U such that the loop of $\mathcal{H}(U)$ crosses the elliptic region and Ω_2, see for instance the Hugoniot curve on Fig. 2.6. The loop of $\mathcal{H}(U_L)$ adds a new region in Ω_2 allowing $1-$rarefaction-$2-$shock connections. Then Ω_1^b region is delimited by $\partial\mathcal{E}$, M_1 and $\left\{u = \frac{1}{2}\right\}$. It makes rises two regions along the L axis allowing $1-$rarefaction-$2-$shock and $1-$shock-$2-$shock connections due to the second part of the Hugoniot curve, see Fig. 2.7.

Proposition 2.3.1 *Assume $U_L \in \Omega_1$, see Fig. 2.8. Different combinations of waves compose the structure of the solution depending on the position of $U_R \in \Omega_u \setminus \mathcal{E}$. The solution is a combination of*

1. *a 1-rarefaction followed by a 2-shock for $U_R \in \Omega_1^1$. For $U_L \in \Omega_1^a$, this configuration is also admissible for $U_R \in \Omega_2^5$, see Fig 2.9;*

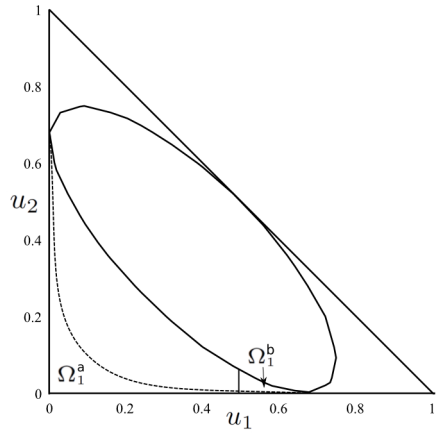

Figure 2.5: The regions Ω_1^a and Ω_1^b in Ω_1.

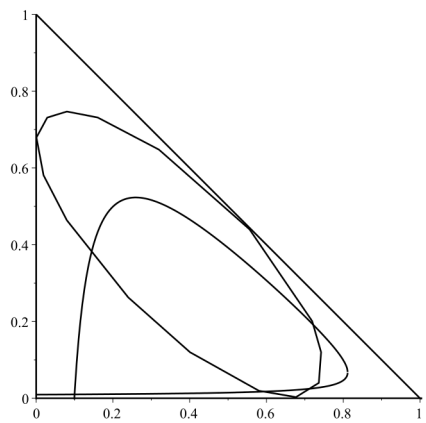

Figure 2.6: Hugoniot curve of $\mathcal{H}(0.1, 0.01)$. The curve crosses $\mathcal{E}$ and Ω_2.

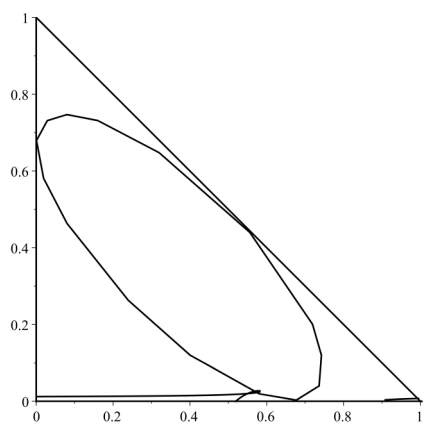

Figure 2.7: Hugoniot curve of $\mathcal{H}(0.55, 0.02)$. The curve crosses Ω_2 with a secondary branch next to $(1, 0)$.

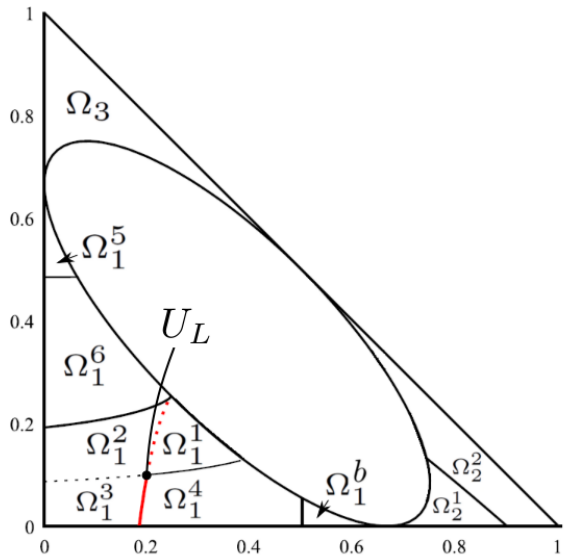

Figure 2.8: Partitioning of $\Omega_u \setminus \mathcal{E}$, corresponding to the solution of the Riemann problem with $U_L \in \Omega_1/(\Omega_1^a \cup \Omega_1^b)$.

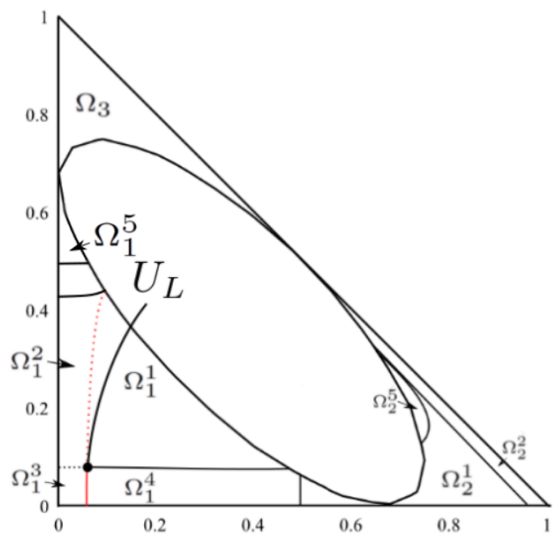

Figure 2.9: Partitioning of $\Omega_u \setminus \mathcal{E}$, corresponding to the solution of the Riemann problem with $U_L \in \Omega_1^a$. Ω_1^6 is not depicted.

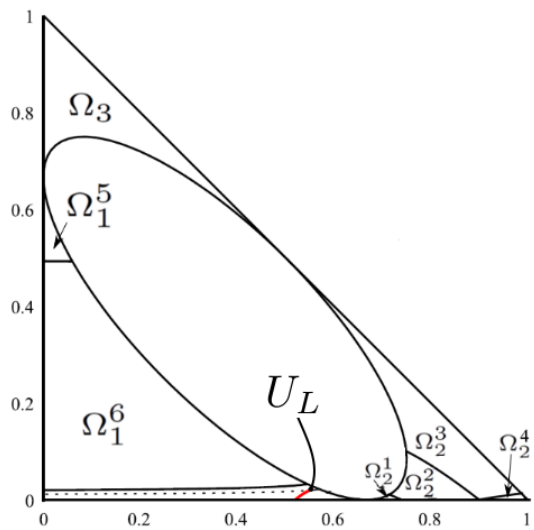

Figure 2.10: Partitioning of $\Omega_u \setminus \mathcal{E}$, corresponding to the solution of the Riemann problem with $U_L \in \Omega_1^b$. Some regions of Ω_1 are to small to be depicted.

2. *a* 1*-rarefaction followed by a* 2*-rarefaction for* $U_R \in \Omega_1^2$*. The region is bounded above by the* 2*-rarefaction coming from the intersection of* $R_1(U_L)$ *and* $\partial\mathcal{E}$*, see Fig 2.10;*

3. *a* 1*-shock followed by a* 2*-rarefaction for* $U_R \in \Omega_1^3$*. For* $U_L \in \Omega_1^b$*, this configuration is also admissible for* $U_R \in \Omega_2^4$*, see Fig 2.10;*

4. *a* 1*-shock followed by a* 2*-shock for* $U_R \in \Omega_1^4 \cup \Omega_1^b \cup \Omega_2^1$*. For* $U_L \in \Omega_1^b$*, this configuration is also admissible for* $U_R \in \Omega_2^3$*, see Fig 2.10;*

5. *a* 1*-shock, a* Σ*-shock followed by a* 2*-shock for* $U_R \in \Omega_2^2$*;*

6. *a* 1*-shock, a* Σ*-shock towards* $(1,0)$*, followed by a contact discontinuity and by a* 2*-shock for* $U_R \in \Omega_3 \cup \Omega_1^5$*,*

7. *a* 1*-shock, three* Σ*-shocks through* $(1,0)$ *and* $(0,1)$*, followed by a* 2*-shock for* $U_R \in \Omega_1^6$*. Indeed, the solution runs along* M_1*,* L *and* M_2*.*

Proposition 2.3.2 *Assume* $U_L \in \Omega_2$*, see Fig. 2.11. The solution is a combination of*

1. *a* 1*-rarefaction followed by a* 2*-shock for* $U_R \in \Omega_2^1$*;*

2. *a* 1*-rarefaction followed by a* 2*-rarefaction for* $U_R \in \Omega_2^2$*;*

3. *a* 1*-shock followed by a* 2*-rarefaction for* $U_R \in \Omega_2^3$*;*

4. *a* 1*-shock followed by a* 2*-shock for* $U_R \in \Omega_2^4$*;*

5. *a* 1*-shock, a contact discontinuity followed by a* 2*-shock for* $U_R \in \Omega_3 \cup \Omega_1^2$*;*

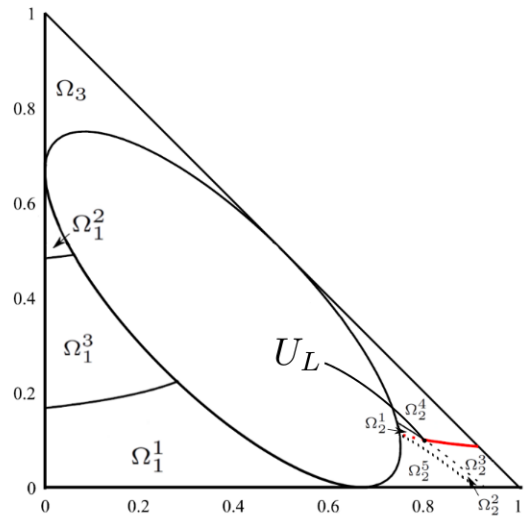

Figure 2.11: Partitioning of $\Omega_u \setminus \mathcal{E}$, corresponding to the solution of the Riemann problem with $U_L \in \Omega_2$.

6. *a* 1*-shock, a contact discontinuity followed by a crossing shock by a* 2*-shock for* $U_R \in \Omega_1^1 \cup \Omega_2^5$.

Proposition 2.3.3 *Assume* $U_L \in \Omega_3$*, see Fig. 2.12. The solution is a combination of*

1. *a* 1*-rarefaction followed by a* 2*-shock for* $U_R \in \Omega_3^1$*;*
2. *a* 1*-rarefaction followed by a* 2*-rarefaction for* $U_R \in \Omega_2^3$*;*
3. *a* 1*-shock followed by a* 2*-rarefaction for* $U_R \in \Omega_3^3$*;*
4. *a* 1*-shock followed by a* 2*-shock for* $U_R \in \Omega_3^4 \cup \Omega_1^2 \cup \Omega_2$*. For* $U_R \in \Omega_2$*, the intersection lies in* Ω_1*;*
5. *a* 1*-shock, a* Σ*-shock followed by a* 2*-shock for* $U_R \in \Omega_1^3$*;*
6. *a* 1*-shock, a contact discontinuity followed by a* 2*-shock for* $U_R \in \Omega_3^5$.

2.3.2 Partial analytical proofs

To prove the admissibility of a solution, the speed of waves must have increasing values. The following part focus on Riemann problem between U_L and U_R involving a crossing shock. It consists in solutions connecting a left state U_L to an intermediary state U_1 through $1-$shock then to a right state U_R through a crossing shock or conversely a crossing shock then a $2-$shock. Rarefactions and general shocks are not developed here since the detail of their expressions lead to complex computations.

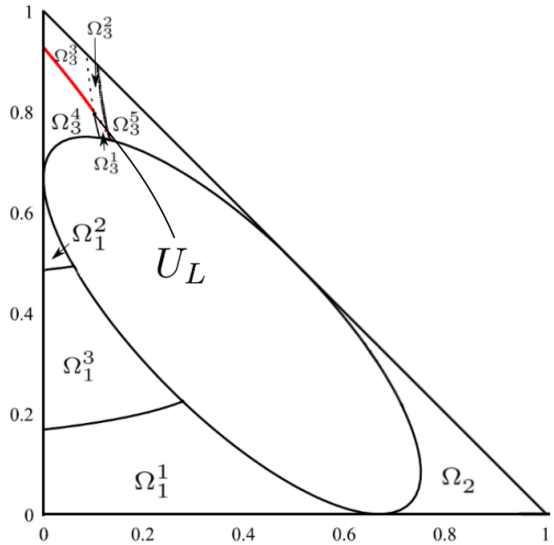

Figure 2.12: Partitioning of $\Omega_u \setminus \mathcal{E}$, corresponding to the solution of the Riemann problem with $U_L \in \Omega_3$.

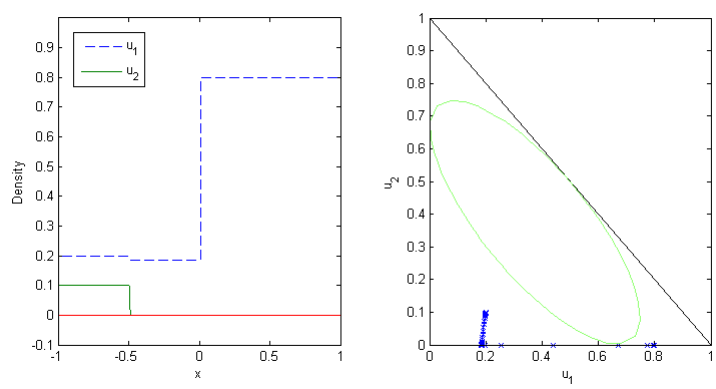

Figure 2.13: Density distribution at $T = 0.7$ for $U_L = (0.2, 0.1)$ and $U_R = (0.8, 0)$

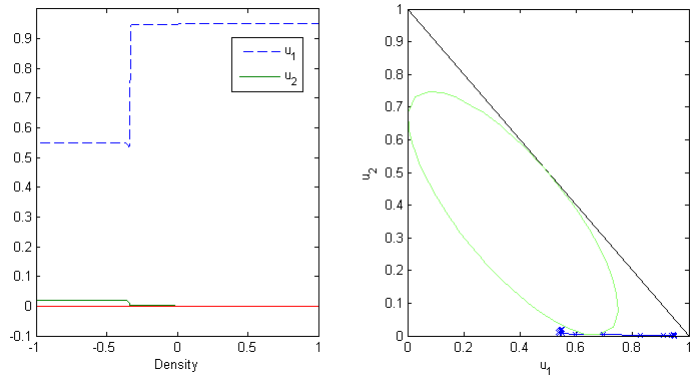

Figure 2.14: Density distribution at $T = 0.7$ for $U_L = (0.55, 0.02)$ and $U_R = (0.95, 0)$

Proof We are interested in $\Sigma-$shocks on M_1.

a. Suppose we can connect $U_L = (u_{L,1}, u_{L,2}) \in \Omega_1 \setminus M_1$ to $U_R = (u_{R,1}, 0) \in \Omega_2 \cap M_1$ with the intermediate state $U_1 = (u_{1,1}, 0) \in \Omega_1 \cap M_1$ s.t. $u_{1,1} \leq u_{1,L}$. We have a $1-$shock with speed $s_1 = -1 + u_{1,L} + u_{2,L}$ followed by a crossing shock with speed $s_\Sigma = 1 - u_{1,1} - u_{1,R}$, see Fig. 2.13.

To be admissible, this configuration should verify $s_1 - s_\Sigma < 0$. We want an expression of $u_{1,1}$. We know that if U_L and $U = (u_1, 0)$ satisfy (2.8), we can write, where $u_{1,\pm}$ stands for the union of the two curves representing the Hugoniot locus $\mathcal{H}(U_L)$.

$$u_{1,\pm}(0) = 1 - \frac{u_{1,L}}{2} - \frac{u_{2,L}}{2} \pm \frac{1}{2}\sqrt{(3u_{1,L} + u_{2,L} - 2)^2 + 4u_{1,L}u_{2,L}}.$$

which are the two abscissae of the intersections of the Hugoniot curve with M_1. $u_{1,1}$ is the smallest one, so $u_{1,1} = u_{1,-}(0)$.

so

$$\begin{aligned} s_1 - s_\Sigma &= -1 + \frac{u_{1,L}}{2} + \frac{u_{2,L}}{2} - \frac{1}{2}\sqrt{(3u_{1,L} + u_{2,L} - 2)^2 + 4u_{1,L}u_{2,L}} + u_{1,R} \\ &= u_{1,R} - u_{1,+}(0) \end{aligned}$$

therefore

$$s_1 - s_\Sigma < 0 \Leftrightarrow u_{1,R} < u_{1,+}(0).$$

$u_{1,+}(0)$ is the threshold above which $u_{1,R}$ does not make any admissible connections with $u_{1,L}$ anymore. This value is smaller than 1 for $u_{1,L} \geq 1/2$, bringing the specific treatment of the $U_L \in \Omega_1^b$ case with the region Ω_2^3 and Ω_2^4 rising in Prop 2.3.1, see Fig. 2.14.

$$\begin{aligned} & u_{1,+}(0) \leq 1 \\ \Leftrightarrow\ & -u_{1,L} - u_{2,L} + \sqrt{(3u_{1,L} + u_{2,L} - 2)^2 + 4u_{1,L}u_{2,L}} \leq 0 \\ \Leftrightarrow\ & (3u_{1,L} + u_{2,L} - 2)^2 + 4u_{1,L}u_{2,L} \leq (u_{1,L} + u_{2,L})^2 \\ \Leftrightarrow\ & 4(-1 + u_{1,L} + u_{2,L})(2u_{1,L} - 1) \leq 0 \end{aligned}$$

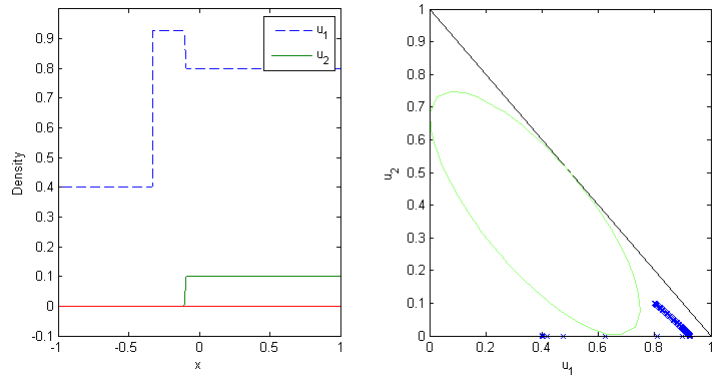

Figure 2.15: Density distribution at $T = 1$ for $U_L = (0.4, 0)$ and $U_R = (0.8, 0.1)$

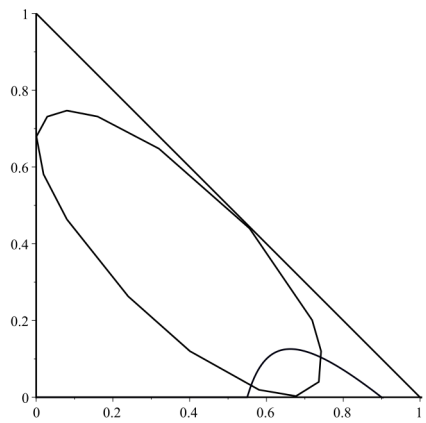

Figure 2.16: Hugoniot curve $\mathcal{H}(0.9, 0)$.

For $2u_{1,L} - 1 \geq 0$ the expression above is negative. The frontier between Ω_2^2 and $\Omega_2^3 \cap \Omega_2^4$ is $\mathcal{H}(u_{1,+}(0), 0) \cap \Omega_2$, see Figs. (2.10,2.16).

Suppose we can connect $U_L = (u_{L,1}, 0) \in \Omega_1 \cap M_1$ to $U_R = (u_{R,1}, u_{R,2}) \in \Omega_2 \backslash M_2$ with the intermediate state $U_1 = (u_{1,1}, 0) \in \Omega_1 \cap M_1$, s.t. $u_{1,1} < u_{L,1}$. We have a crossing shock with speed $s_\Sigma = 1 - u_{L,1} - u_{2,L}$ followed by a $2-$shock with speed $s_2 = -1 + u_{2,R} + u_{2,1}$, see Fig. 2.15.

To be admissible, this configuration should verify $s_\Sigma - s_2 < 0$. We want an expression of $u_{1,1}$. We know that if U_L and $U = (u_1, 0)$ satisfy (2.8), we can write, where $u_{1,\pm}$ stands for the union of the two curves representing the Hugoniot locus $\mathcal{H}(U_R)$.

$$u_{1,\pm}(0) = 1 - \frac{u_{1,R}}{2} - \frac{u_{2,R}}{2} \pm \frac{1}{2}\sqrt{(3u_{1,R} + u_{2,R} - 2)^2 + 4u_{1,R}u_{2,R}}$$

which are the two abscissae of the intersections of the Hugoniot curve with M_1. $u_{1,1}$ is the greatest one, so $u_{1,1} = u_{1,+}(0)$.

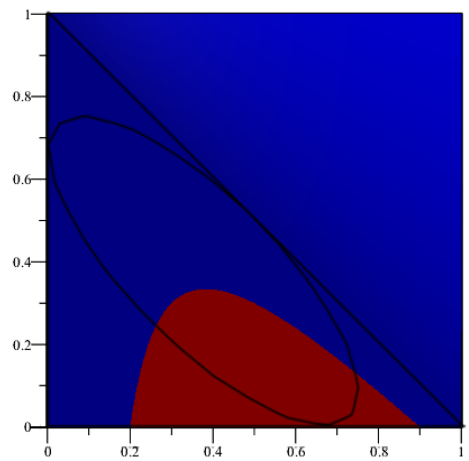

Figure 2.17: Sign of $P(U_R)$ for $U_L = (0.2, 0)$. Blue is the positive region and red is the negative one.

We bring the study of this expression to the one of a second order polynomial.

$$\begin{aligned}
s_\Sigma - s_2 = 1 - u_{1,L} - \frac{u_{1,R}}{2} - \frac{u_{2,R}}{2} - \frac{1}{2}\sqrt{(3u_{1,R} + u_{2,R} - 2)^2 + 4u_{1,R}u_{2,R}} < 0 \\
\Leftrightarrow 2 - 2u_{1,L} - u_{1,R} - u_{2,R} < \sqrt{(3u_{1,R} + u_{2,R} - 2)^2 + 4u_{1,R}u_{2,R}} \\
\Leftrightarrow (3u_{1,R} + u_{2,R} - 2)^2 + 4u_{1,R}u_{2,R} < (2 - 2u_{1,L} - u_{1,R} - u_{2,R})^2 \\
\Leftrightarrow 0 < 2u_{1,R}^2 - u_{1,L}^2 + 2u_{1,R}u_{2,R} - u_{1,L}u_{2,R} - u_{1,L}u_{1,R} - 2u_{1,R} + 2u_{1,L}
\end{aligned}$$

We call the last expression $P(U_R) := 2u_{1,R}^2 - u_{1,L}^2 + 2u_{1,R}u_{2,R} - u_{1,L}u_{2,R} - u_{1,L}u_{1,R} - 2u_{1,R} + 2u_{1,L}$. The curve $\{P(U_R) = 0\}$ is a continuous curve and $\{P(U_R) = 0\} \cap \Omega_2$ draws the frontier between Ω_2^1 and Ω_2^2 in Prop 2.3.1, see Fig. 2.17.

Consider $U_A = (1, 0)$ and $U_B = (2/3, 0)$. $P(1, 0) = -u_{1,L}(1 - u_{1,L}) > 0$ so $\{P(U_R) > 0\} \cap \Omega_2 = \Omega_2^2$. $P(2/3, 0) = -\left(u_{1,L} - \frac{2}{3}\right)^2 < 0$ so $\{P(U_R) < 0\} \cap \Omega_2 = \Omega_2^1$.

□

b. **Proof** We are interested in $\Sigma-$shocks on L.

a. Suppose we can connect $U_L = (u_{L,1}, u_{L,2}) \in \Omega_2 \setminus L$ to $U_R = (u_{R,1}, 1 - u_{R,1}) \in \Omega_3 \cap L$ with the intermediate state $U_1 = (u_{1,1}, 1 - u_{1,1}) \in \Omega_2 \cap L$, s.t. $u_{1,L} < u_{1,1}$. We have a $1-$shock with speed $s_1 = \frac{u_{1,L}(1-u_{1,L}-u_{2,L})}{u_{1,L}-u_{1,1}}$ followed by a contact discontinuity with speed $s_\Sigma = 0$, see Fig. 2.18.

To be admissible, this configuration should verify $s_1 - s_\Sigma = s_1 < 0$. We have

- $u_{1,L} > 0$,
- $1 - u_{1,L} - u_{2,L} > 0$,

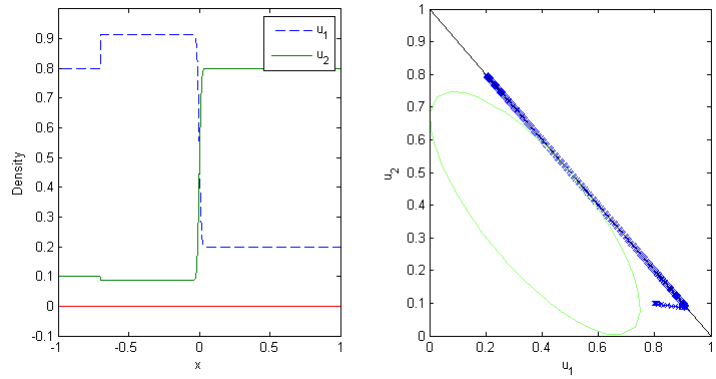

Figure 2.18: Density distribution at $T = 1$ for $U_L = (0.8, 0.1)$ and $U_R = (0.8, 0.2)$

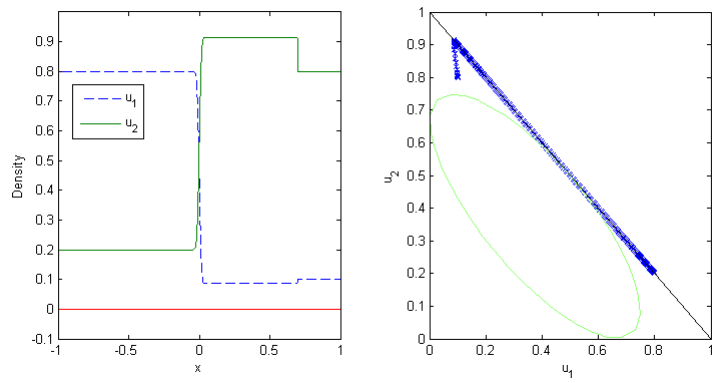

Figure 2.19: Density distribution at $T = 1$ for $U_L = (0.2, 0.8)$ and $U_R = (0.1, 0.8)$

- $u_{1,L} - u_{1,1} < 0$

so this configuration is admissible.

b. Suppose we can connect $U_L = (u_{L,1}, 1-u_{L,1}) \in \Omega_2 \cap L$ to $U_R = (u_{R,1}, u_{R,2}) \in \Omega_3 \setminus L$ with $U_1 = (u_{1,1}, 1 - u_{1,1}) \in \Omega_3 \cap L$, s.t. $u_{1,1} < u_{1,R}$. We have a contact discontinuity with speed $s_\Sigma = 0$ followed by a $2-$shock with speed $s_2 = \frac{u_{1,R}(1-u_{1,R}-u_{2,R})}{u_{1,R}-u_{1,1}}$, see Fig. 2.19.

To be admissible, this configuration should verify $s_\Sigma - s_2 = s_2 < 0$. We have

- $u_{1,R} > 0$,
- $1 - u_{1,R} - u_{2,R} > 0$,
- $u_{1,R} - u_{1,1} > 0$

so this configuration is admissible.

□

Proof We are interested in $\Sigma-$shocks on M_2.

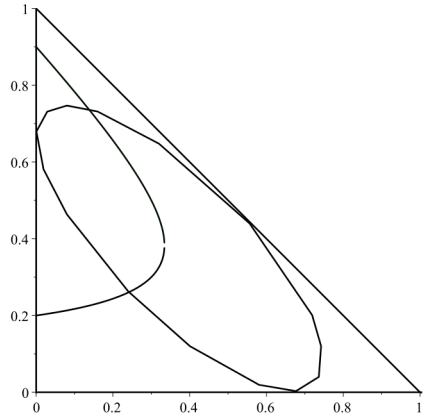

Figure 2.20: Hugoniot curve $\mathcal{H}(0, 0.2)$.

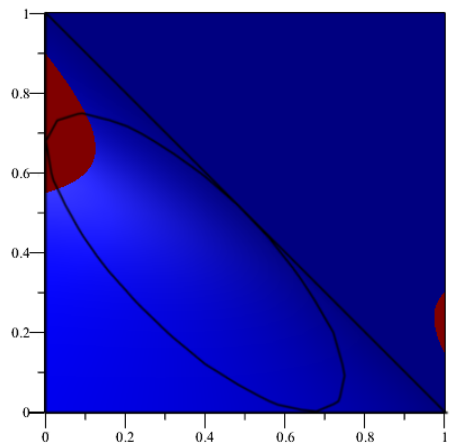

Figure 2.21: Sign of $P_{\text{bis}}(U_R)$ for $U_L = (0, 0.8)$. Blue is the positive region and red is the negative one.

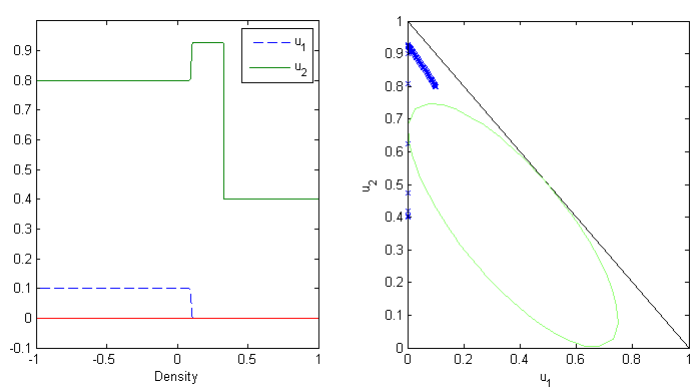

Figure 2.22: Density distribution at $T = 1$ for $U_L = (0.1, 0.8)$ and $U_R = (0, 0.4)$

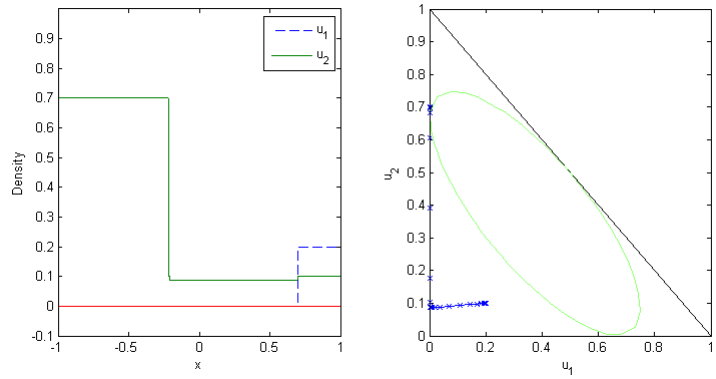

Figure 2.23: Density distribution at $T = 1$ for $U_L = (0, 0.7)$ and $U_R = (0.2, 0.1)$

a. Suppose we can connect $U_L = (u_{L,1}, u_{L,2}) \in \Omega_2 \setminus L$ to $U_R = (u_{R,1}, 1 - u_{R,1}) \in \Omega_3 \cap L$ with the intermediate state $U_1 = (u_{1,1}, 1 - u_{1,1}) \in \Omega_2 \cap L$, s.t. $u_{1,L} < u_{1,1}$. We have a $1-$shock with speed $s_1 = \frac{u_{1,L}(1-u_{1,L}-u_{2,L})}{u_{1,L}-u_{1,1}}$ followed by a contact discontinuity with speed $s_\Sigma = 0$, see Fig. 2.22.

a. Suppose we can connect $U_L = (u_{L,1}, u_{L,2}) \in \Omega_3 \setminus M_2$ to $U_R = (0, u_{R,2}) \in \Omega_2 \cap M_2$ with $U_1 = (u_{1,1}, u_{1,2}) \in \Omega_3 \cap M_2$, s.t. $u_{2,L} < u_{1,2}$. We have a $1-$shock with speed $s_1 = 1 - u_{1,L} - u_{2,L}$ followed by a crossing shock with speed $s_\Sigma = -1 + u_{1,2} + u_{2,R}$.

To be admissible, this configuration should verify $s_1 - s_\Sigma < 0$. By Prop 2.2.1, $u_{1,1} = u^+_{1,1}(0)$ brings to

$$\begin{aligned} s_1 - s_\Sigma =& 1 - \frac{u_{1,L}}{2} - \frac{u_{2,L}}{2} - u_{2,R} - \frac{1}{2}\sqrt{(u_{1,L} + 3u_{2,L} - 2)^2 + 4u_{1,L}u_{2,L}} < 0 \\ \Leftrightarrow& 1 - \frac{u_{1,L}}{2} - \frac{u_{2,L}}{2} - \frac{1}{2}\sqrt{(u_{1,L} + 3u_{2,L} - 2)^2 + 4u_{1,L}u_{2,L}} < u_{2,R} \\ \Leftrightarrow& u^-_{1,1}(0) < u_{2,R} \end{aligned}$$

So if $u_{2,R}$ is above this threshold, the configuration $S_1\Sigma$ between U_L and U_R is admissible. $\mathcal{H}(u^-_{1,1}(0), 0) \cap \Omega_1$ makes the boundary of Ω^3_1 in Ω^1_1, see Fig 2.20.

b. Suppose we can connect $U_L = (u_{L,1}, u_{L,2}) \in \Omega_3 \setminus M_2$ to $U_R = (0, u_{R,2}) \in \Omega_2 \cap M_2$ with $U_1 = (u_{1,1}, u_{1,2}) \in \Omega_3 \cap M_2$, s.t. $u_{2,L} < u_{1,2}$. We have a $1-$shock with speed $s_1 = 1 - u_{1,L} - u_{2,L}$ followed by a crossing shock with speed $s_\Sigma = -1 + u_{1,2} + u_{2,R}$, see Fig. 2.23.

Suppose we can connect $U_L = (0, u_{L,2}) \in \Omega_3 \cap M_2$ to $U_R = (u_{R,1}, u_{R,2}) \in \Omega_1 \setminus M_2$ with $U_1 \in \Omega_1 \cap M_2$, s.t. $u_{2,1} < u_{2,R}$. We have crossing shock with speed $s_\Sigma = -1 + u_{2,L} + u_{2,1}$ a $2-$shock followed by a with speed $s_2 = 1 - u_{1,R} - u_{2,R}$.

To be admissible, this configuration must verify $s_\Sigma - s_2 < 0$. By Prop 2.2.1, we get

$$\begin{aligned}
&s_\Sigma - s_2 < 0\\
&\Leftrightarrow 1 - u_{2,L} - \frac{u_{1,R}}{2} - \frac{u_{2,R}}{2} + \frac{1}{2}\sqrt{(u_{1,R} + 3u_{2,R} - 2)^2 + 4u_{1,R}u_{2,R}} < 0\\
&\Leftrightarrow (u_{1,R} + 3u_{2,R} - 2)^2 + 4u_{1,R}u_{2,R} < (2 - 2u_{2,L} - u_{1,R} - u_{2,R})^2\\
&\Leftrightarrow 2u_{2,R}^2 + 2u_{1,R}u_{2,R} - u_{2,L}u_{1,R} - u_{2,L}u_{2,R} - 2u_{2,R} - u_{2,L}^2 + 2u_{2,L} < 0.
\end{aligned}$$

We call $P_{\text{bis}}(U_R)$ this second order polynomial in U_R and by using a similar argument as in Proof 2.3.2.b, we have $(\{P_{\text{bis}}(U_R) > 0\} \cap \Omega_1) \setminus \Omega_1^1 = \Omega_3^1$ and $\{P_{\text{bis}}(U_R) < 0\} \cap \Omega_1 = \Omega_1^2$ in Prop 2.3.3, see Fig 2.21.

□

2.4 Numerical Study

We take a space step Δx and a time step Δt subject to a CFL condition which will be specified later in (1.26). For $j \in \mathbb{Z}$ and $n \in \mathbb{N}$, let $x_{j+1/2} = j\Delta x$ be the cells interface, $x_j = (j - 1/2)\Delta x$ the cells center and $t^n = n\Delta t$ the time discretization. We want to construct a finite volume approximate solution of (2.1)-(2.4) of the form $U_\Delta(t,x) = U_j^n = (u_{1,j}^n, u_{2,j}^n)$ for $(t,x) \in C_j^n = [t^n, t^{n+1}[\times[x_{j-1/2}, x_{j+1/2}[$. We use the following Lax-Friedrichs scheme:

$$\begin{aligned}
u_{1,i}^{n+1} &= u_{1,i}^n - \frac{\Delta t}{\Delta x}[F^1(u_{1,i}^n, u_{2,i}^n; u_{1,i+1}^n, u_{2,i+1}^n)\\
&\quad - F^1(u_{1,i-1}^n, u_{2,i-1}^n; u_{1,i}^n, u_{2,i}^n)],\\
u_{2,i}^{n+1} &= u_{2,i}^n - \frac{\Delta t}{\Delta x}[F^2(u_{1,i}^n, u_{2,i}^n; u_{1,i+1}^n, u_{2,i+1}^n)\\
&\quad - F^2(u_{1,i-1}^n, u_{2,i-1}^n; u_{1,i}^n, u_{2,i}^n)],
\end{aligned} \tag{2.10}$$

with the numerical flux $F = (F^1, F^2)$ defined by

$$\begin{aligned}
F^1(a_1, b_1; a_2, b_2) &= \frac{f(a_1, b_1) + f(a_2, b_2)}{2} - \frac{\alpha}{2}(a_2 - a_1),\\
F^2(a_1, b_1; a_2, b_2) &= -\frac{f(b_1, a_1) + f(b_2, a_2)}{2} - \frac{\alpha}{2}(b_2 - b_1),
\end{aligned} \tag{2.11}$$

for $\alpha \geq 1$. We prove by induction that the domain Ω_u is invariant for (2.10)-(2.11)

Lemma 2.4.1 *Under the Courant-Friedrichs-Lewy (CFL) stability condition*

$$\Delta t \leq \frac{\Delta x}{\alpha}, \quad \alpha \geq 1, \tag{2.12}$$

for any initial data $U_{\Delta,0} \in \Omega_u$ the approximate solutions computed by scheme (2.10)-(2.11) *satisfy the following uniform bounds:*

$$U_j^n = (u_{1,j}^n, u_{2,j}^n) \in \Omega_u \quad \forall j \in \mathbb{Z},\ n \in \mathbb{N}.$$

Proof We proceed by induction: assuming that $u^n_{1,j} \geq 0$, $u^n_{2,j} \geq 0$ and $u^n_{1,j} + u^n_{2,j} \leq 1$ for all $j \in \mathbb{Z}$, we show that the same holds for $u^{n+1}_{1,j}$ and $u^{n+1}_{2,j}$.

To prove positiveness, we focus on the u_1 component, the procedure being similar for u_2. Dropping the index n, we compute

$$\begin{aligned}
u^{n+1}_{1,i} &= u_{1,i} - \frac{\Delta t}{2\Delta x}\left[f(u_{1,i+1}, u_{2,i+1}) - f(u_{1,i-1}, u_{2,i-1})\right] \\
&-\frac{\alpha \Delta t}{2\Delta x}(-u_{1,i-1} + 2u_{1,i} - u_{1,i+1}) \\
&= \left(1 - \alpha\frac{\Delta t}{\Delta x}\right) u_{1,i} + \frac{\alpha \Delta t}{2\Delta x}\left(u_{1,i-1} + u_{1,i+1}\right) \\
&+\frac{\Delta t}{2\Delta x}\left[f(u_{1,i-1}, u_{2,i-1}) - f(u_{1,i+1}, u_{2,i+1})\right] \\
&= \left(1 - \alpha\frac{\Delta t}{\Delta x}\right) u_{1,i} + \frac{\Delta t}{2\Delta x}\left[u_{1,i-1}(\alpha + 1 - u_{1,i-1} - u_{2,i-1})\right. \\
&\left. + u_{1,i+1}(\alpha - 1 + u_{1,i+1} + u_{2,i+1})\right].
\end{aligned}$$

By assumption $1 - u_{1,i-1} - u_{2,i-1} \geq 0$, $\alpha \geq 1 - u_{1,i+1} - u_{2,i+1}$ and $1 - \alpha\frac{\Delta t}{\Delta x} \geq 0$ by (2.12), ensuring $u^{n+1}_i \geq 0$.

To prove $u^{n+1}_{1,i} + u^{n+1}_{2,i} \leq 1$, we observe that

$$f(a,b) - f(b,a) = (a-b)(1-a-b) = a(1-a) - b(1-b),$$

and we compute (dropping again the index n)

$$\begin{aligned}
&u^{n+1}_{1,i} + u^{n+1}_{2,i} = \\
&= u_{1,i} + u_{2,i} \\
&\quad + \frac{\alpha \Delta t}{2\Delta x}\left(-u_{1,i-1} + 2u_{1,i} - u_{1,i+1} - u_{2,i-1} + 2u_{2,i} - u_{2,i+1}\right) \\
&\quad - \frac{\Delta t}{2\Delta x}\left[f(u_{1,i+1}, u_{2,i+1}) - f(u_{2,i+1}, u_{1,i+1})\right. \\
&\quad \left. -f(u_{1,i-1}, u_{2,i-1}) + f(u_{2,i-1}, u_{1,i-1})\right] \\
&= \left(1 - \alpha\frac{\Delta t}{\Delta x}\right)(u_{1,i} + u_{2,i}) + \frac{\alpha \Delta t}{2\Delta x}\left(u_{1,i-1} + u_{1,i+1} + u_{2,i-1} + u_{2,i+1}\right) \\
&\quad - \frac{\Delta t}{2\Delta x}\left[(u_{1,i+1} - u_{2,i+1})(1 - u_{1,i+1} - u_{2,i+1})\right. \\
&\quad \left. -(u_{1,i-1} - u_{2,i-1})(1 - u_{1,i-1} - u_{2,i-1})\right]
\end{aligned}$$

$$
\begin{aligned}
&= \left(1-\alpha\frac{\Delta t}{\Delta x}\right)(u_{1,i}+u_{2,i}) \\
&\quad + \frac{\Delta t}{2\Delta x}\left[\alpha(u_{1,i-1}+u_{2,i-1})+(u_{1,i-1}-u_{2,i-1})(1-u_{1,i-1}-u_{2,i-1})\right] \\
&\quad + \frac{\Delta t}{2\Delta x}\left[\alpha(u_{1,i+1}+u_{2,i+1})-(u_{1,i+1}-u_{2,i+1})(1-u_{1,i+1}-u_{2,i+1})\right] \\
&= \left(1-\alpha\frac{\Delta t}{\Delta x}\right)(u_{1,i}+u_{2,i}) \\
&\quad + \frac{\Delta t}{2\Delta x}\left[u_{1,i-1}(\alpha+1-u_{1,i-1})+u_{2,i-1}(\alpha-1+u_{2,i-1})\right] \\
&\quad + \frac{\Delta t}{2\Delta x}\left[u_{1,i+1}(\alpha-1+u_{1,i+1})+u_{2,i+1}(\alpha+1-u_{2,i+1})\right].
\end{aligned}
$$

Using the hypothesis that $\alpha \geq 0$, $0 \leq (1-u_1), (1-u_2) \leq 1$, we get

$$
u_{1,i}^{n+1} + u_{2,i}^{n+1} \leq \left(1-\alpha\frac{\Delta t}{\Delta x}\right) + \alpha\frac{\Delta t}{2\Delta x} + \alpha\frac{\Delta t}{2\Delta x} = 1,
$$

therefore concluding the proof.

□

The uniform $\mathbf{L}_\infty$ bound provided by Lemma 2.4.1 ensures the convergence towards Young measures, which are weak-$*$ measurable maps $\nu : \mathbb{R}^+ \times \mathbb{R} \to \mathcal{P}(\mathbb{R}^2)$, where $\mathcal{P}(\mathbb{R}^2)$ denotes the space of probability measures on $\mathbb{R}^2$, see [81].
Relying on Young measures, DiPerna [36] introduced the concept of *measure-valued solutions.*

Definition 2.4.1 *Let $\mathcal{P}(\mathbb{R}^2)$ denotes the space of probability measures on $\mathbb{R}^2$. A measure-valued solution of (2.1-2.4) is a measurable map $\nu : \mathbb{R}^+ \times \mathbb{R} \to \mathcal{P}(\mathbb{R}^2)$ such that for all $\phi \in \mathbb{C}_c^1(\mathbb{R}^2;\mathbb{R})$ we have*

$$
\int_{\mathbb{R}^+}\int_{\mathbb{R}} \left(\langle \nu_{t,x}, \boldsymbol{Id}\rangle \phi_t + \langle \nu_{t,x}, \mathbf{F}\rangle \phi_x\right) \mathrm{d}x\mathrm{d}t + \int_{\mathbb{R}} U^0(x)\phi(0,x)\,\mathrm{d}x = 0. \tag{2.13}
$$

where $\boldsymbol{Id}$ stands for the identity operator.

Theorem 2.4.2 *Let U_Δ be a sequence of approximate solutions of (2.1-2.4) constructed by the scheme (2.10-2.11). Then there exists a subsequence, still denoted by U_Δ, and a Young measure ν with $\mathrm{supp}(\nu_{t,x}) \subset \overline{\Omega}_u$ such that*

$$
h(U_\Delta) \overset{*}{\rightharpoonup} \langle \nu_{t,x}, h\rangle := \int_{\mathbb{R}^2} h(\lambda)\,\mathrm{d}\nu_{t,x}(\lambda) \quad \text{in } \mathbf{L}_\infty(\mathbb{R}^+\times\mathbb{R};\mathbb{R}^2) \tag{2.14}
$$

for all $h \in \mathbf{C}(\mathbb{R}^2;\mathbb{R})$.
Moreover, ν is a measure-valued solution of (2.1-2.4) in the sense of Definition 2.4.1.

Proof The convergence to a Young measure is classical, see [81]. Here we show that the limits of Lax-Friedrichs approximations are indeed measure-valued solutions. Let $\varphi \in \mathbf{C}^{\mathbf{1}}_{\mathbf{c}}(\mathbb{R}^2)$ and multiply (2.10) by $\varphi(t^n, x_j)$. Summing over $j \in \mathbb{Z}$ and $n \in \mathbb{N}$ we get

$$\begin{aligned}
&\sum_n \sum_j \varphi(t^n, x_j)(U_j^{n+1} - U_j^n) \\
&\quad = -\frac{\Delta t}{2\Delta x} \sum_n \sum_j \varphi(t^n, x_j) \left(\mathbf{F}(U_{j+1}^n) - \mathbf{F}(U_{j-1}^n)\right) \\
&\qquad - \alpha \frac{\Delta t}{2\Delta x} \sum_n \sum_j \varphi(t^n, x_j) \left(2U_j^n - U_{j+1}^n - U_{j-1}^n\right).
\end{aligned}$$

Summing by parts we obtain

$$\begin{aligned}
&\sum_j \varphi(0, x_j) U_j^0 + \sum_n \sum_j \left(\varphi(t^n, x_j) - \varphi(t^{n-1}, x_j)\right) U_j^n \\
&\quad + \frac{\Delta t}{2\Delta x} \sum_n \sum_j \left(\varphi(t^n, x_{j+1}) - \varphi(t^n, x_{j-1})\right) \mathbf{F}(U_j^n) \\
&\quad + \alpha \frac{\Delta t}{2\Delta x} \sum_n \sum_j \left(\varphi(t^n, x_{j+1}) - 2\varphi(t^n, x_j) + \varphi(t^n, x_{j-1})\right) U_j^n = 0.
\end{aligned} \tag{2.15}$$

Then we multiply (2.15) by Δx getting

$$\begin{aligned}
&\Delta x \sum_j \varphi(0, x_j) U_j^0 + \Delta x \Delta t \sum_n \sum_j \frac{\varphi(t^n, x_j) - \varphi(t^{n-1}, x_j)}{\Delta t} U_j^n \\
&+ \Delta x \Delta t \sum_n \sum_j \frac{\varphi(t^n, x_{j+1}) - \varphi(t^n, x_{j-1})}{2\Delta x} \mathbf{F}(U_j^n) \\
&+ \alpha \frac{\Delta x \Delta t}{2} \sum_n \sum_j \left(\frac{\varphi(t^n, x_{j+1}) - \varphi(t^n, x_j)}{\Delta x} - \frac{\varphi(t^n, x_j) - \varphi(t^n, x_{j-1})}{\Delta x} \right) U_j^n = 0.
\end{aligned} \tag{2.16}$$

Passing to the limit in (2.16) for $\Delta x \to 0$ (in the nonlinear weak-$*$ sense of (2.14)) for U_j^n and using the regularity of φ, the last term vanishes and we get (2.13).

□

Frid and Liu [43] provide an explicit formula for computing the probability measure ν satisfying (2.14) in the case of Riemann-type initial data (2.4). For any space step Δx fixed, let $U_k = U_{\Delta x/k}$, $k \in \mathbb{N}$, be the sequence of approximate solutions obtained dividing Δx by k. Then, for any $h \in \mathbf{C}(\mathbb{R}^2; \mathbb{R})$ it holds

$$\langle \nu_{t,x}, h \rangle = \lim_{T \to \infty} \frac{2}{T^2} \int_0^T h(U_\Delta(\tau, (x/t)\tau))\tau \; d\tau \tag{2.17}$$

for almost every $x/t \in \mathbb{R}$. (For the proof, see [43, Appendix A.2].) For numerical purposes, we will use the following discretized version of formula (2.17) to compute the moments of interest:

$$\langle \nu_{t,x}, h \rangle = \lim_{N \to \infty} \frac{2}{N(N+1)} \sum_{k=1}^{N} k\, h(U_{j_k}^k), \quad j_k = \left[k \frac{\Delta t}{\Delta x} \frac{x}{t} \right], \tag{2.18}$$

where $[\cdot]$ denotes the integer part.

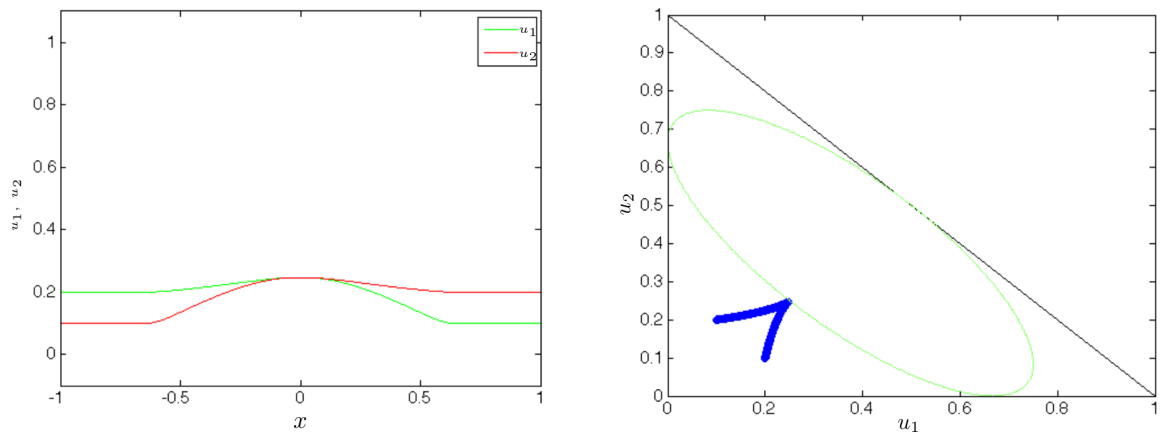

Figure 2.24: Solution of (2.1)-(2.4) with $U_L = (0.2, 0.1)$ and $U_R = (0.1, 0.2)$. We observe a classical configuration consisting of a 1-rarefaction and a 2-rarefaction separated by an intermediate state.

2.5 Numerical results

2.5.1 Distributional solutions

In this section, we present some numerical computations illustrating the principal features of weak (distributional) solutions of problem (2.1)-(2.4). From [53] we know that, if $U_L, U_R \in \Omega_u \setminus \bar{\mathcal{E}}$, then corresponding weak solutions must satisfy $U(x,t) \in \Omega_u \setminus \mathcal{E}$ a.e. In particular, U consists of a combination of rarefactions and shock waves, as illustrated by the following numerical tests, where we have taken $\Delta x = 0.001$, $\alpha = 1$, $CFL = 0.9$, and we display the approximate solution U_Δ at time $t = 1$, both in the x-u_1, u_2 plane (Figures 2.24-2.28 and 2.30-2.34, left) and in the phase plane u_1-u_2 (Figures 2.24-2.28 and 2.30-2.34, right).

Test 1. We consider initial data $U_L = (0.2, 0.1)$ and $U_R = (0.1, 0.2)$. The solution showed in Fig. 2.24 consists of a rarefaction of the first family joining U_L with an intermediate state close to $\partial\mathcal{E}$, followed by a rarefaction of the second family to U_R. This is a limit situation, since if the Lax curves do not intersect in the same connected region, the structure of the solution becomes more complex, as illustrated by the following examples.

Test 2. We consider initial data $U_L = (0.2, 0.1)$ and $U_R = (0.1, 0.3)$. The solution showed in Fig. 2.25 consists of a shock of the first family joining U_L with a state $U_1 = (u_{1,1}, 0)$ on the u_1-axis, followed by a crossing shock between U_1 and the state $(1, 0)$, a contact discontinuity form $(1, 0)$ to $(0, 1)$ with zero speed, another crossing shock from $(0, 1)$ to a point $U_2 = (0, u_{2,2})$ and a 2-shock from U_2 to U_R.

Test 3. We consider initial data $U_L = (0.2, 0.1)$ and $U_R = (0.1, 0.8)$. The solution showed in Fig. 2.26 consists of a shock of the first family joining U_L with a state $U_1 = (u_{1,1}, 0)$ on the u_1-axis, followed by a crossing shock between U_1 and the state $(1, 0)$, a standing contact discontinuity form $(1, 0)$ to a point $U_2 = (u_{1,2}, 1 - u_{1,2}) \in \partial\Omega_u$ and a 2-shock from U_2 to U_R.

Test 4. We consider initial data $U_L = (0.2, 0.1)$ and $U_R = (0.85, 0.1)$. The solution showed in Fig. 2.27 consists of a shock of the first family joining U_L with a state $U_1 = (u_{1,1}, 0)$ on the u_1-axis, followed by a crossing shock between U_1 and a state $U_2 = (u_{1,2}, 0)$ and a 2-shock

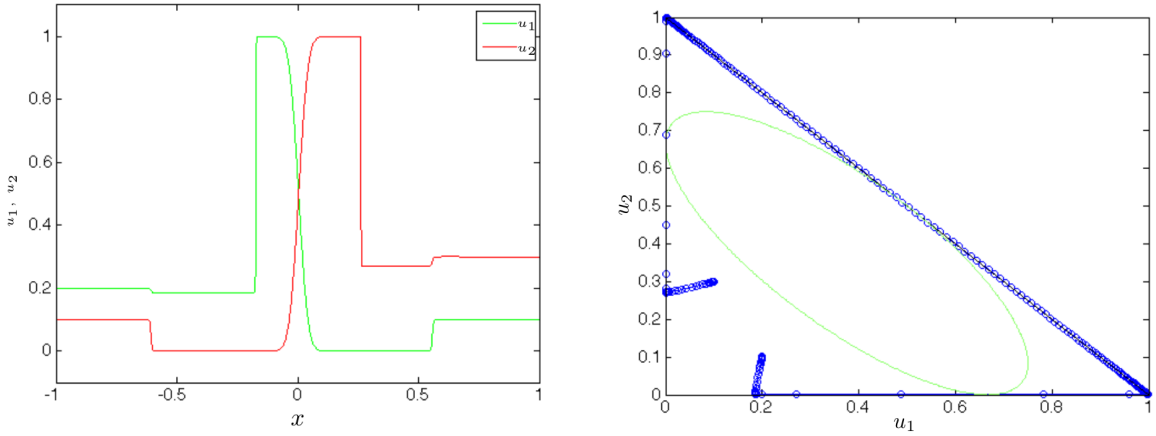

Figure 2.25: Solution of (2.1)-(2.4) with $U_L = (0.2, 0.1)$ and $U_R = (0.1, 0.3)$. We observe a 1-shock, a crossing shock, a contact discontinuity, another crossing shock and a 2-shock.

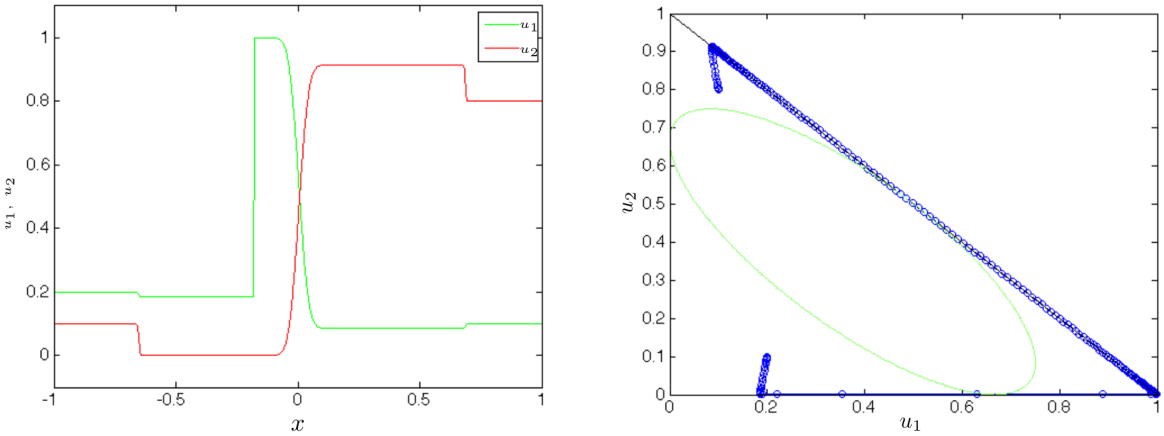

Figure 2.26: Solution of (2.1)-(2.4) with $U_L = (0.2, 0.1)$ and $U_R = (0.1, 0.8)$. We observe a 1-shock, a crossing shock, a contact discontinuity and a 2-shock.

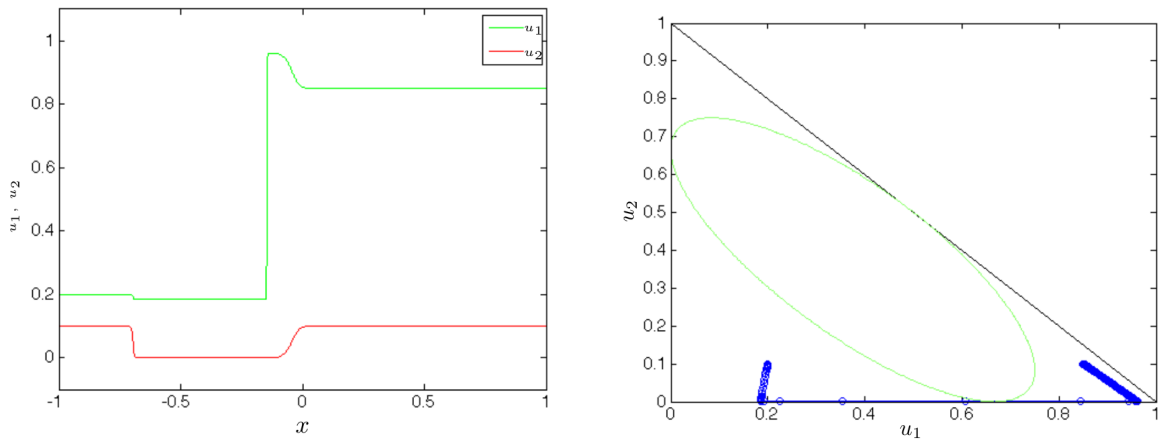

Figure 2.27: Solution of (2.1)-(2.4) with $U_L = (0.2, 0.1)$ and $U_R = (0.85, 0.1)$. We observe a 1-shock, a crossing shock and a 2-shock.

from U_2 to U_R. We remark that the crossing shock is sharply captured.

Test 5. We consider initial data $U_L = (0.2, 0.1)$ and $U_R = (0.75, 0.1)$. The solution showed in Fig. 2.28 consists of a shock of the first family joining U_L with a state U_1 in the interior of the domain, followed by a crossing shock between U_1 and a state U_2 superposed to a 2-shock from U_2 to U_R. Note that this composite wave could be replaced by a 2-shock joining directly U_1 to U_R, see [58]. Indeed, we have

$$U_2 \in \mathcal{H}(U_1), \quad U_R \in \mathcal{H}(U_2), \quad U_R \in \mathcal{H}(U_1),$$

and

$$s(U_1, U_2) = s(U_2, U_R) = s(U_1, U_R).$$

Anyway, the two solutions are identical as $\mathbf{L_1}$ functions.

Remark The configurations displayed in Tests 2-3 are unrealistic from the modeling point of view, because they result in a complete blocking of one or both groups of pedestrians, represented by the vacuum regions delimited by the standing contact discontinuities. In reality, such stuck situations never occur in normal conditions, and the flows always organize so that few people manage to pass, even if the resulting capacity can be very reduced [22]. System (2.1) must be seen as a toy model, whose understanding can give some insight for more realistic approaches.

If one or both values of the Riemann initial data $U^0 = (U_L, U_R)$ belong to $\mathcal{E}$, we can still observe distributional solutions in some cases. In accordance to [53], since $\mathcal{E}$ is convex, if $U_L \in \mathcal{E}$ or $U_R \in \mathcal{E}$ and u_1 is a weak solutions, then if $U(t, x) \in \mathcal{E}$ for some t, x, than $u_1(t, x) \in \{U_L, U_R\}$. Indeed, the initial state belonging to $\mathcal{E}$ will be connected through a shock to some $U_M \in \Omega_u \setminus \mathcal{E}$. In particular, given any point $U_L \in \mathcal{E}$, $\mathcal{H}(U_L) \cap \mathcal{E} = \{U_L\}$, see Fig. 2.29.

Examples of weak (distributional) solutions are given in Figures 2.30-2.32. In these cases, the Hugoniot loci of the states belonging to $\mathcal{E}$ intersect the Lax curves of the following state, and no oscillations appear in the numerical approximation.

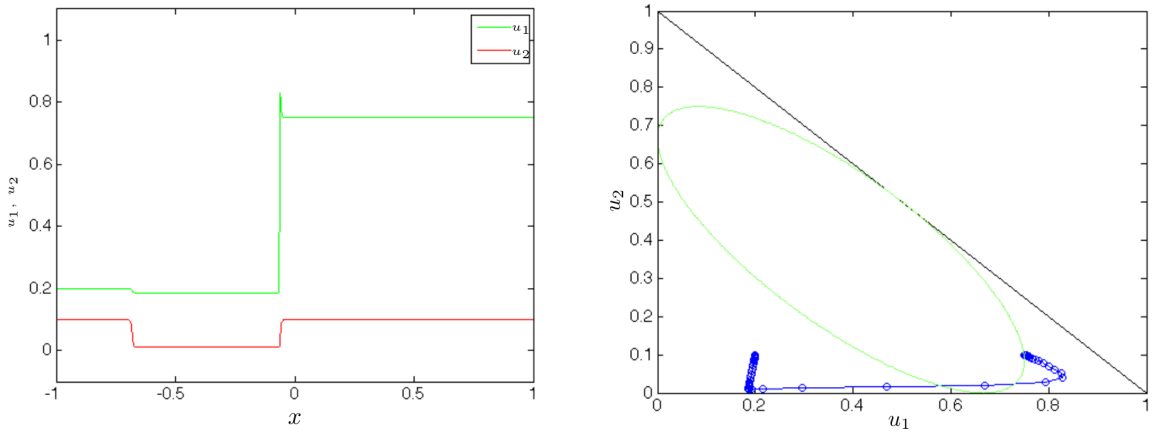

Figure 2.28: Solution of (2.1)-(2.4) with $U_L = (0.2, 0.1)$ and $U_R = (0.75, 0.1)$. We observe a 1-shock, a crossing shock and a 2-shock.

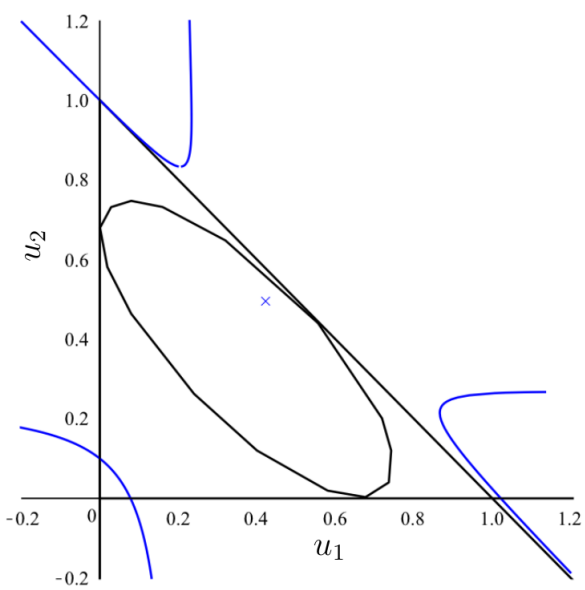

Figure 2.29: The Hugoniot locus $\mathcal{H}(U_L)$ for $U_L = (0.4, 0.5) \in \mathcal{E}$. Remark that $\mathcal{H}(U_L) \cap \mathcal{E} = U_L$.

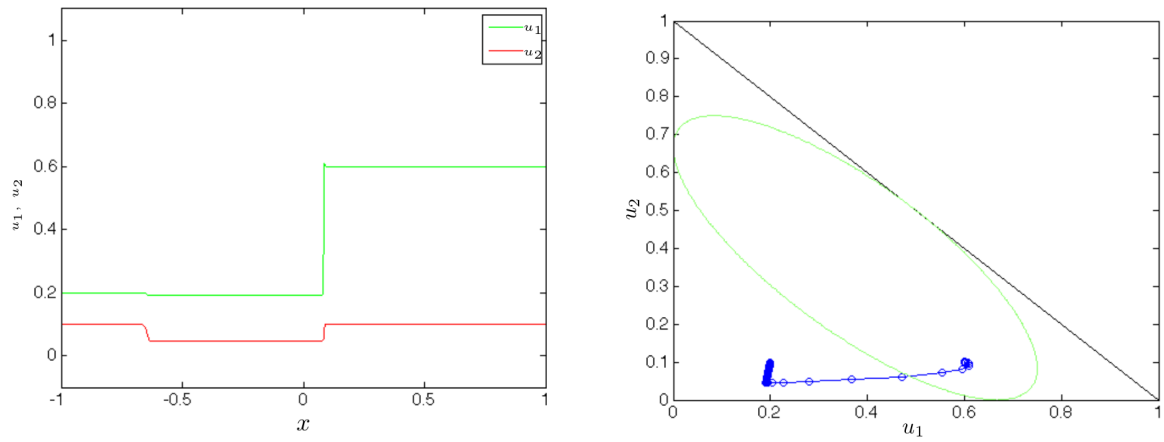

Figure 2.30: Distributional solution of (2.1)-(2.4) with $U_L = (0.2, 0.1)$ and $U_R = (0.6, 0.1) \in \mathcal{E}$. We observe a 1-shock in the hyperbolic region, followed by a shock connecting the state U_R in the elliptic region.

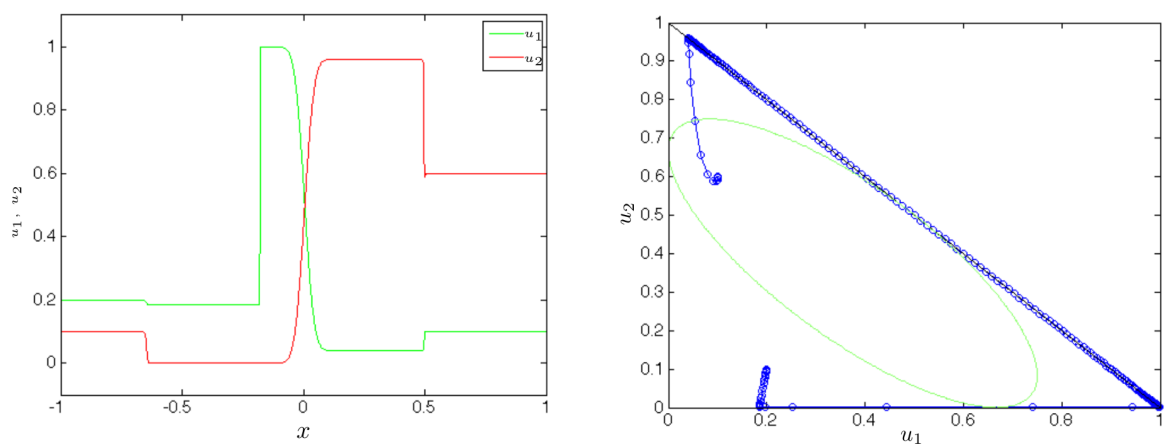

Figure 2.31: Distributional solution of (2.1)-(2.4) with $U_L = (0.2, 0.1)$ and $U_R = (0.1, 0.6) \in \mathcal{E}$. We observe a 1-shock, a crossing shock and a contact discontinuity in the hyperbolic region, followed by a shock joining directly U_R.

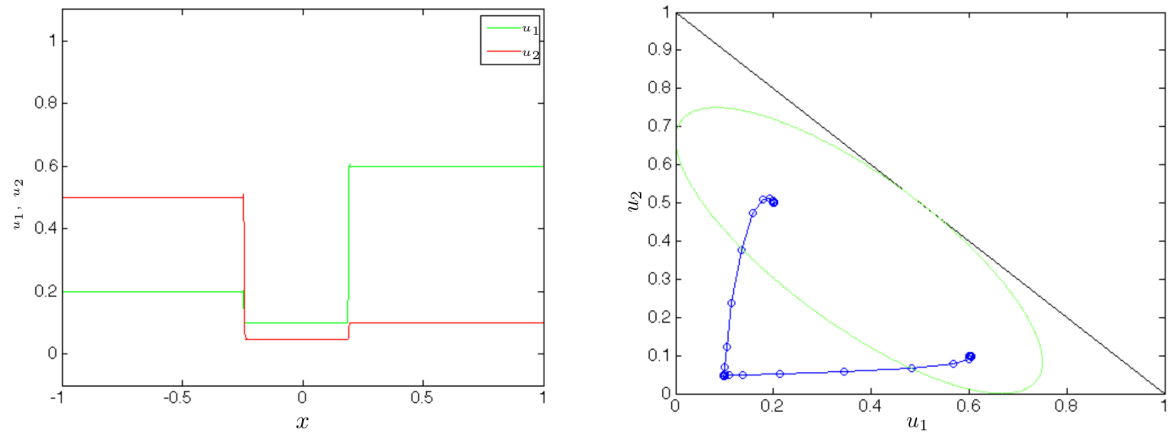

Figure 2.32: Distributional solution of (2.1)-(2.4) with initial data in the elliptic region: $U_L = (0.2, 0.5) \in \mathcal{E}$ and $U_R = (0.6, 0.1) \in \mathcal{E}$. We observe two shocks joining U_L and U_R with an intermediate state in the hyperbolic region.

2.5.2 Measure-valued solutions

In general, if the Riemann initial data take values in the elliptic region $\mathcal{E}$, the approximate solutions computed through the numerical scheme (2.10)-(2.11) display persistent oscillations. As examples, in this section we analyze the behavior of the approximate solutions corresponding to the initial data $U_L = (0.1, 0.2)$, $U_R = (0.4, 0.5)$ and $U_L = (0.4, 0.5)$, $U_R = (0.1, 0.2)$. Figures 2.33, 2.34 show the corresponding approximate solutions for $\Delta x = 0.001$ and $\Delta x = 0.0002$ at time $t = 1$. It appears that oscillations joining the state in $\mathcal{E}$ with the hyperbolic region increase in number as the mesh size decreases.
To get further information on the measure-valued solutions corresponding to the above initial data, we compute their average (or expected values) and variance relying on formula (2.18). In particular, we get

$$\overline{U}(t,x) := \int_{\mathbb{R}^2} \lambda \, \mathrm{d}\nu_{t,x}(\lambda) = \lim_{N\to\infty} \frac{2}{N(N+1)} \sum_{k=1}^{N} k \, U_{j_k}^k \tag{2.19}$$

for the mean densities,

$$\overline{\mathbf{F}(U)}(t,x) := \int_{\mathbb{R}^2} \mathbf{F}(\lambda) \, \mathrm{d}\nu_{t,x}(\lambda) = \lim_{N\to\infty} \frac{2}{N(N+1)} \sum_{k=1}^{N} k \, \mathbf{F}(U_{j_k}^k) \tag{2.20}$$

for the mean fluxes, and

$$\begin{aligned} \mathrm{Var}(U)(t,x) &:= \int_{\mathbb{R}^2} (\lambda - \overline{U}(t,x))^2 \, \mathrm{d}\nu_{t,x}(\lambda) \\ &= \lim_{N\to\infty} \frac{2}{N(N+1)} \sum_{k=1}^{N} k \, (U_{j_k}^k - \overline{U}(t,x))^2, \\ &= \lim_{N\to\infty} \frac{2}{N(N+1)} \sum_{k=1}^{N} k \, (U_{j_k}^k)^2 - \overline{U}(t,x)^2 \end{aligned} \tag{2.21}$$

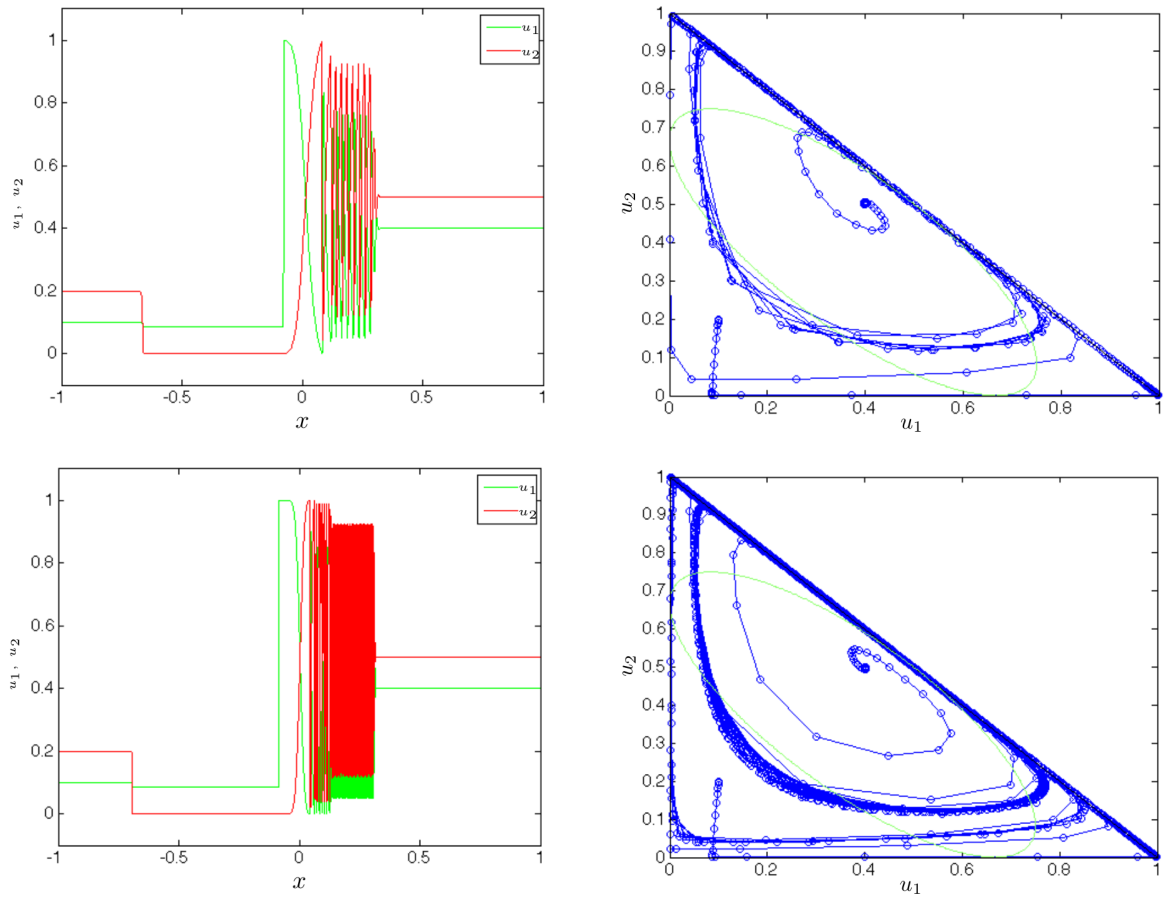

Figure 2.33: Solution of (2.1)-(2.4) with initial data $U_L = (0.1, 0.2)$ and $U_R = (0.4, 0.5) \in \mathcal{E}$ for $\Delta x = 0.001$ (top) and $\Delta x = 0.0002$ (bottom).

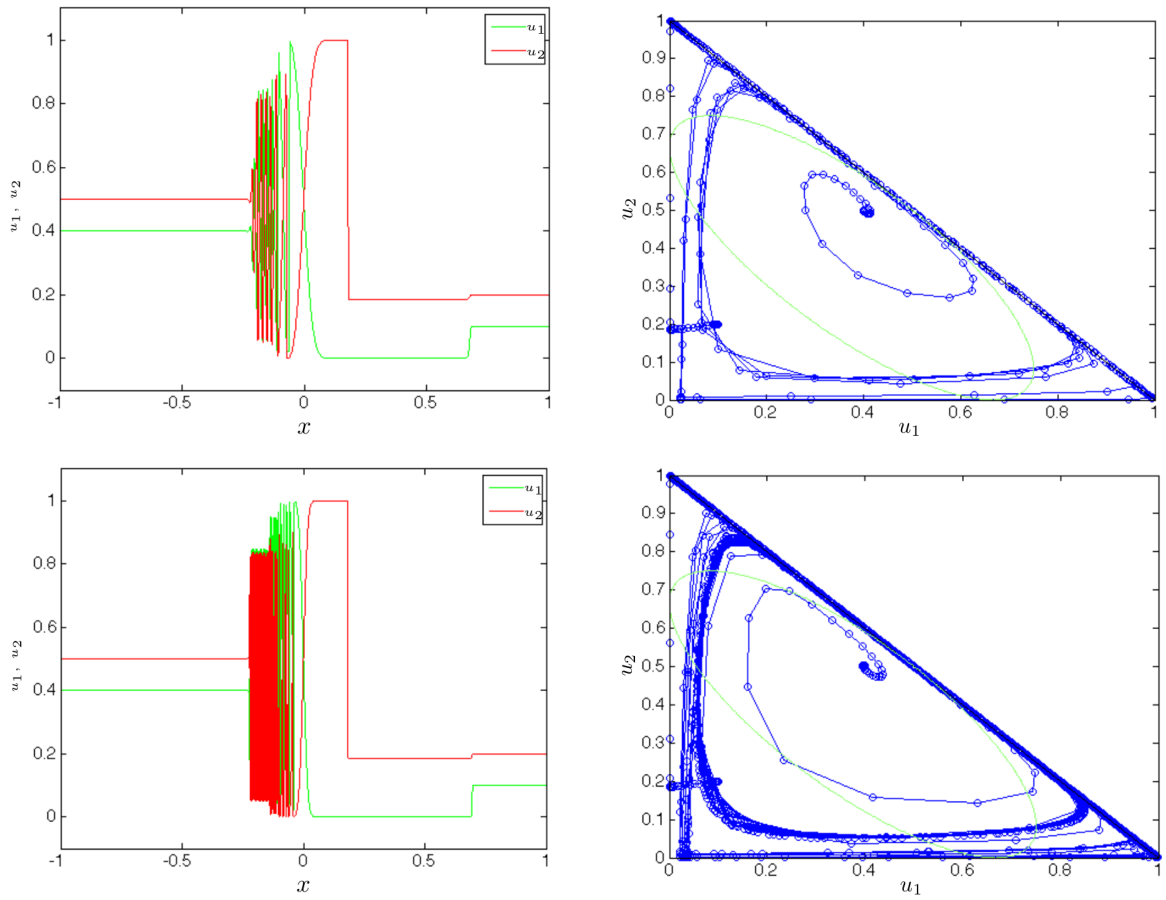

Figure 2.34: Solution of (2.1)-(2.4) with initial data $U_L = (0.4, 0.5) \in \mathcal{E}$ and $U_R = (0.1, 0.2)$ for $\Delta x = 0.001$ (top) and $\Delta x = 0.0002$ (bottom).

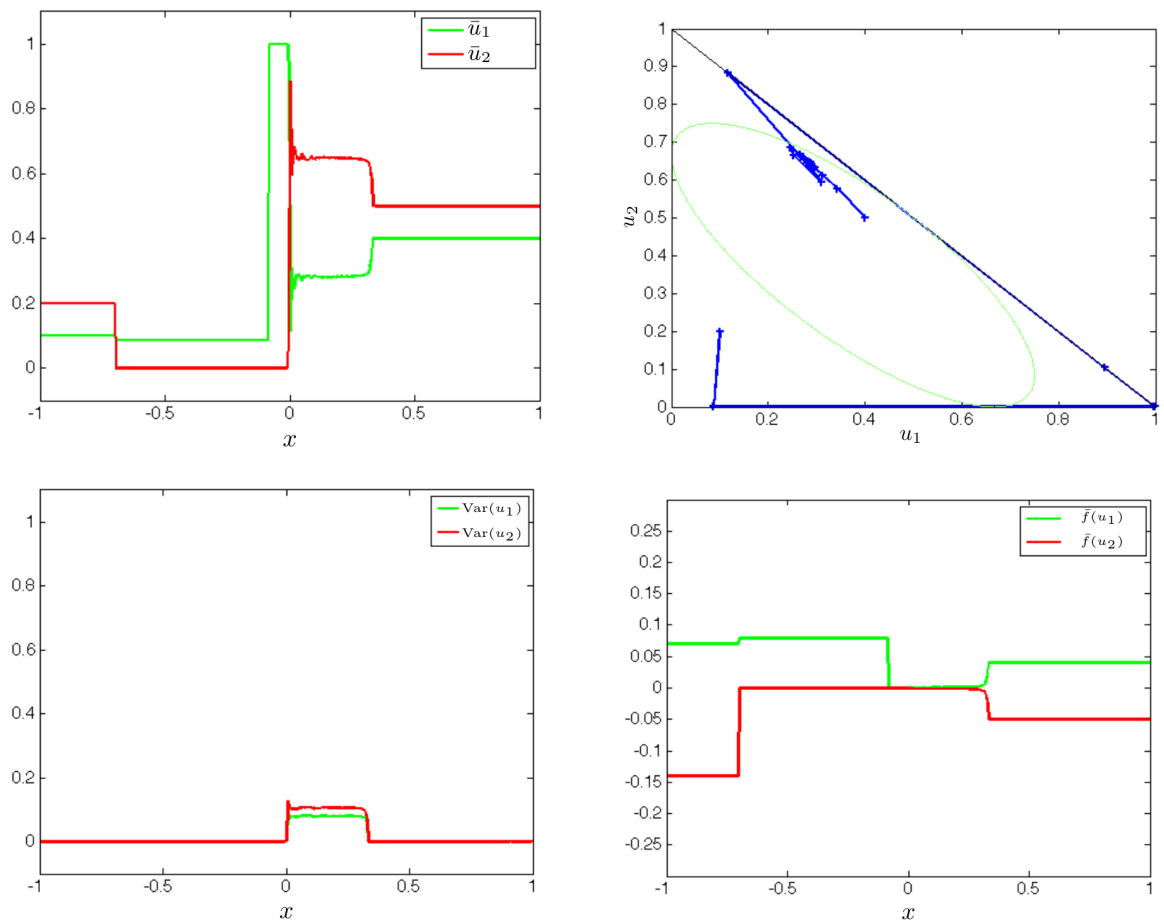

Figure 2.35: Average (top for density values (2.19) and bottom right for flux (2.20)) and variance (2.21) (bottom left) corresponding to initial data $U_L = (0.1, 0.2)$ and $U_R = (0.4, 0.5)$ and $N = 4 \cdot 10^6$ iterations.

for the density variance. As expected, the average coincides with the densities and the variance is zero for values in the hyperbolic region, see Figures 2.35, 2.36.

Remark that the convergence of the limit in (2.18) is very slow. We have performed simulations using a $CFL = 0.1$, and taking $\Delta x = 4 \cdot 10^{-5},\ 2 \cdot 10^{-5},\ 1 \cdot 10^{-5},\ 5 \cdot 10^{-6},\ 2.5 \cdot 10^{-6}$, which correspond to $N = 2.5 \cdot 10^5,\ 5 \cdot 10^5,\ 1 \cdot 10^6,\ 2 \cdot 10^6,\ 4 \cdot 10^6$ iterations. Fig 2.35, 2.36 show the average and the variance computed for $\Delta x = 5 \cdot 10^{-6}$, that is $N = 2 \cdot 10^6$. Note that we still observe oscillations for values in the elliptic region.

Aiming at giving an estimation of the accuracy of the results, we also compute the conservation errors and the convergence rates, which are given in Tables 2.1, 2.2. The conservation error

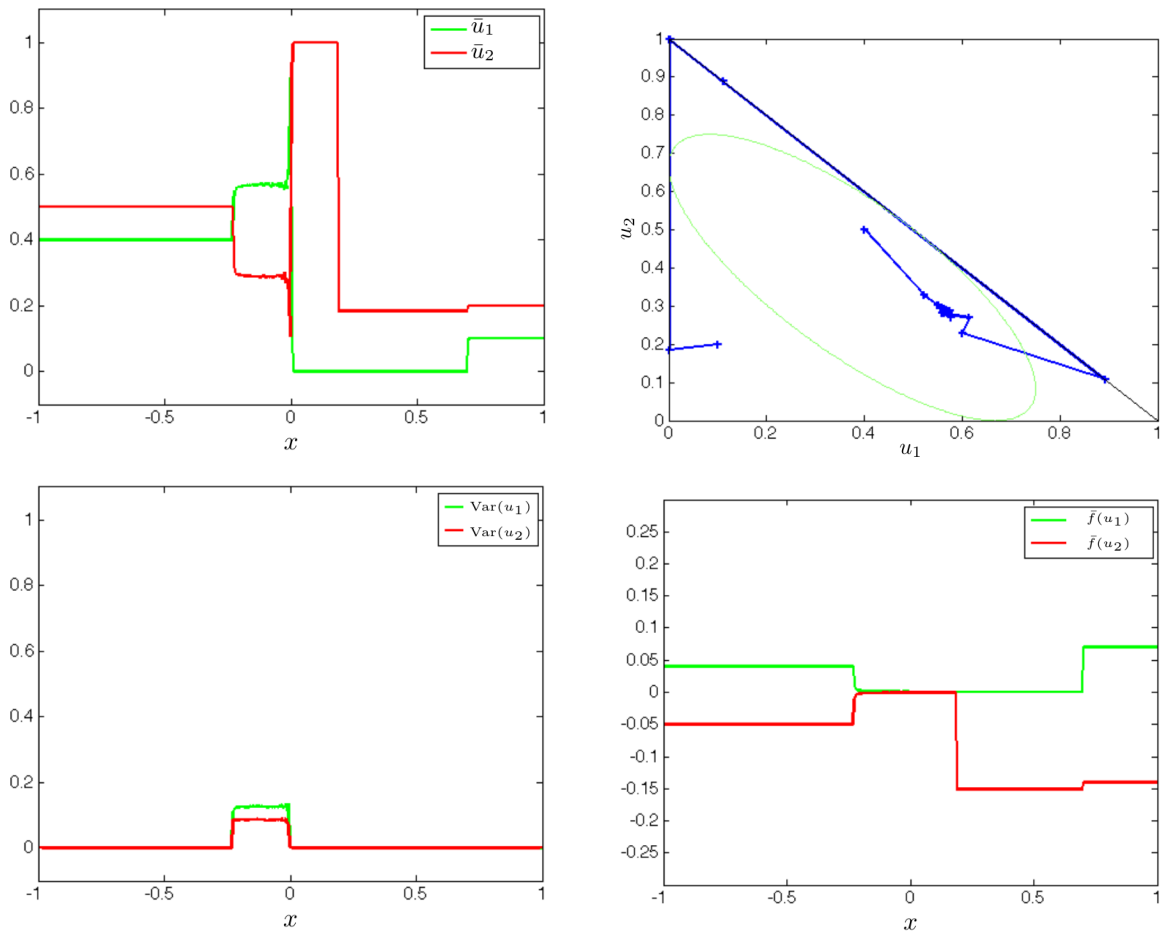

Figure 2.36: Average (top for density values (2.19) and bottom right for flux (2.20)) and variance (2.21) (bottom left) corresponding to initial data $U_L = (0.4, 0.5)$ and $U_R = (0.1, 0.2)$ and $N = 4 \cdot 10^6$ iterations.

	$U_L = (0.1, 0.2)$ $U_R = (0.4, 0.5)$		$U_L = (0.4, 0.5)$ $U_R = (0.1, 0.2)$	
N	E^1_{cons}	E^2_{cons}	E^1_{cons}	E^2_{cons}
2.5e05	-1.627e-03	2.869e-04	-5.537e-04	-1.443e-05
5e05	-1.256e-03	-5.011e-04	-2.257e-04	6.580e-04
1e06	-9.259e-04	-7.722e-04	1.054e-03	-4.071e-06
2e06	-1.532e-03	-7.331e-05	-4.071e-04	6.019e-04
4e06	-1.514e-03	-1.714e-04	3.873e-04	2.489e-05

Table 2.1: Conservation errors (2.22) at time $t = 1$.

	$U_L = (0.1, 0.2)$ $U_R = (0.4, 0.5)$		$U_L = (0.4, 0.5)$ $U_R = (0.1, 0.2)$	
N	γ^1	γ^2	γ^1	γ^2
2.5e05	0.37413	0.46423	0.61146	0.65385
5e05	0.62555	0.49616	0.26923	0.37293
1e06	0.52973	0.63003	1.04921	0.91148

Table 2.2: Convergence rates (2.23) at time $t = 1$.

is given by the formula

$$\begin{aligned} E^U_{cons}(N,t) &= \begin{pmatrix} E^1_{cons}(t) \\ E^2_{cons}(t) \end{pmatrix} \\ &= \int_{-1}^{1} \overline{U}^N(t,x)\,\mathrm{d}x - \int_{-1}^{1} U^0(x)\,\mathrm{d}x \\ &+ \int_0^t \overline{\mathbf{F}(U)}^N(s,1)\,ds - \int_0^t \overline{\mathbf{F}(U)}^N(s,-1)\,ds, \end{aligned} \tag{2.22}$$

where

$$\overline{U}^N(t,x) := \frac{2}{N(N+1)} \sum_{k=1}^{N} k\, U^k_{j_k}$$

and

$$\overline{\mathbf{F}(U)}^N(t,x) := \frac{2}{N(N+1)} \sum_{k=1}^{N} k\, \mathbf{F}(U^k_{j_k}).$$

The $\mathbf{L_1}$-convergence rate is defined by

$$\gamma(N) = \begin{pmatrix} \gamma^1(N) \\ \gamma^2(N) \end{pmatrix} = \begin{pmatrix} \log_2\left(e^1(N)/e^1(2N)\right) \\ \log_2\left(e^2(N)/e^2(2N)\right) \end{pmatrix}, \tag{2.23}$$

where the $\mathbf{L_1}$-error is computed at final time $t = 1$ as

$$e(N) = \begin{pmatrix} e^1(N) \\ e^2(N) \end{pmatrix} = \|\overline{U}^N(t,\cdot) - \overline{U}^{2N}(t,\cdot)\|_{\mathbf{L_1}([-1,1])}.$$

(In the above expressions, the integrals are intended component by component.)
We observe that conservation errors remain quite stable, while the $\mathbf{L_1}$-convergence rate is low. Indeed, the very long computing times prevented us to reach sharper approximations.

2.6 Conclusion

The 2×2 system (2.1) is a simplified model for the motion of two groups of people walking in opposite directions along a corridor. This situation is known for displaying characteristic patterns as lane formation [51, 69]. The system consists of two conservation laws of mixed hyperbolic-elliptic type. Though the solution configurations are not always realistic, the instabilities observed for densities in the elliptic region could be related to these auto-organization phenomena that result in a transition from a mixture to separate phases.
We investigated the model properties and pull out nonclassical elements in mixed-type system. Then we conjectured an admissible solution to the Riemann problem initial for data in hyperbolic regions, but the unicity of the solution is still an open question.
We presented a Lax-Friedrichs finite volume scheme, and proved an $\mathbf{L}_\infty$ bound of the approximate solutions to ensure the convergence towards Young measures.
Following [43], we compute the average of sequence of solutions with persisting oscillations and get the expected values and the variance for densities and fluxes. The recovery of the flux characteristics through this method advocates the recast of the corresponding Cauchy problem in the framework of measure-valued solutions.

Chapter 3

Finite volume approximation of a nonlocal model of pedestrian traffic applied to the initial data optimization of an evacuation problem.

Contents

3.1 Introduction **68**
3.2 Approximation of the solutions with a finite volume scheme . . . **68**
3.2.1 The algorithm 68
3.2.2 Existence of solutions 70
3.2.3 Numerical convergence of the numerical scheme 74
3.3 Optimization of the initial data for an evacuation problem **75**
3.3.1 Settings 75
3.3.2 Formulation of the optimization problem 78
3.3.3 Discrete formulation 78
3.3.4 Formulation of the cost function gradient 78
3.3.5 Numerical validation of the gradient 80
3.3.6 Optimization results 82
3.4 Conclusion **88**

3.1 Introduction

We consider the following system of N continuity equations on $\Omega \subset \mathbb{R}^2$

$$\partial_t U + \mathrm{div}_{x,y} F(t, x, y, U, \eta * U) = 0 \tag{3.1}$$

The flow F depends nonlocally on the distribution of density with $t \in \mathbb{R}^+$, $(x, y) \in \mathbb{R}^2$, $U \in \mathbb{R}^N$, $\eta : \mathbb{R}^2 \mapsto \mathbb{R}^{m\times N}$ and the coupling is due to the nonlocal terms $\eta * U$ given for $\ell = 1, ..., m$, by

$$(\eta * U)_\ell(t, x, y) = \int_{\mathbb{R}^2} \sum_{k=1}^{N} \eta^{\ell,k}(x - x', y - y')U^k(t, x', y')\mathrm{d}x'\mathrm{d}y'.$$

This kind of conservation laws is used to represent various physical phenomena, for instance in biology [24, 38, 44, 48], conveyor belts [7, 8, 47], sedimentation [4, 16] and finally crowd dynamics. Nonlocal models of pedestrian traffic are remarkable for spontaneous lane formation in crowd, but also for failing at several properties of usual macroscopic models. [28] addressed the loss of maximum principle and the fact that nonlocality allows information to virtually travel at infinite speed. The well-posedness of the Cauchy problem has been stated in [26, 28, 29] with an extensive study of the continuous dependence of the solution on the initial datum and its stability with respect to the vector field in [29].
We address the numerical integration of this model via a Lax-Friedrichs algorithm that converges, up to a subsequence, to a weak entropy solution of (3.1). The scheme considered here is a variant of the one proposed by Colombo et al. in [1]. In particular, it takes cell centered evaluations of local and nonlocal data. Then we consider an adjoint state based gradient descent method to solve the optimization problem of an evacuation, where the evacuation total time is minimized by reshaping the initial density distribution. In the Appendix D, we detail the computations and the description of the vector field generation, and explore the effect of nonisotropic kernels. Theorem 3.2.1 ensures the existence of a weak entropic solution to (3.1) with a general flow. The positivity, the mass conservation and the bounding of the density advocate this solution to be physical. Finally the Lipschitz continuity in time guarantees the existence of a solution and the bounds above on any finite time interval and establishes the finite speed of propagation of the information at the functional level.

3.2 Approximation of the solutions with a finite volume scheme

3.2.1 The algorithm

We fix our attention to the k-th equation in (3.1) for $k = 1, \ldots, N$,

$$\partial_t U^k + \partial_x f^k(t, x, y, U^k, \eta * U) + \partial_y g^k(t, x, y, U^k, \theta * U) = 0 \tag{3.2}$$

with f and g as fluxes and where the nonlocal terms $(\eta * U)$ and $(\theta * U)$ are given by the usual convolution product.
Throughout, we denote the Euclidean norm with the notation $|\xi|$ for $\xi \in \mathbb{R}$, $\|\xi\|$ for $\xi \in \mathbb{R}^w$, w being an integer strictly greater than 1 and the functional norm $\|\zeta\|_{\mathbf{L}_\infty(\mathbb{R}^2;\mathbb{R}^N)} = \sup_{(x,y)\in\mathbb{R}^2} \|\zeta(x, y)\|$ for every $\zeta \in \mathbb{R}^N$.
The following assumptions on the maps $f^k = f^k(t, x, y, U^k, A)$ and $g^k = g^k(t, x, y, U^k, B)$ and η, θ in (3.2), for $k = 1, \ldots, N$, are used below

(H0) $f^k,\ g^k \in \mathbf{C^2}(\mathbb{R}^+ \times \mathbb{R}^2 \times \mathbb{R} \times \mathbb{R}^m; \mathbb{R})$; $\partial_u f^k,\ \partial_u g^k \in \mathbf{L}_\infty(\mathbb{R}^+ \times \mathbb{R}^2 \times \mathbb{R} \times \mathbb{R}^m; \mathbb{R})$; for all $t \in \mathbb{R}^+$, $(x, y) \in \mathbb{R}^2$ and $A, B \in \mathbb{R}^m$, $f^k(t, x, y, 0, A) = g^k(t, x, y, 0, B) = 0$.

(H1) There exists $M > 0$ such that for all t, x, y, u, A, B in their respective domains,

$$|\partial_x f^k|, |\partial^2_{xx} f^k|, |\partial^2_{xy} f^k|, \|\nabla_A f^k\|, \|\partial_x \nabla_A f^k\|, \|\partial_y \nabla_A f^k\|, \|\nabla^2_{AA} f^k\| \le M|u|,$$
$$|\partial_y g^k|, |\partial^2_{yy} g^k|, |\partial^2_{xy} g^k|, \|\nabla_B g^k\|, \|\partial_x \nabla_B g^k\|, \|\partial_y \nabla_B g^k\|, \|\nabla^2_{BB} g^k\| \le M|u|.$$

(H2) $\partial_u f^k,\ \partial_u g^k \in \mathbf{W^{1,\infty}}(\mathbb{R}^+ \times \mathbb{R}^2 \times \mathbb{R} \times \mathbb{R}^m; \mathbb{R})$.

(H3) $\eta,\ \theta \in (\mathbf{C^2} \cap \mathbf{W^{2,\infty}})(\mathbb{R}^2; \mathbb{R}^{m\times N})$.

(H0) settles f and g as *flux*, smooth and null for a zero density. The constant M in (H1) relates the flux variations to the density. Thanks to (H2), $\partial_u f$ and $\partial_u g$ are Lipschitz and with (H3) η and θ are sufficiently smooth.

Definition 3.2.1 *Let $U^0 \in \mathbf{L}_\infty(\mathbb{R}^2; \mathbb{R}^N)$. A map $U : [0, T] \mapsto \mathbf{L}_\infty(\mathbb{R}^2; \mathbb{R}^N)$ is a solution to* (3.1) *with initial datum U^0 if for $k = 1, \dots, N$, setting for all $w \in \mathbb{R}$*

$$\tilde{f}^k(t, x, y, w) = f^k(t, x, y, w, (\eta * U)(t, x, y)),$$
$$\tilde{g}^k(t, x, y, w) = g^k(t, x, y, w, (\theta * U)(t, x, y)),$$

the map U^k is a Kružkov solution to the conservation law

$$\begin{cases} \partial_t U^k + \partial_x \tilde{f}^k(t, x, y, U^k) + \partial_y \tilde{g}^k(t, x, y, U^k) = 0, \\ U^k(0, x, y) = U^{0,k}(x, y). \end{cases} \tag{3.3}$$

Fix a rectangular grid with sizes Δx and Δy in $\mathbb{R}^2$ and choose a time step Δt. For later use, we also introduce the usual notation

$$t^n = n\Delta t,\ n \in \mathbb{N}$$

$$\begin{aligned} x_i &= i\Delta x, \quad x_{i+\frac{1}{2}} = \left(i + \tfrac{1}{2}\right)\Delta x, \quad i \in \mathbb{Z}; \quad \lambda_x = \Delta t/\Delta x, \\ y_j &= j\Delta y, \quad y_{j+\frac{1}{2}} = \left(j + \tfrac{1}{2}\right)\Delta y, \quad j \in \mathbb{Z}; \quad \lambda_y = \Delta t/\Delta y. \end{aligned} \tag{3.4}$$

We define a piecewise constant approximation solution $u_\Delta \equiv (u^1_\Delta, ..., u^N_\Delta)$ to (3.2) by

$$u^k_\Delta(t, x, y) = u^{k,n}_{ij} \quad \text{for} \quad \begin{cases} t \in [t^n, t^{n+1}[, \\ x \in [x_{i-1/2}, x_{i+1/2}[, \\ y \in [y_{j-1/2}, y_{i+1/2}[, \end{cases}$$

through the nonlocal algorithm based on dimensional splitting, see [31]

$$\begin{aligned} u^{k,n+1/2}_{ij} =& u^{k,n}_{ij} - \frac{\lambda_x}{2}\left[F^{k,n}_{i+1/2,j}(u^{k,n}_{ij}, u^{k,n}_{i+1,j}) - F^{k,n}_{i-1/2,j}(u^{k,n}_{i-1,j}, u^{k,n}_{ij})\right] \\ u^{k,n+1}_{ij} =& u^{k,n+1/2}_{ij} - \frac{\lambda_y}{2}\left[G^{k,n+1/2}_{i,j+1/2}(u^{k,n+1/2}_{ij}, u^{k,n+1/2}_{i,j+1})\right. \\ & \left. - G^{k,n+1/2}_{i,j-1/2}(u^{k,n+1/2}_{i,j-1}, u^{k,n+1/2}_{ij})\right] \end{aligned} \tag{3.5}$$

with

$$
\begin{aligned}
F^{k,n}_{i+1/2,j}(a,b) &= \frac{f^{k,n}_{ij}(a) + f^{k,n}_{i+1,j}(b)}{2} - \frac{\alpha(b-a)}{2\lambda_x},\\
G^{k,n+1/2}_{i,j+1/2}(a,b) &= \frac{g^{k,n+1/2}_{ij}(a) + g^{k,n+1/2}_{i,j+1}(b)}{2} - \frac{\beta(b-a)}{2\lambda_y},\\
f^{k,n}_{ij}(a) &= f^k(t^n, x_i, y_j, a, A^n_{ij}),\\
g^{k,n+1/2}_{ij}(b) &= g^k(t^{n+1/2}, x_i, y_j, b, B^{n+1/2}_{ij}).
\end{aligned}
$$

The convolution terms are computed through quadrature formulæ, i.e.,

$$
\begin{aligned}
A^n_{ij} &= \Delta x \Delta y \left[\sum_{l,p\in\mathbb{Z}} \sum_{k=1}^{N} \eta^{1,k}_{i-l,j-p} u^{k,n}_{l,p}, \dots, \sum_{l,p\in\mathbb{Z}} \sum_{k=1}^{N} \eta^{m,k}_{i-l,j-p} u^{k,n}_{l,p} \right], \qquad (3.6)\\
B^{n+1/2}_{ij} &= \Delta x \Delta y \left[\sum_{l,p\in\mathbb{Z}} \sum_{k=1}^{N} \theta^{1,k}_{i-l,j-p} u^{k,n+1/2}_{l,p}, \dots, \sum_{l,p\in\mathbb{Z}} \sum_{k=1}^{N} \theta^{m,k}_{i-l,j-p} u^{k,n+1/2}_{l,p} \right],
\end{aligned}
$$

where $\eta^{l,k}_{ij} = \eta^{l,k}(x_i, y_j)$ and $\theta^{l,k}_{ij} = \theta^{l,k}(x_i, y_j)$.
Throughout, we require that Δt is chosen in order to satisfy the CFL condition

$$
\lambda_x \le \frac{\min\{3\alpha, 2-3\alpha, 1\}}{1+3\max_k \|\partial_u f^k\|_{\mathbf{L}_\infty}}, \quad \lambda_y \le \frac{\min\{3\beta, 2-3\beta, 1\}}{1+3\max_k \|\partial_u g^k\|_{\mathbf{L}_\infty}}, \qquad (3.7)
$$

and we assume that the mesh sizes are sufficiently small, in the sense that Δx, $\Delta y \le 1/(3M)$, where M is as in (H1).

3.2.2 Existence of solutions

In this part, we present existence results for the problem (3.2) discretized with the numerical scheme (3.5).

Theorem 3.2.1 . *Let* (H0), (H1), (H3) *and* (3.7) *hold. Fix an initial datum* $U^0 \in (\mathbf{L_1} \cap \mathbf{L}_\infty \cap \mathbf{BV})(\mathbb{R}^2; \mathbb{R}^N_+)$. *Then the algorithm* (3.5) *defines a sequence of approximate solutions which converges, up to a subsequence, to a solution* $U \in \mathbf{C^0}(\mathbb{R}^+; \mathbf{L_1}(\mathbb{R}^2; \mathbb{R}^N_+))$ *to* (3.2) *in the sense of Definition 3.2.1. Moreover,* U *is locally Lipschitz continuous with respect to the* $\mathbf{L_1}$ *norm and for all* $k \in \{1, \dots, N\}$ *and for all* $t \in \mathbb{R}^+$, *the following bounds hold:*

$$
\begin{aligned}
&\|U(t)\|_{\mathbf{L}_\infty(\mathbb{R}^2;\mathbb{R}^N)} \le e^{\mathcal{C}t(1+\|U^0\|_{\mathbf{L_1}})} \|U^0\|_{\mathbf{L}_\infty(\mathbb{R}^2;\mathbb{R}^N)} && \textit{with } \mathcal{C} \textit{ as in } (\text{A.5}),\\
&\|U^k(t)\|_{\mathbf{L_1}(\mathbb{R}^2;\mathbb{R})} = \|U^{0,k}\|_{\mathbf{L_1}(\mathbb{R}^2;\mathbb{R})},\\
&\boldsymbol{TV}(U^k(t)) \le e^{\mathcal{K}_1 t} \boldsymbol{TV}(U^k_0) + \frac{\mathcal{K}_2}{\mathcal{K}_1}\left(e^{\mathcal{K}_1 t} - 1\right) && \textit{with } \mathcal{K}_1,\ \mathcal{K}_2 \textit{ as in } (\text{A.9}),\\
&\|U(t+\tau) - U(t)\|_{\mathbf{L}_\infty(\mathbb{R}^2;\mathbb{R}^N)} \le C(t)\tau && \textit{with } C(t) \textit{ as in } (\text{A.11}),
\end{aligned}
$$

We split the proof of Theorem 3.2.1 in several steps, each with its own significance and proved in a specific lemma. All proofs are deferred to Appendix A.
The positivity ensures that the numerical solution takes physical values, while simplifying the forthcoming computations.

Lemma 3.2.2 *(Positivity). Let* (H0), (H1), (H3) *and* (3.7) *hold. Fix a* $U^0 \in \mathbf{L_1} \cap \mathbf{L}_\infty)(\mathbb{R}^2; \mathbb{R}^N_+)$. *Then the approximate solution* u_Δ *defined by the algorithm* (3.5) *satisfies* $u^k_\Delta(t,x,y) \geq 0$ *for all* $k \in \{1,\dots,N\}$, $t \in \mathbb{R}_+$ *and* $(x,y) \in \mathbb{R}^2$.

Due to the conservative nature of the present Lax-Friedrichs type algorithm, positivity ensures that the $\mathbf{L_1}$ norm of the approximate solution remains constant.

Lemma 3.2.3 *(*$\mathbf{L_1}$ *bound). Let* (H0), (H1), (H3) *and* (3.7) *hold. Fix an initial datum* $U^0 \in (\mathbf{L_1} \cap \mathbf{L}_\infty(\mathbb{R}^2; \mathbb{R}^N_+)$. *Then the approximate solution* u_Δ *defined the algorithm* (3.5) *satisfies* $\|u_\Delta(t)\|_{\mathbf{L_1}} = \|u_\Delta(0)\|_{\mathbf{L_1}}$ *for* $k \in \{1,\dots,N\}$ *and* $t \in \mathbb{R}_+$.

The proof consists in studying $\|u^{n+1/2}_\Delta\|_{\mathbf{L_1}}$, and remarking that all fluxes cancel, see for instance [5, Lemma 2.4].
The following $\mathbf{L}_\infty$ bound ensures that the maximum of the approximate solution increases at most exponentially in time. This growth estimate is optimal and coincides with the classical one, see [63].

Lemma 3.2.4 *(*$\mathbf{L}_\infty$ *bound). Let* (H0), (H1), (H3) *and* (3.7) *hold. Fix an initial datum* $U^0 \in \mathbf{L_1} \cap \mathbf{L}_\infty)(\mathbb{R}^2; \mathbb{R}^N_+)$. *Then there exists a* $\mathcal{C}$ *depending only on* η, θ, $f^1,\dots,f^N$, $g^1,\dots,g^N$, *see* (A.5), *such that the approximate solution* u_Δ *defined by the algorithm* (3.5) *satisfies* $\|u_\Delta(t)\|_{\mathbf{L}_\infty} \leq e^{\mathcal{C}t(1+\|U^0\|_{\mathbf{L_1}})}\|U^0\|_{\mathbf{L}_\infty}$ *for all* $t \in \mathbb{R}_+$.

We get now the uniform bound on the total variation of the approximate solutions.

Lemma 3.2.5 *(*$\mathbf{BV}$ *bound). Let* (H0), (H1), (H2), (H3) *and* (3.7) *hold. Fix an initial datum* $U^0 \in (\mathbf{L_1} \cap \mathbf{L}_\infty \cap \mathbf{BV})(\mathbb{R}^2; \mathbb{R}^N_+)$. *Then there exist constants* $\mathcal{K}_1$ *and* $\mathcal{K}_2$, *see* (A.9), *depending only on* $\|U^0\|_{\mathbf{L_1}}$, η, θ, $f^1,\dots,f^N$, $g^1,\dots,g^N$, *such that the approximate solution* u_Δ *defined by the algorithm* (3.5) *satisfies*

$$\begin{aligned}
&\sum_{ij}\left(\left\|u^{k,n}_{i+1,j} - u^{k,n}_{ij}\right\|\Delta y + \left\|u^{k,n}_{i,j+1} - u^{k,n}_{ij}\right\|\Delta x\right)\\
&\leq e^{\mathcal{K}_1 t}\sum_{ij}\left(\left\|u^{k,0}_{i+1,j} - u^{k,0}_{ij}\right\|\Delta y + \left\|u^{k,0}_{i,j+1} - u^{k,0}_{ij}\right\|\Delta x\right) + \mathcal{K}_2(e^{\mathcal{K}_1 t} - 1)
\end{aligned}$$

for all n, *for all* $t \in [t^n, t^{n+1}[$ *and for all* $k = 1,\dots,N$.

Remark that $\mathcal{K}_2$ depends on all the components of U^0. Hence an initial datum with a constant component may lead to a solution with no constant components. In other words, the coupling among the different scalar equations in (3.1) allows the total variation to be transferred from one component to the others.
To prove discrete entropy inequalities, we introduce the Kružkov numerical entropy fluxes, see [5, Lemma 2.8], [31, Section 3], [32, Section 4]:

$$\begin{aligned}
\Phi^{k,n,\kappa}_{i+1/2,j}(a,b) &= f^{k,n}_{i+1/2,j}(a\vee\kappa, b\vee\kappa) - f^{k,n}_{i+1/2,j}(a\wedge\kappa, b\wedge\kappa),\\
\Gamma^{k,n,\kappa}_{i,j+1/2}(a,b) &= g^{k,n}_{i,j+1/2}(a\vee\kappa, b\vee\kappa) - g^{k,n}_{i,j+1/2}(a\wedge\kappa, b\wedge\kappa),
\end{aligned} \tag{3.8}$$

where we denote $a \vee b = \max\{a,b\}$ and $a \wedge b = \min\{a,b\}$.

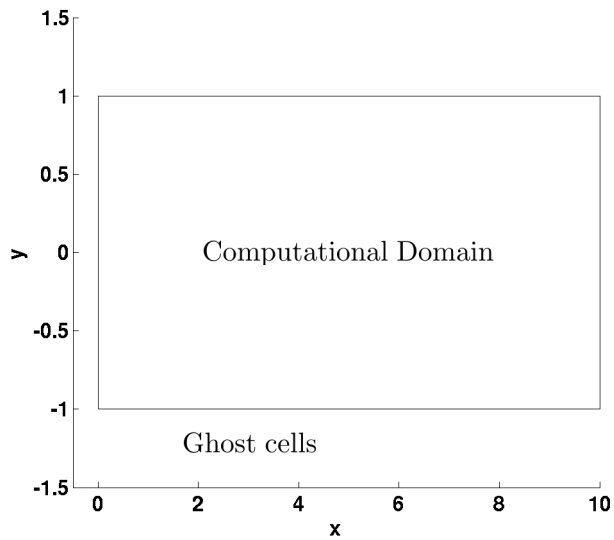

Figure 3.1: Computational domain for convergence tests.

Lemma 3.2.6 *(Discrete Entropy Condition). Let* (H0), (H1), (H2), (H3) *and* (3.7) *hold. Fix an initial datum* $U^0 \in (\mathbf{L_1} \cap \mathbf{L}_\infty \cap \mathbf{BV})(\mathbb{R}^2; \mathbb{R}_+)$*. Then the approximate solution* u *defined by the algorithm* (3.5) *satisfies*

$$\begin{aligned}
&\|u_{ij}^{k,n+1} - \kappa\| - \|u_{ij}^{k,n} - \kappa\| + \lambda_x \left(\Phi_{i+1/2,j}^{k,n,\kappa}(u_{ij}^{k,n}, u_{i+1,j}^{k,n}) - \Phi^{k,n,\kappa}(u_{i-1,j}^{k,n}, u_{ij}^{k,n}) \right) \\
&+\lambda_x \mathrm{sgn}(u_{ij}^{k,n+1/2} - \kappa)(f_{i+1/2,j}^{k,n}(\kappa) - f_{i-1/2,j}^{k,n}(\kappa)) \\
&+\lambda_y \left(\Gamma_{i,j+1/2}^{k,n+1/2,\kappa}(u_{ij}^{k,n+1/2}, u_{i,j+1}^{k,n+1/2}) - \Gamma_{i,j-1/2}^{k,n+1/2,\kappa}(u_{i-1,j}^{k,n+1/2}, u_{ij}^{k,n+1/2}) \right) \\
&+\lambda_y \mathrm{sgn}(u_{ij}^{k,n+1} - \kappa)(g_{i,j+1/2}^{k,n+1/2}(\kappa) - g_{i,j-1/2}^{k,n+1/2}(\kappa)) \leq 0
\end{aligned}$$

for all $i, j \in \mathbb{Z}, k = 1, \ldots, N,$ *and* $\kappa \in \mathbb{R}$*.*

As in [5, Lemma 2.8] for both fluxes $\Phi_{i+1/2,j}^{k,n,\kappa}$ and $\Gamma_{i,j+1/2}^{k,n,\kappa}$, we state that the updating $u^{n+1/2}$ is a monotone transformation. Then from it and the definition (3.8) of the entropic flux, we get the entropic inequality.

Lemma 3.2.7 *(*$\mathbf{L_1}$ *Lipschitz Continuity in time). Let* (H0), (H1), (H2), (H3) *and* (3.7) *hold. Fix an initial datum* $U^0 \in (\mathbf{L_1} \cap \mathbf{L}_\infty \cap \mathbf{BV})(\mathbb{R}^2; \mathbb{R}_+^2)$*. Then for any* $\bar{n} \in \mathbb{N}$*, there exists a constant* C *depending on* $\|U^0\|_{\mathbf{L_1}}$*,* $\boldsymbol{TV}(U^0)$*,* t^n*,* λ_x*,* λ_y*,* α*,* β *and on the functions* η*,* θ*,* f^k *and* g^k*, for* $k \in \{1, \ldots, N\}$ *such that for* $n = 1, \ldots, \bar{n}$ *the approximate solution* u_Δ *defined by* (3.5) *satisfies*

$$\|u_\Delta(t^{n+1}) - u_\Delta(t^n)\|_{\mathbf{L_1}} \leq C\Delta t. \tag{3.9}$$

The proof of Lemma 3.2.7 is a generalization of [5, Lemma 2.7].

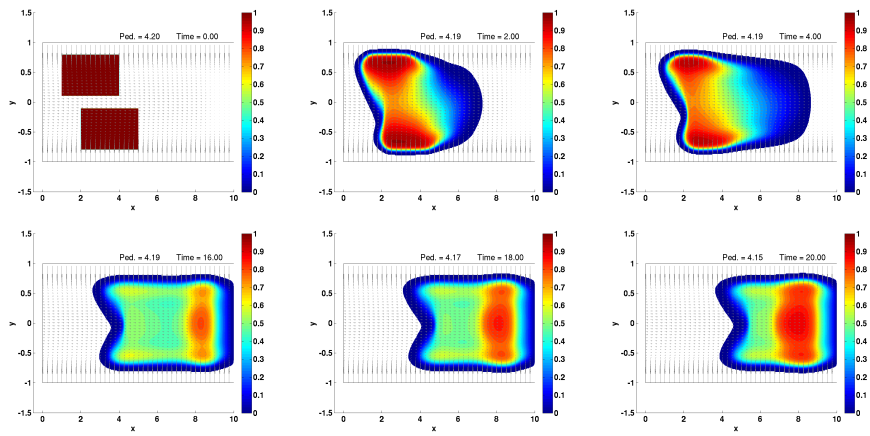

Figure 3.2: Solution to (3.1) at times $t = 0$, 2, 4, 16, 18 and 20 with absorbing boundary conditions and space mesh $\Delta x = \Delta y = 0.0125$, $\alpha = \beta = 0.333$ and CFL$= 1/7$.

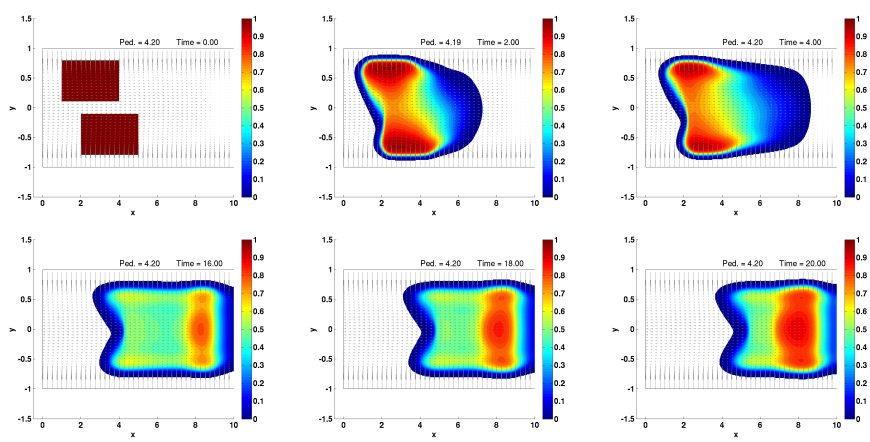

Figure 3.3: Solution to (3.1) at times $t = 0$, 2, 4, 16, 18 and 20 with zero flux boundary conditions and space mesh $\Delta x = \Delta y = 0.0125$, $\alpha = \beta = 0.333$ and CFL$= 1/7$.

Δx	$\|u_{\Delta x} - u_{\Delta x/2}\|_{\mathbf{L_1}}$	γ
0.05	0.54489748	0.2754
0.025	0.41369662	0.3725
0.0125	0.28505490	0.3541
0.00625	0.20006065	
0.003125		

Table 3.1: Convergence rate γ for the numerical scheme (3.5) on the domain $[0,10]\times[-1,1]$ at time $t = 1.0$ for the approximate solutions to the problem (3.1,3.10) with $\lambda_x = \lambda_y = 0.15$ and absorbing boundary conditions.

3.2.3 Numerical convergence of the numerical scheme

We estimate the convergence of the scheme (3.5) for problems with two kind of boundary conditions, knowing absorbing and zero-numerical flux conditions. It consists in the displacement of a crowd in a rectangular domain. It moves along a vector field ν chosen to make them stop at $x = 9.5$ with a strong repulsion at the walls. The domain is a corridor with dimension $[0,10]\times[-1,1]$, discretized with a cartesian grid $\Delta x = \Delta y$. We implement the boundary condition using *ghost cells* for the outer surrounding cells of the discretized domain, see Fig. 3.1. For the first boundary condition, we force the density at those cells to be $u_{ij} = 0$. For the latter one, we set the numerical flux to zero at the outside interface of the computational domain, $F_{i+\frac{1}{2},j} = 0$ and $G_{i,j+\frac{1}{2}} = 0$. Additionally we consider the density in the outside domain to be zero for the deviation computation for both conditions. Here the maximal density is 1 and the maximal speed is 1. The following flux is defined on the domain

$$\begin{aligned} f(t,x,y,U,A) &= U(1-U)\left[\nu_x(x,y) + \mathcal{I}_x(A)\right], \quad \eta = \mu \\ g(t,x,y,U,B) &= U(1-U)\left[\nu_y(x,y) + \mathcal{I}_y(B)\right], \quad \theta = \mu \end{aligned} \tag{3.10}$$

with

$$\nu(x,y) = \begin{bmatrix} (1-y^2)^3 \exp(x-9.5)^2 \chi_{]-\infty,9.5]\times[-1,1]}(x,y) \\ -2y\exp(1-1/y^2) \end{bmatrix}, \tag{3.11}$$

$$\mathcal{I}(A) = -\,\varepsilon \frac{\nabla A}{\sqrt{1+\|\nabla A\|^2}} \tag{3.12}$$

$$\tilde{\mu}(x,y) = \left(0.16 - x^2 - y^2\right)^3 \chi_{\{]-0.4,0.4]\times[-0.4,0.4]\}}(x,y), \quad \mu(x,y) = \frac{\tilde{\mu}(x,y)}{\iint_{\mathbb{R}^2}\tilde{\mu}},$$

so that $\iint_{\mathbb{R}^2}\mu = 1$ and A, B described as in (3.6).
We take as an initial value $U^0 \in (\mathbf{L_1}\cap\mathbf{L}_\infty\cap\mathbf{BV})(\mathbb{R}^2;[0,1])$

$$U^0(x,y) = \chi_{[1,4]\times[0.1,0.8]}(x,y) + \chi_{[2,5]\times[-0.8,-0.1]}(x,y) \tag{3.13}$$

The numerical integration of (3.2)-(3.10)-(3.13) obtained with the scheme (3.5) is shown in Figs. (3.2)-(3.3). The two groups will move to the right and merge, and the algorithm will stop at $t = 1$. We remark no dramatic differences between the two integration, despite a slight decrease in the total mass for the absorbing boundary conditions, see Fig. 3.2.

Δx	$\|u_{\Delta x} - u_{\Delta x/2}\|_{\mathbf{L_1}}$	γ
0.05	0.54209296	0.2703
0.025	0.41368130	0.3724
0.0125	0.28505490	0.3541
0.00625	0.20006065	
0.003125		

Table 3.2: Convergence rate γ for the scheme (3.5) on the domain $[0, 10] \times [-1, 1]$ at time $t = 1.0$ for the approximate solutions to the problem (3.1,3.10) with $\lambda_x = \lambda_y = 0.15$ and zero flux boundary conditions

The convergence rate is computed with the $\mathbf{L_1}$ distance between the numerical solutions $u_{\Delta x}$ and $u_{\Delta x/2}$ corresponding to a decreasing grid size with $\Delta x = \Delta y = h$. The results in Tab. 3.1 and Tab. 3.2 suggest that the numerical scheme might have a convergence rate $\gamma = \log_2 \frac{\|u_h - u_{h/2}\|}{\|u_{h/2} - u_{h/4}\|} \approx 0.3$ for both the absorbing and zero flux boundary conditions.

3.3 Optimization of the initial data for an evacuation problem

We focus now on an optimization problem using the model (3.1), with $N = 1$, $k = 1$ and $m = 1$ and writing $U^1 = U$. A group of pedestrians aims to exit a room and we want to find the best arrangement of the initial distribution to minimize the evacuation time.

3.3.1 Settings

The density U of pedestrians satisfies the following nonlocal continuity equation

$$\partial_t U + \mathrm{div}_{x,y} F\left(t, x, y, U, U * \eta\right) = 0 \tag{3.14}$$

with $F\left(t, x, y, U, U * \eta\right) = \left(V_{\max} U \left(1 - \frac{U}{U_{\max}}\right)\left(\nu + \mathcal{I}(\eta * U)\right)\right)$.
This conservation law describes macroscopically the behavior of a crowd where pedestrians evaluate their travel speed according to the density average around them. The scalar speed only depends on the local density with the maximal density $U_{\max} > 0$ and the maximal speed $V_{\max} > 0$. $\nu = (\nu_x, \nu_y)$ is a prescribed vector field for the preferred direction of the pedestrians, and $\mathcal{I}$ a deviation due to the *perceived* density such that

$$\mathcal{I}(\eta * U) = -\varepsilon \frac{\nabla(\eta * U)}{\sqrt{1 + \|\nabla(\eta * U)\|^2}}, \tag{3.15}$$

with $\varepsilon > 0$. η is a smooth nonnegative and with a compact support kernel representing how pedestrians average the density around them to correct their path such that

$$\eta(x, y) = \left(1 - \left(\frac{x}{r}\right)^2\right)^3 \left(1 - \left(\frac{y}{r}\right)^2\right)^3, r > 0. \tag{3.16}$$

The domain Ω is subdivided in Ω_{ped} where pedestrians walk and Ω_{wall} where they cannot such that $\Omega = \Omega_{\text{ped}} \cup \Omega_{\text{wall}}$, see Fig. 3.4. We state that $\Gamma_w = \partial\Omega_{\text{wall}} \cap \partial\Omega_{\text{ped}}$ is the interface

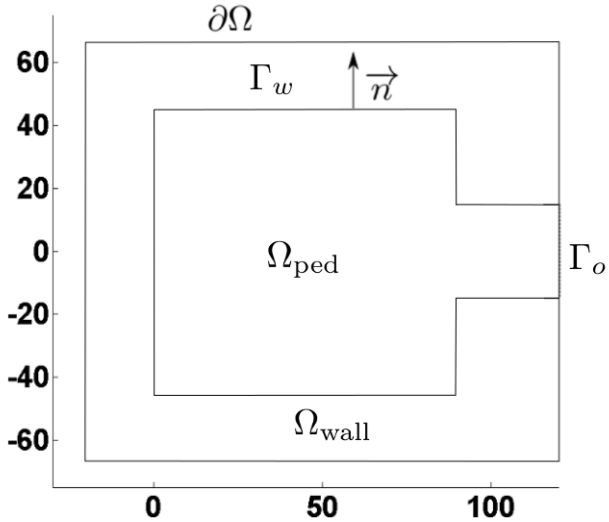

Figure 3.4: Representation of the domain Ω and its different subdivisions.

between walls and the pedestrian area, and $\Gamma_o = \partial\Omega \cap \partial\Omega_{\text{ped}}$ the exit. We add to (3.14) the following boundary conditions

$$\begin{cases} U(t,x,y) = 0, & \forall (x,y) \in \Gamma_o,\ \forall t \in \mathbb{R}^+, \\ \langle F, \vec{n} \rangle = 0, & \forall (x,y) \in \Gamma_w,\ \forall t \in \mathbb{R}^+, \end{cases} \tag{3.17}$$

with $\vec{n}$ the exterior normal of Γ_w.
We call $\Omega_{\text{ctrl}} \subset \Omega_{\text{ped}}$, see Fig. 3.5, where the initial distribution $U(0,x,y) = U^0(x,y) : \Omega \mapsto \mathbb{R}^+$ must be nonnegative, such that

$$\begin{cases} 0 \leq U^0(x,y) \leq U_{\max}, & \forall (x,y) \in \Omega_{\text{ctrl}}, \\ \int_\Omega U^0(x,y)\,\mathrm{d}x\mathrm{d}y = U_{\text{init}} & \forall (x,y) \in \Omega_{\text{ctrl}}, \\ U^0(x,y) = 0 & \forall (x,y) \notin \Omega_{\text{ctrl}}, \end{cases} \tag{3.18}$$

with U_{init} a given positive constant representing the quantity of pedestrians.
The computational domain consists in a grid composed of a central region where the flux is nonlocal and surrounded by a region with a thickness greater than the radius of the compact support kernel η, see Fig. 3.6. We set the flux to be local in the latter region because from our knowledge, there is no results for this boundary problems with nonlocal conservation laws.
From a numerical point of view, we denotes three kind of regions: the one where the nonlocal deviation is computed, the one where the deviation is set to zero and the one where the numerical flux is set to 0. We gather the two first as pedestrian regions in Ω_{ped} and the last one is named Ω_{wall}. We can see on Fig 3.6 that the first region Ω_{nonlocal} corresponds to a the main pedestrian area, then Ω_{local} corresponds to a small buffer region before the exit, like a corridor, and the final one Ω_{wall} corresponds to the walls. The numerical flux at the interface between Ω_{wall} and Ω_{ped} is $F = 0$ horizontally and $G = 0$ vertically.

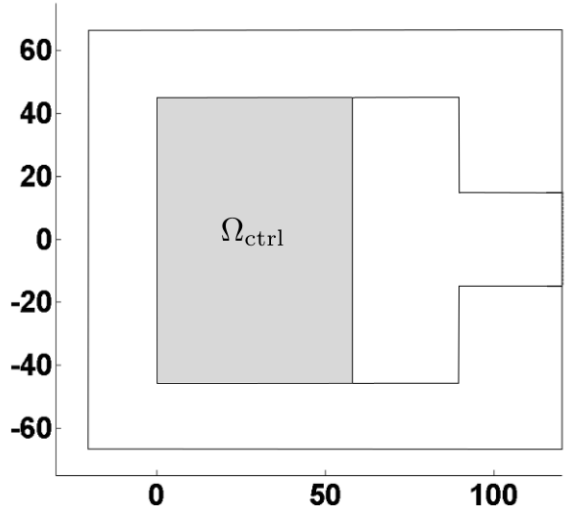

Figure 3.5: Control domain Ω_{ctrl} in Ω.

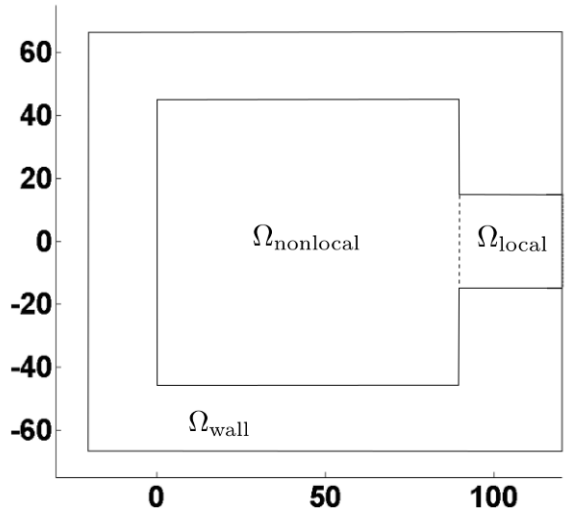

Figure 3.6: Numerical domain partition in Ω.

3.3.2 Formulation of the optimization problem

The optimization problem consists of minimizing the total travel time of the evacuation respecting the constraints given by (3.1), (3.17) and (3.18). The optimization problem for the initial data $U^0 \in (\mathbf{L_1} \cap \mathbf{L}_\infty \cap \mathbf{BV})(\mathbb{R}^2; \mathbb{R}_+^N)$ reads

$$\min_{U^0 \in \mathbf{L}^\infty(\Omega_{\text{ctrl}};[0,U_{\max}])} \mathcal{J}(U^0) = \min_{U^0 \in \mathbf{L}^\infty(\Omega_{\text{ctrl}};[0,U_{\max}])} \int_{\mathbb{R}^+} \int_\Omega U_{U^0}(t,x,y)\,\mathrm{d}t\,\mathrm{d}x\,\mathrm{d}y, \tag{3.19}$$
$$\text{subject to (3.14), (3.17) and (3.18)}$$

where U_{U^0} represents the solution associated to U^0, defined in Ω_{ctrl}.

3.3.3 Discrete formulation

We solve this problem using a *first discretize-then-optimize* approach, i.e. we will optimize the descretized formulation of problem as in [75, 79].
We call $\Omega^\Delta_{\text{name}}$ the discretized version of Ω_{name} using the mesh (3.4) (and in the similar way for Γ). We denote by u_Δ the discrete solution of (3.1) and with a slight abuse of notation $(u_\Delta)_{ij} = u_{ij} \approx U(x_i, y_j)$.
At the boundary, we set a discrete zero numerical flux $F = 0/G = 0$ at the interface Γ^Δ_w, and $u_\Delta = 0$ at Γ^Δ_o.

$$\begin{cases} u_\Delta = 0 \text{ at } \Gamma^\Delta_o, \\ F = 0,\ G = 0 \text{ at } \Gamma^\Delta_w. \end{cases} \tag{3.20}$$

Admissible controls correspond to the cells value of a parametrization of U^0 with a piecewise constant map on Ω_{ctrl}. We choose here to discretize U^0 with a grid as (3.4) with $(\Delta x)_M = (\Delta y)_M$ multiple of Δx. We have then $\mathbf{u}^0_m = \sum_{ij} u_{ij} \frac{\Delta x \Delta y}{(\Delta x)_M (\Delta y)_M}$ for (x_i, y_j) in the corresponding cell m, $m = 1...M$. We define

$$\mathcal{U} = \left\{ \mathbf{u}^0 \in \mathbb{R}^M \ : \ \begin{array}{c} 0 \le \mathbf{u}^0_m \le U_{\max}, \\ \sum_m \mathbf{u}^0_m (\Delta x)_M (\Delta y)_M = U_{\text{init}} \end{array} \quad m = 1...M \right\} \tag{3.21}$$

The discretization (3.5) yields the problem with the discrete cost function J

$$\min_{\mathbf{u}^0 \in \mathcal{U}} J(\mathbf{u}^0) = \min_{\mathbf{u}^0 \in \mathcal{U}} \sum_{n=0}^{N_t} \sum_{(i,j) \in [1...N_x] \times [1...N_y]} (u^n_{ij})_{\mathbf{u}^0} \Delta x \Delta y \Delta t \tag{3.22}$$
$$\text{subject to (3.5), (3.20) and (3.21)}$$

where N_t is the number of time steps, and N_x and N_y the number of cells in the horizontal and vertical directions and $u_{\mathbf{u}^0}$ the discretized solution associated with to $\mathbf{u}^0$.

3.3.4 Formulation of the cost function gradient

We solve the optimization problem (3.22) with a gradient descent method. At each optimization step, we compute ∇J. To this end, we transform the PDE-constrained problem (3.22) into an unrestricted one using a Lagrangian formulation. The Lagrangian will take in account

step and half steps of the fractional step integration and, as u_Δ, $\boldsymbol{\phi}$ lies in $\mathbb{R}^{2N_t} \times \mathbb{R}^{N_x} \times \mathbb{R}^{N_y}$. The Lagrangian reads:

$$L(\mathbf{u}^0, u_\Delta, \boldsymbol{\phi}) = \sum_{n=0}^{N_T} \sum_{ij} u_{ij}^n \Delta x \Delta y \Delta t$$

$$+ \sum_{n=0}^{N_T-1} \sum_{ij} \boldsymbol{\phi}_{ij}^n \left(\frac{u_{ij}^{n+1/2} - u_{ij}^n}{\Delta t} + \frac{F_{i+1/2,j}^n - F_{i-1/2,j}^n}{\Delta x} \right) \tag{3.23}$$

$$+ \sum_{n=0}^{N_T-1} \sum_{ij} \boldsymbol{\phi}_{ij}^{n+1/2} \left(\frac{u_{ij}^{n+1} - u_{ij}^{n+1/2}}{\Delta t} + \frac{G_{i,j+1/2}^{n+1/2} - G_{i,j-1/2}^{n+1/2}}{\Delta y} \right) \tag{3.24}$$

We formally derive the following optimality system by assuming sufficient regularity conditions. The state equation results from the derivative with respect to the Lagrange multipliers $\boldsymbol{\phi}_{ij}^n$, and the adjoint equations are given from the Lagrangian derivative with respect to the density. We also introduce the indicator function χ^F (resp. χ^G) returning 1 for a vertical interface (resp. horizontal) between two cells of $\Omega_{\text{ped}}^\Delta$ and 0 otherwise for the boundary part of the Lagrangian. The detail of the following computation is in Appendix B.
Derivating (3.23) with respect to u_{ij}^n

$$\begin{aligned}
&\Delta t \partial_{u_{ij}^n} L(\mathbf{u}^0, u_\Delta, \boldsymbol{\phi}) \\
&= \Delta x \Delta y \Delta t^2 + \boldsymbol{\phi}_{ij}^{n-1/2} - \boldsymbol{\phi}_{ij}^n \\
&+ \lambda_x \sum_{\substack{r \in [1 \dots N_x] \\ s \in [1 \dots N_y]}} \boldsymbol{\phi}_{rs}^n \left[\partial_{u_{ij}^n} F_{r+1/2,s}^n \chi_{r+1/2,s}^F - \partial_{u_{ij}^n} F_{r-1/2,s}^n \chi_{r-1/2,s}^F \right]
\end{aligned} \tag{3.25}$$

Writing $f_{ij}(u) = \bar{f}(u) \left(\nu_x + \mathcal{I}_x\right)_{ij}$ and $g_{ij}(u) = \bar{g}(u) \left(\nu_y + \mathcal{I}_y\right)_{ij}$ with

$$\bar{f}(u) = \bar{g}(u) = V_{\max} u \left(1 - \frac{u}{U_{\max}}\right),$$

we obtain from (3.14)

$$\begin{aligned}
\partial_{u_{ij}^n} f_{rs}(u) &= \partial_{u_{ij}^n} \bar{f}(u) (\nu_x + \mathcal{I}_x(u))_{rs} + \bar{f}(u) \partial_{u_{ij}} \left[\mathcal{I}_x\right](u), \\
\partial_{u_{ij}^n} g_{rs}(u) &= \partial_{u_{ij}^n} \bar{g}(u) (\nu_y + \mathcal{I}_y(u))_{rs} + \bar{g}(u) \partial_{u_{ij}^n} \left[\mathcal{I}_y\right](u).
\end{aligned}$$

We state $\bar{f}_{ij}^n = \bar{f}(u_{ij}^n)$ and $\bar{g}_{ij}^n = \bar{g}(u_{ij}^n)$ and we introduce Φ_{rs}^f and Φ_{rs}^α, see (B.1), $\overline{(\partial_x \eta)}$ and $\overline{(\partial_y \eta)}$, see (B.3), and $\boldsymbol{\Phi}_1^n$ and $\boldsymbol{\Phi}_2^n$, see (B.4), to have the final expression of the Lagrangian derivative

$$\begin{aligned}
\Delta t \partial_{u_{ij}^n} L(\mathbf{u}^0, u_\Delta, \boldsymbol{\phi}) &= \Delta x \Delta y \Delta t^2 + \boldsymbol{\phi}_{ij}^{n-1/2} - \boldsymbol{\phi}_{ij}^n + \left(\frac{-\alpha}{2}\right) \Phi_{ij}^\alpha \\
&+ \lambda_x \left(\Phi_{ij}^f \left(\nu_x + \mathcal{I}_x\right)_{ij} \partial_{u_{ij}^n} \bar{f}_{ij}^n + \left(\boldsymbol{\Phi}_1^n * \overline{(\partial_x \eta)}\right)_{ij} + \left(\boldsymbol{\Phi}_2^n * \overline{(\partial_y \eta)}\right)_{ij} \right).
\end{aligned}$$

Stating $\Delta t \partial_{u_{ij}^n} L(\mathbf{u}^0, u_\Delta, \boldsymbol{\phi}) = 0$, and computing Φ_{rs}^g and Φ_{rs}^β, $\mathbf{\Phi}_1^{n+1/2}$ and $\mathbf{\Phi}_2^{n+1/2}$ in a similar way, it yields the following adjoint equations

$$\begin{aligned}
\boldsymbol{\phi}_{ij}^n &= \boldsymbol{\phi}_{ij}^{n+1/2} - \left(\frac{-\beta}{2}\right)\Phi_{ij}^\beta - \lambda_y \left(\Phi_{ij}^g \left(\nu_y + \mathcal{I}_y\right)_{ij} \partial_{u_{ij}^{n+1/2}} \bar{g}_{ij}^{n+1/2}\right. \\
&\quad \left. + \left(\mathbf{\Phi}_1^{n+1/2} * \overline{(\partial_x \eta)}\right)_{ij} + \left(\mathbf{\Phi}_2^{n+1/2} * \overline{(\partial_y \eta)}\right)_{ij}\right) \\
\boldsymbol{\phi}_{ij}^{n-1/2} &= -\Delta x \Delta y \Delta t^2 + \boldsymbol{\phi}_{ij}^n - \left(\frac{-\alpha}{2}\right)\Phi_{ij}^\alpha - \lambda_x \left(\Phi_{ij}^f \left(\nu_x + \mathcal{I}_x\right)_{ij} \partial_{u_{ij}^n} \bar{f}_{ij}^n\right. \\
&\quad \left. + \left(\mathbf{\Phi}_1^n * \overline{(\partial_x \eta)}\right)_{ij} + \left(\mathbf{\Phi}_2^n * \overline{(\partial_y \eta)}\right)_{ij}\right)
\end{aligned}$$

with the following final condition

$$\boldsymbol{\phi}_{ij}^{N_t} = 0$$

Therefore we get

$$\begin{aligned}
\frac{\partial J}{\partial u_{ij}^0} =& \Delta x \Delta y \Delta t - \frac{1}{\Delta t}\boldsymbol{\phi}_{ij}^0 + \frac{-\alpha}{2\Delta t}\Phi_{ij}^\alpha + \frac{1}{\Delta x}\left(\Phi_{ij}^f \left(\nu_x + \mathcal{I}_x\right)_{ij} \partial_{u_{ij}^0} \bar{f}_{ij}^0\right. \\
&\left. + \left(\mathbf{\Phi}_1^0 * \overline{(\partial_x \eta)}\right)_{ij} + \left(\mathbf{\Phi}_2^0 * \overline{(\partial_y \eta)}\right)\right).
\end{aligned}$$

Knowing that the discrete cost function depends on the initial value in the cells, and thus of the values of $\mathbf{u}^0$, such that $J = J\left(\left\{u_{ij}^0(\mathbf{u}^0)\right\}_{ij}\right)$ for all $i = 1...N_x$, $j = 1...N_y$, we finally get

$$\nabla_{\mathbf{u}_m^0} J = \sum_{i,j} \frac{\partial J}{\partial u_{ij}^0} \frac{\mathrm{d}u_{ij}^0}{\mathrm{d}\mathbf{u}_m^0}.$$

3.3.5 Numerical validation of the gradient

We aim to validate numerically the computation of the cost function gradient for (3.22), comparing it to the gradient estimated via finite differences. We fix the experiment constants:

$$\begin{array}{lll}
U_{\max} = 4 \text{ ped}.m^{-2}, & \nu_x = 1, & \Delta x = \Delta y = 1m, \\
V_{\max} = 1m.s^{-1}, & \nu_y = 0, & \lambda_x = \lambda_y = 0.25, \\
U_{\text{init}} = 7 \text{ ped}, & \varepsilon = 0.5. & \\
T_{\max} = 8s, & &
\end{array}$$

The domain Ω is a $7m \times 5m$ rectangle with a room in $\Omega_{\text{nonlocal}} = [0,3] \times [0,1]$ and a corridor in $\Omega_{\text{loc}} = [3,5] \times [0,1]$. The remaining of the domain corresponds to Ω_{wall}, such $\Omega = \Omega_{\text{ped}} \cup \Omega_{\text{wall}}$, with $\Omega_{\text{ped}} = \Omega_{\text{nonlocal}} \cup \Omega_{\text{local}}$, see Fig 3.7.
We choose a coarse discretization $\Delta x = \Delta y = 1$ to numerically evaluate the convergence of the gradient obtained with the adjoint state. We validate numerically here the adjoint formula for zero density inside walls. The wall density will be taken in account in future works. We call c_{ij} the cell centered in (i,j). The initial data $\mathbf{u}^0$ is defined in $\Omega_{\text{ctrl}} \subset \Omega_{\text{nonlocal}}$ such that

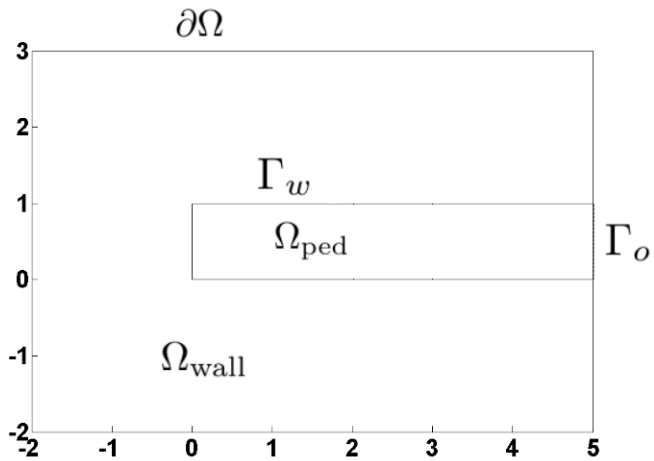

Figure 3.7: The 7×5 domain Ω.

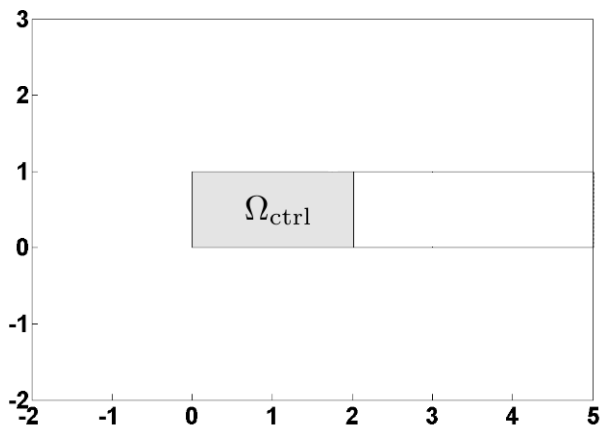

Figure 3.8: Control domain Ω_{ctrl} in Ω.

	$\nabla_{\mathbf{u}_1^0} J$	$\nabla_{\mathbf{u}_2^0} J$
$\text{DF}_{\delta U=10^{-3}}$	7.3489726	7.2069695
$\text{DF}_{\delta U=10^{-4}}$	7.3490886	7.2072204
$\text{DF}_{\delta U=10^{-5}}$	7.3491002	7.2072455
$\text{DF}_{\delta U=10^{-6}}$	7.3491014	7.2072481
ADJ	7.3491015	7.2072483

Table 3.3: Convergence results for the cost function gradient.

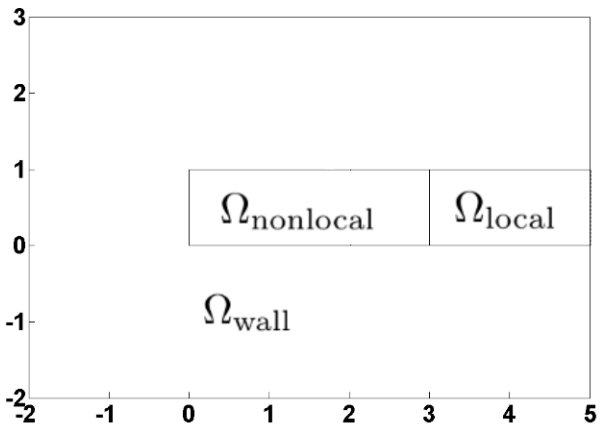

Figure 3.9: Numerical domain partition in Ω.

$\Omega_{\text{ctrl}} = [0,2] \times [0,1]$, see Figs. 3.8 and 3.9. The values of $\mathbf{u}^0$ are identified to the finite volume cells $u^0_{0,0}$ for $\mathbf{u}^0_1$ and $u^0_{1,0}$ for $\mathbf{u}^0_2$. $\mathcal{I}$ is zero on Ω_{loc}.
We compute the gradient of the cost function with respect to $\mathbf{u}^0_1$ and $\mathbf{u}^0_2$, with finite differences for $\delta U = 10^{-3}$, $\delta U = 10^{-4}$, $\delta U = 10^{-5}$ and $\delta U = 10^{-6}$, and with the adjoint state method.
According to Table 3.3, the sequence of finite difference gradients converges towards the gradient computed with adjoint state.

3.3.6 Optimization results

In this part we want to evaluate the impact of computing the cost function gradient for nonconvex optimization problem instead of estimating it with finite differences. We aim to optimize the total travel time of the evacuation of the room by reshaping the initial distribution of pedestrians. We will use the MATLAB nonlinear solver `fmincon` with the `active-set` algorithm. The maximal Evaluations (Eval) number is 120 000 and the maximal Iterations number (Iter) is 400. For each optimization we output the success of convergence, the optimal cost value, the number of Eval and Iter, and the computation time T_{Comp} on a desktop computer (Intel Xeon E7 2.8 GHz). Additionally we plot the optimal initial distribution of pedestrians and the evolution of the cost function J for both finite difference and adjoint state method.
The domain consists in a square room of $90m$ side connected to a $30m$ wide corridor on the right side, see Fig. 3.10. Additionally we have two sliders on the right side of the room joining the top and bottom walls to the corridor with an angle of 45°. We define as Ω_{nonlocal} the room and Ω_{local} the corridor, see Fig. 3.11. The union of both regions is Ω_{ped} and the remaining part of the domain is Ω_{wall}. Furthermore we define the discomfort region $\Omega_{\text{disc}} \subset \Omega_{\text{ped}}$ as a strip band along the walls, see Fig. 3.13, and the controls region $\Omega_{\text{ctrl}} \subset \Omega_{\text{nonlocal}}$, see Fig. 3.12 where the initial density reshaping will occur.
The vector field ν represents the natural direction of pedestrians in an empty room with a strong discomfort in the vicinity of walls, see Fig. 3.14. It is the normalized sum of ν_{ped}, the gradient of the eikonal solution on Ω_{ped}, and ν_{disc}, a linearly decreasing discomfort on Ω_{disc}.

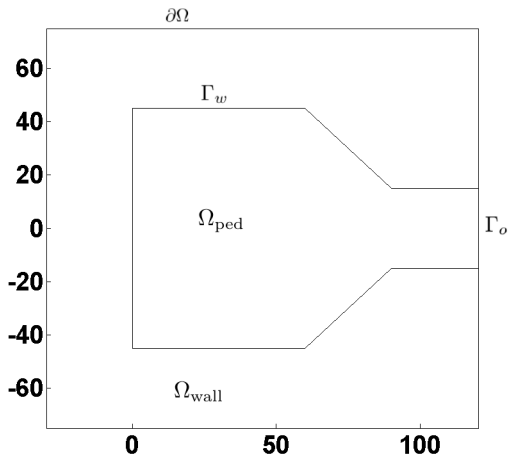

Figure 3.10: The domain Ω.

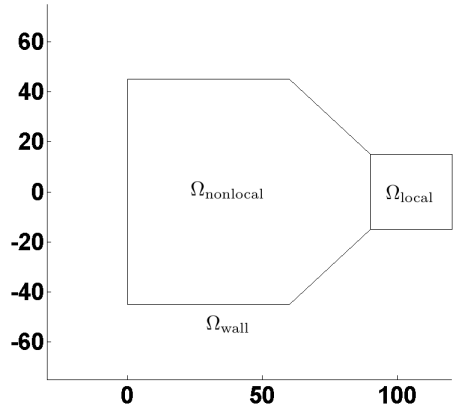

Figure 3.11: Numerical domain partition on Ω.

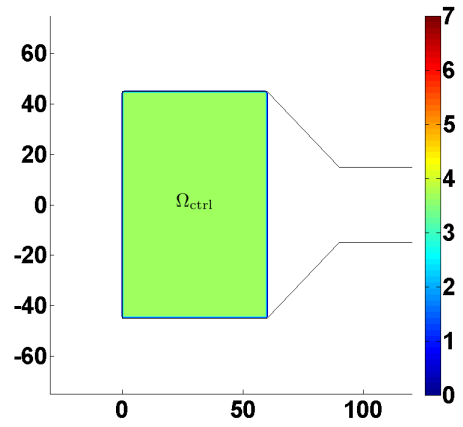

Figure 3.12: Control domain Ω_{ctrl} in Ω with an initial mass of pedestrian $U_{\text{init}} = 20\,000$ ped.

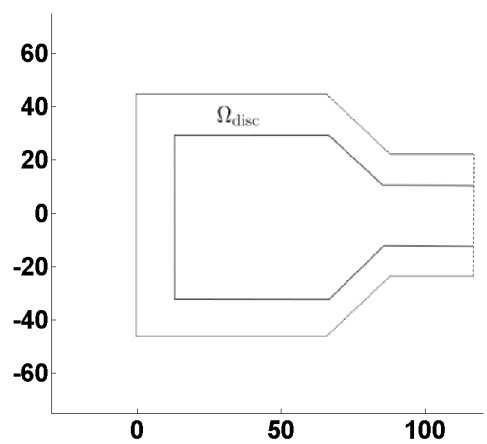

Figure 3.13: Discomfort region along the walls (unscaled).

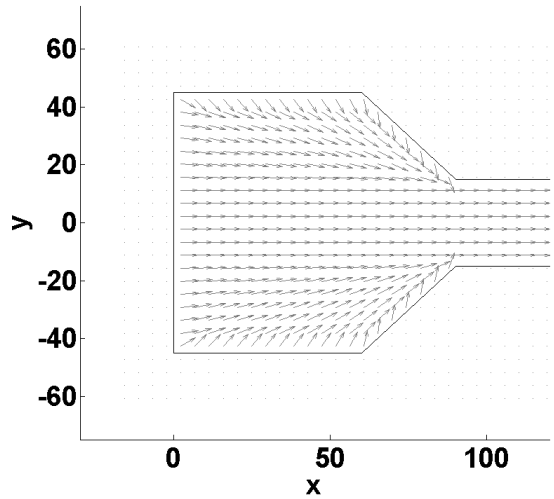

Figure 3.14: Vector field ν on Ω_{ped}.

	Cvg	J	Eval	Iter	$T_{\text{Comp}}(s)$
Fin. Diff.	X	289 404.32	10 198	400	59 729
Adj. Stat.	✓	289 403.63	39	17	5 733

Table 3.4: Outputs of the optimization procedure for 24 control cells with and $\varepsilon = 0$ for finite differences and adjoint state method.

The deviation $\mathcal{I}$ will take in account only the density of pedestrians and consider Ω_{wall} as an empty space.
We distribute on Ω_{ctrl} an homogeneous crowd of 20 000 persons, see Fig. 3.12 and set the experiment constants, where $T_{\max}$ is chosen large enough to let everybody leave the room:

$$\begin{array}{cc} U_{\max} = 7 \text{ ped}.m^{-2}, & \Delta x = \Delta y = 1.5\, m, \\ V_{\max} = 2\, m.s^{-1}, & \lambda_x = \lambda_y = 1/7\, s.m^{-1}, \\ U_{\text{init}} = 20,000 \text{ ped}, & \varepsilon = 8, \\ T_{\max} = 260\, s. & \end{array}$$

The computational domain consists of a cartesian grid with $\Delta x = \Delta y = 1.5\, m$. The discretization of diagonals consists in stair curves such that the discrete domain is symmetric with respect to the axis $y = 0$. At the wall interface Γ_w, we set the numerical fluxes $F = 0$ for vertical interfaces and $G = 0$ for horizontal interfaces and at the exit Γ_o the density is set to $u_{ij}^n = 0$ for all time steps.
We conduct six tests, with different ε and parametrizations of the initial data.
Test 1. We take a local flux in (3.14), i.e. $\varepsilon = 0$, and the initial data parametrized in 24 controls. The optimal distribution is depicted on Fig 3.15. The finite difference reached the maximal number of optimization iteration Iter and did not converge.
Test 2. We take a nonlocal flux in (3.14) with $\varepsilon = 8$ and the initial data parametrized in 24 controls. The optimal distribution is depicted on Fig 3.17.

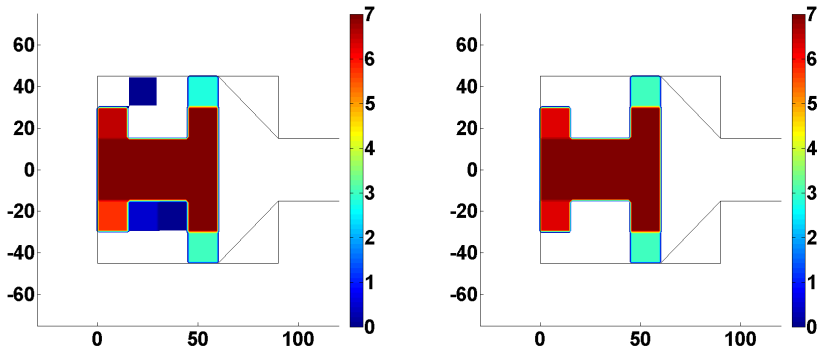

Figure 3.15: Optimal solution with 24 control cells and $\varepsilon = 0$ computed with finite differences on the left side and adjoint state method on the right side.

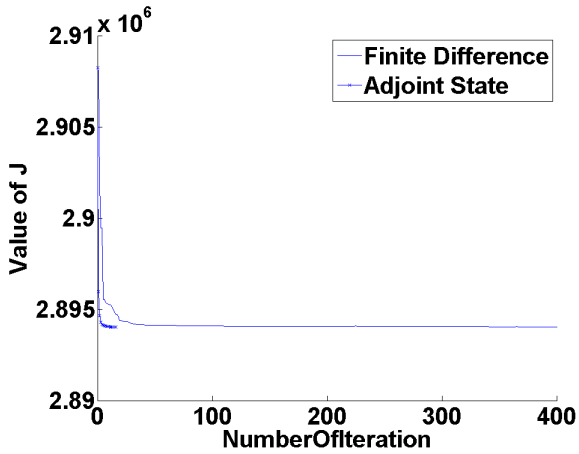

Figure 3.16: Evolution of J for 24 control cells with $\varepsilon = 0$ for finite differences and adjoint state method.

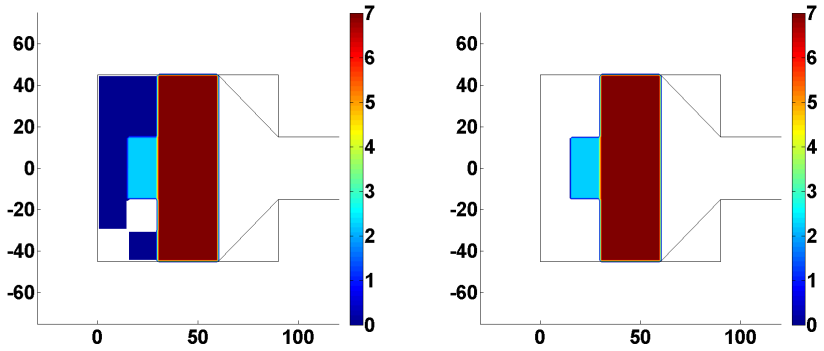

Figure 3.17: Optimal solution with 24 control cells and $\varepsilon = 8$ computed with finite differences on the left side and adjoint state method on the right side.

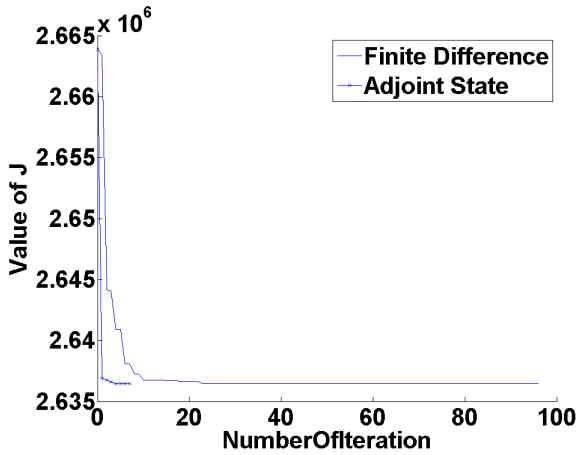

Figure 3.18: Evolution of J for 24 control cells with $\varepsilon = 8$ for finite differences and adjoint state method.

	Cvg	J	Eval	Iter	$T_{\text{Comp}}(s)$
Fin. Diff.	X	263 643.88	2 681	97	14 365
Adj. Stat.	✓	263 643, 63	15	8	1 598

Table 3.5: Outputs of the optimization procedure for 24 control cells with and $\varepsilon = 8$ for finite differences and adjoint state method.

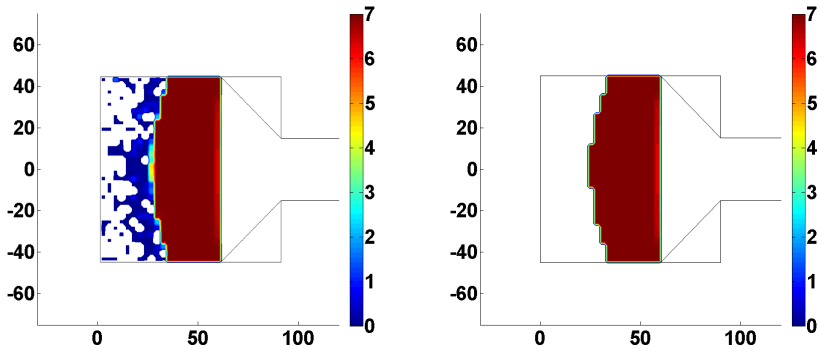

Figure 3.19: Optimal solution with 600 control cells and $\varepsilon = 8$ computed with finite differences on the left side and adjoint state method on the right side.

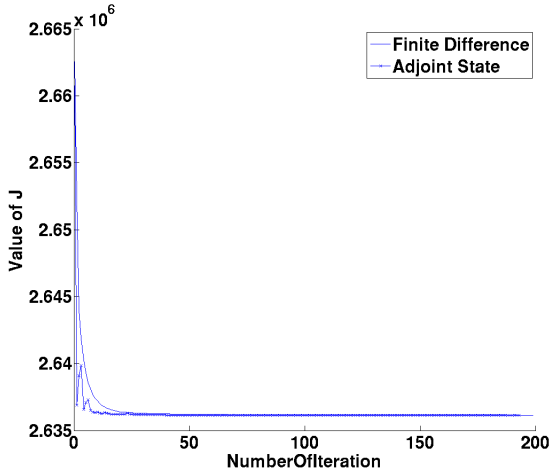

Figure 3.20: Evolution of J for 600 control cells with $\varepsilon = 8$ for finite differences and adjoint state method.

Test 3. We take a nonlocal flux in (3.14) with $\varepsilon = 8$ and the initial data parametrized in 600 controls. The optimal distribution is depicted on Fig 3.19. The finite difference reached the maximal number of function calls Eval and did not converge.
According to Tables (3.4-3.6), the adjoint state method improves the optimization procedure and reaches an optimal solution with less iterations, function calls and finally computation time.

3.4 Conclusion

Nonlocal fluxes in conservation laws describe the adjustment of the pedestrian's direction; when they take in account the density around them, they tend to form lanes.
In this chapter we have shown the convergence of a Lax-Friedrichs type numerical scheme for a general nonlocal flux to a weak entropy solution of the Cauchy problem (3.1). We estimated

	Cvg	J	Eval	Iter	$T_{\text{Comp}}(s)$
Fin. Diff.	X	263 615.64	120 285	199	700 382
Adj. Stat.	✓	263 612.99	1 453	194	167 865

Table 3.6: Outputs of the optimization procedure for 600 control cells with and $\varepsilon = 8$ for finite differences and adjoint state method.

numerically the convergence order of the scheme for two boundary problems with inward vector field at the boundary. We then investigated the efficiency of an adjoint state method on the optimization of nonlocal problems corresponding to room evacuations. We showed that it gives dramatic improvements in terms of iteration number and computational time.
This preliminary study set up the basis of a framework for optimization problems controlled by initial data. On one hand, the nonlocal flux has to be extend over the whole domain, including an investigation on the nonlocality at the interface and beyond for the boundary value problem. On the other hand, the existence of a weak entropy solution and of the computation of its approximation through the numerical scheme (3.5) has to be extend to the boundary-value problem, in order to develop more realistic settings involving lane formation in complex geometry as for instance railway stations.

Conclusion and perspectives

In this thesis, we introduced three PDE-based models describing the pedestrian traffic in various situations.

First, the evacuation of a crowd in a long narrow corridor with two opposite exits has been modeled by a scalar conservation law with space-discontinuous flux function for which the discontinuity location depends nonlocally on the density profile.
We coded an adapted wave front tracking scheme, assumed to give good approximation of the problem's solution. These wave front tracking approximations were used as reference solutions to show numerically the convergence of classical finite volume schemes, supporting their use for the computation of solutions of Hughes' model. However the convergence of wave front tracking approximations is still an open question.

In the second chapter, a simplified model for the motion of two groups of people walking in opposite directions has been proposed. It consists of a system of two conservation laws of mixed hyperbolic-elliptic type.
We investigated the model properties to conjecture an admissible solution to the Riemann problem for initial data in the hyperbolic region, but the global existence and uniqueness of solutions is still an open question. We presented a Lax-Friedrichs finite volume scheme, and proved a bound of the approximate solutions to ensure the convergence towards Young measures. Following [43], we computed the averages of sequences of solutions with persisting oscillations and get the expected values and the variances for densities and fluxes. Results suggest that recasting the corresponding Cauchy problem in the framework of measure-valued solutions allows to recover the flow characteristics. The instabilities observed in the elliptic region could be related to the auto-organization phenomena that result in a transition from a mixture to separate phases, corresponding to the lane formation in crowds crossing.

Finally, in the third chapter, we described the deviation of the pedestrian's direction in a model based on a conservation law with a nonlocal flux in two dimensions.
We showed the convergence of a Lax-Friedrichs type numerical scheme for a general nonlocal flux to a weak entropy solution of the corresponding Cauchy problem. We estimated numerically the convergence order of the scheme for two boundary value problems with repulsive vector field at the boundary. Then we showed the efficiency of an adjoint state method for optimization problems corresponding to room evacuations.

The modeling of pedestrian movements is a fruitful research field where many improvements could be realized, from the validation of existing models to the creation of new representations integrating more features. In particular, the pedestrian's ability to forecast, to decide and to fail is crucial in optimization and control of traffic flow. Nonlocal models in space are an interesting representation of the pedestrian's assimilation of the information. One can go further by integrating a nonlocal effect in time, like a memory effect, to describe

the behavior evolution of pedestrians in a usually congested place, like increased attention or a lower speed. Moreover first order macroscopic models struggle to achieve phenomena like *blocking archs*. Validation is therefore a critical step to build confidence in macroscopic models. Hence much work remains to develop a consistent mathematical framework handling nonclassical conservation laws for a broad application to pedestrian traffic.

Conclusion et perspectives

Dans cette thèse, on a introduit trois modèles basés sur des équations aux dérivées partielles non-linéaires décrivant le trafic piétonnier dans différentes situations.

D'abord, l'évacuation d'un couloir avec deux sorties a été modélisée par une loi de conservation scalaire avec un flux discontinu en espace et en temps, dont la discontinuité se déplace selon la distribution de densité. On a adapté la méthode de suivi des fronts afin d'obtenir de bonnes approximation de la solution du problème. Ces approximations ont été utilisées comme solutions de référence pour montrer numériquement la convergence des schémas de volumes finis classiques, confortant leur utilisation pour l'intégration numérique du modèle de Hughes. Cependant la preuve de convergence de la méthode de suivi des fronts pour ce problème reste une question ouverte.

Dans le second chapitre, un modèle pour le déplacement de deux groupes marchant en sens contraire a été proposé. Il se compose de deux lois de conservation formant un système de type mixte hyperbolique-elliptique. On a détaillé les propriétés du modèle afin de conjecturer des solutions admissibles au problème de Riemann pour des données initiales dans des régions hyperboliques. Cependant l'unicité des solutions reste un problème ouvert. On a présenté ensuite un schéma aux volumes finis dérivé de Lax-Friedrichs, et prouvé une borne uniforme de la solution approchée assurant la convergence vers une mesure de Young. En suivant [43], on a calculé la moyenne de séquences de solutions approchées avec des oscillations persistantes, afin d'obtenir les espérances de la densité et du flux. Ces résultats suggèrent que la reformulation du problème de Cauchy correspondant dans le cadre des mesures de probabilité permet de récupérer les caractéristiques de l'écoulement. Les instabilités observées dans la région elliptique peuvent être mis en relation à la transition depuis une mixture vers des phases séparées, correspondant à la formation de groupes de piétons.

Dans le dernier chapitre, on a décrit un modèle non-local de trafic où le piéton dévie de sa trajectoire en fonction de sa perception de la distribution de densité autour de lui. On a montré la convergence d'un schéma numérique de type Lax-Friedrichs pour un flux non-local général vers une solution faible entropique du problème de Cauchy associé. On a estimé numériquement l'ordre de convergence du schéma pour deux problèmes de bord avec un champ répulsif au bord. Ensuite on a montré l'efficacité d'une méthode de descente de gradient basée sur la méthode de l'état adjoint plutôt que des approximations par différences finies pour des problèmes d'optimisation correspondant à des évacuations de salles.

La modélisation des mouvements piétonniers est un champ de recherche fertile où de nombreuses améliorations restent à réaliser, depuis la validation des modèles existants à la création de nouvelles représentations intégrant plus de caractéristiques. En particulier, la capacité qu'a le piéton à prévoir, décider et se tromper est cruciale en optimisation et contrôle du trafic. Les modèles non-locaux en espace sont une représentation intéressante de la manière

dont les piétons assimilent l'information. On peut aller plus loin en intégrant un effet non-local en temps, comme un effet mémoire, pour décrire l'évolution du comportement des piétons dans les zones habituellement bloquées comme une attention accrue, ou une vitesse rabaissée. De plus, les modèles macroscopiques ont du mal à reproduire les phénomènes comme les *arches bloquantes*, l'effet *faster-is-slower* et le *paradoxe de Braess*. La validation est une étape critique pour renforcer la confiance dans les modèles macroscopiques. Par conséquent, beaucoup de travail reste pour développer un cadre consistant capable de traiter les lois de conservation non-classiques en vue d'une application générale au trafic piétonnier.

Appendix A

Proofs of technical lemmas

In this section are collected the necessary proofs to obtain Theorem 3.2.1. We follow closely [1].

Lemma A.0.1 *Let H, K and u^0 be positive. Define $u^{n+1} = (1+H)u^n + K$. Then*

$$u^n = (1+H)^n u^0 + \frac{(1+H)^n - 1}{H} K \leq (1+H)^n (u^0 + nK).$$

Proof u^{n+1} is defined as an arithmetic-geometric sequence, so

$$u^n = (1+H)^n (u^0 + K/H) - K/H = (1+H)^n u^0 + K \frac{(1+H)^n - 1}{H}.$$

By the binomial theorem and $\binom{n}{k} = \frac{n}{k}\binom{n-1}{k-1}$

$$\frac{(1+H)^n - 1}{H} = \frac{\left(\sum_{k=0}^{n} \binom{n}{k} H^k\right) - 1}{H} = \sum_{k=1}^{n} \binom{n}{k} H^{k-1} = \sum_{k=0}^{n-1} \binom{n}{k+1} H^k$$
$$= \sum_{k=0}^{n-1} \frac{n}{k+1} \binom{n-1}{k} H^k \leq \sum_{k=0}^{n-1} n \binom{n-1}{k} H^k = n(1+H)^{n-1} \leq n(1+H)^n$$

□

Lemma A.0.2 *Under condition* (H3), (3.6) *yields the estimates*

$$\begin{aligned}
\|A^n_{i+1,j} - A^n_{ij}\| &\leq \Delta x \|\partial_x \eta\|_{\mathbf{L}^\infty} \|u(t^n)\|_{\mathbf{L}^1}, \\
\|A^n_{i,j+1} - A^n_{ij}\| &\leq \Delta y \|\partial_y \eta\|_{\mathbf{L}^\infty} \|u(t^n)\|_{\mathbf{L}^1}, \\
\|A^n_{i+1,j} - 2A^n_{ij} + A^n_{i-1,j}\| &\leq \Delta x^2 \|\partial^2_{xx} \eta\|_{\mathbf{L}^\infty} \|u(t^n)\|_{\mathbf{L}^1}, \\
\|A^n_{i+1,j+1} - A^n_{i+1,j} - A^n_{i-1,j+1} - A^n_{i-1,j}\| &\leq 2\Delta x \Delta y \|\partial^2_{xy} \eta\|_{\mathbf{L}^\infty} \|u(t^n)\|_{\mathbf{L}^1}, \\
\|A^n_{i+2,j} - A^n_{i+1,j} - A^n_{ij} - A^n_{i-1,j}\| &\leq 2\Delta x^2 \|\partial^2_{xx} \eta\|_{\mathbf{L}^\infty} \|u(t^n)\|_{\mathbf{L}^1}.
\end{aligned}$$

Proof Consider the estimates on the A terms, the others being entirely similar.

$$\begin{aligned}
&\|A_{i+1,j} - A_{ij}\| \\
\leq &\Delta x \Delta y \sum_{l,m\in\mathbb{Z}} \|(\eta_{i-l+1,j-m} - \eta_{i-l,j-m}) u_\Delta(t^n, x_l, y_m)\| \\
\leq &\Delta x \Delta y \sum_{l,m\in\mathbb{Z}} \|\eta_{i-l+1,j-m} - \eta_{i-l,j-m}\| \|u_\Delta(t^n, x_l, y_m)\| \\
\leq &\Delta x \Delta y \sum_{l,m\in\mathbb{Z}} \|u_\Delta(t^n, x_l, y_m)\| \int_{x_{i-l}}^{x_{i+1-l}} \|\partial_x \eta(x, y_{j-m})\| dx \\
\leq &\Delta x \|\partial_x \eta\|_{\mathbf{L}^\infty} \|u_\Delta(t^n)\|_{\mathbf{L}^1},
\end{aligned}$$

proves the first estimate. Similarly with $\bar{x}_{i+1/2} \in]x_i, x_{i+1}[$,

$$\begin{aligned}
&\|A_{i+1,j} - 2A_{ij} + A_{i-1}\| \\
\leq &\Delta x \Delta y \sum_{l,m\in\mathbb{Z}} \|u_\Delta(t^n, x_l, y_m)\| \|\eta_{i+1-l,j-m} - 2\eta_{i-l,j-m} + \eta_{i-1-l,j-m}\| \\
\leq &\Delta x \Delta y \sum_{l,m\in\mathbb{Z}} \|u_\Delta(t^n, x_l, y_m)\| \Delta x \|\partial_x \eta(\bar{x}_{i+1/2-l}, y_{j-m}) - \partial_x \eta(\bar{x}_{i-1/2-l}, y_{j-m})\| \\
\leq &\Delta x \Delta y \sum_{l,m\in\mathbb{Z}} \|u_\Delta(t^n, x_l, y_m)\| \Delta x \int_{\bar{x}_{i-1/2-l}}^{\bar{x}_{i+1/2-l}} \|\partial^2_{xx} \eta(x, y_{j-m})\| dx \\
\leq &\Delta x^2 \|\partial^2_{xx} \eta\|_{\mathbf{L}^\infty} \|u_\Delta(t^n)\|_{\mathbf{L}^1},
\end{aligned}$$

and

$$\begin{aligned}
&\|A_{i+2,j} - A_{i+1,j} - A_{ij} + A_{i-1}\| \\
\leq &\Delta x \Delta y \sum_{l,m\in\mathbb{Z}} \|u_\Delta(t^n, x_l, y_m)\| \|\eta_{i+2-l,j-m} - \eta_{i+1-l,j-m} - \eta_{i-l,j-m} + \eta_{i-1-l,j-m}\| \\
\leq &\Delta x \Delta y \sum_{l,m\in\mathbb{Z}} \|u_\Delta(t^n, x_l, y_m)\| \Delta x \|\partial_x \eta(\bar{x}_{i+3/2-l}, y_{j-m}) - \partial_x \eta(\bar{x}_{i-1/2-l}, y_{j-m})\| \\
\leq &\Delta x \Delta y \sum_{l,m\in\mathbb{Z}} \|u_\Delta(t^n, x_l, y_m)\| \Delta x \int_{\bar{x}_{i-1/2-l}}^{\bar{x}_{i+3/2-l}} \|\partial^2_{xx} \eta(x, y_{j-m})\| dx \\
\leq &2\Delta x^2 \|\partial^2_{xx} \eta\|_{\mathbf{L}^\infty} \|u_\Delta(t^n)\|_{\mathbf{L}^1}.
\end{aligned}$$

□

Proof of Lemma 3.2.2 We want to rewrite (3.5) as a convex combination of $u_{i-1,j}, u_{ij}, u_{i+1,j}$ (we drop the k index):

$$\begin{aligned}
u_{ij}^{n+1/2} = u_{ij}^n \quad &-a^n_{i-1/2,j}(u^n_{ij} - u^n_{i-1,j}) + b^n_{i+1/2,j}(u^n_{i+1,j} - u^n_{ij}) \\
&-\lambda_x \left(F^n_{i+1/2,j}(u^n_{ij}, u^n_{ij}) - F^n_{i-1/2,j}(u^n_{ij}, u^n_{ij}) \right),
\end{aligned} \tag{A.1}$$

where $a^n_{i-1/2,j}$ and $b^n_{i+1/2,j}$ are

$$a^n_{i-1/2,j} = \lambda_x \frac{F^n_{i-1/2,j}(u^n_{ij}, u^n_{ij}) - F^n_{i-1/2,j}(u^n_{i-1,j}, u^n_{ij})}{u^n_{ij} - u^n_{i-1,j}},$$
$$b^n_{i+1/2,j} = \lambda_x \frac{F^n_{i+1/2,j}(u^n_{ij}, u^n_{ij}) - F^n_{i+1/2,j}(u^n_{i-1,j}, u^n_{ij})}{u^n_{i+1,j} - u^n_{ij}}.$$

We prove that $a^n_{i-1/2,j}$ and $b^n_{i+1/2,j}$ are nonnegative. Indeed,

$$\begin{aligned} a^n_{i-1/2,j} &= \lambda_x \tfrac{F^n_{i-1/2,j}(u^n_{ij},u^n_{ij}) - F^n_{i-1/2,j}(u^n_{i-1,j},u^n_{ij})}{u^n_{ij}-u^n_{i-1,j}} \\ &= \tfrac{\lambda_x}{u^n_{ij}-u^n_{i-1,j}} \left(\tfrac{f^n_{i-1,j}(u_{ij}) + f^n_{ij}(u_{ij})}{2} - \tfrac{f^n_{i-1,j}(u_{ij}) + f^n_{ij}(u_{i-1,j})}{2} \right) + \tfrac{\alpha}{2} \\ &= \tfrac{\lambda_x}{u^n_{ij}-u^n_{i-1,j}} \left(\tfrac{f^n_{ij}(u_{ij}) - f^n_{ij}(u_{i-1,j})}{2} \right) + \tfrac{\alpha}{2} \\ &= \tfrac{\lambda_x \partial_u f^n_{ij}(\bar{u}^n_{i-1/2,j}) + \alpha}{2} \end{aligned}$$

for a suitable $\bar{u}^n_{i-1/2,j}$ lying between $u^n_{i-1,j}$ and u^n_{ij}. We use a similar procedure to demonstrate $b^n_{i+1/2,j}$ nonnegativity.
Hence by (3.7)

$$a^n_{i-1/2,j} \geq \tfrac{-\lambda_x \|\partial_u f^k\|_{\mathbf{L}^\infty} + \alpha}{2} \geq 0, \quad a^n_{i-1/2,j} \leq \tfrac{\lambda_x \|\partial_u f^k\|_{\mathbf{L}^\infty} + \alpha}{2} \leq \tfrac{1}{3}. \tag{A.2}$$

Remark λ_x satisfies

$$\lambda_x \leq \frac{\max\{\alpha, 2/3 - \alpha\}}{\|\partial_u f^k\|_{\mathbf{L}^\infty}}.$$

Similar computations hold for $b^n_{i+1/2,j}$. Then $1 - a^n_{i-1/2,j} - b^n_{i-1/2,j}$, $a^n_{i-1/2,j}$ and $b^n_{i+1/2,j}$ are coefficients of a convex combination. We want to bound the last term in (A.1). Using (H0), (H1) and (3.7) and $u^n_{ij} \geq 0$,

$$\begin{aligned} &\left| F^n_{i+1/2,j}(u^n_{ij}, u^n_{ij}) - F^n_{i-1/2,j}(u^n_{ij}, u^n_{ij}) \right| \\ =&\frac{1}{2} \left| f^k(t^n, x_{i+1}, y_j, u^n_{ij}, A^n_{i+1,j}) - f^k(t^n, x_{i-1}, y_j, u^n_{ij}, A^n_{i-1,j}) \right. \\ &\left. + f^k(t^n, x_{i+1}, y_j, u^n_{ij}, A^n_{i-1,j}) - f^k(t^n, x_{i+1}, y_j, u^n_{ij}, A^n_{i-1,j}) \right| \\ \leq&\frac{1}{2} \left| f^k(t^n, x_{i+1}, y_j, u^n_{ij}, A^n_{i+1,j}) \right| + \left| f^k(t^n, x_{i+1}, y_j, u^n_{ij}, A^n_{i-1,j}) \right| \\ &+ \left| f^k(t^n, x_{i+1}, y_j, u^n_{ij}, A^n_{i-1,j}) - f^k(t^n, x_{i-1}, y_j, u^n_{ij}, A^n_{i-1,j}) \right| \\ \leq&u^n_{ij} \|\partial_u f\|_{\mathbf{L}^\infty} + \frac{1}{2} \left| f^k(t^n, x_{i+1}, y_j, u^n_{ij}, A^n_{i-1,j}) - f^k(t^n, x_{i-1}, y_j, u^n_{ij}, A^n_{i-1,j}) \right|. \end{aligned}$$

So there exists $\bar{x}_i$ between x_{i-1} and x_{i+1} such that

$$\begin{aligned} &\left| F^n_{i+1/2,j}(u^n_{ij}, u^n_{ij}) - F^n_{i-1/2,j}(u^n_{ij}, u^n_{ij}) \right| \\ \leq&u^n_{ij} \|\partial_u f\|_{\mathbf{L}^\infty} + \Delta x \left| \partial_x f(t^n, \bar{x}_i, y_j, u^n_{ij}, A_{i-1,j}) \right| \\ \leq&u^n_{ij} \|\partial_u f\|_{\mathbf{L}^\infty} + \Delta x M u^n_{ij} \\ \leq&u^n_{ij} \left(\|\partial_u f\|_{\mathbf{L}^\infty} + \frac{1}{3} \right). \end{aligned}$$

Now using condition (3.7) we have

$$\left|F^n_{i+1/2,j}(u^n_{ij},u^n_{ij})-F^n_{i-1/2,j}(u^n_{ij},u^n_{ij})\right|\leq \tfrac{1}{3\lambda_x}u^n_{ij}. \tag{A.3}$$

Using (A.2) and (A.3) in (A.1) we get

$$\begin{aligned}u^{n+1/2}_{ij}=&(1-a^n_{i-1/2,j}-b^n_{i+1/2,j})u^n_{ij}+a^n_{i-1/2,j}u^n_{i-1,j}+b^n_{i+1/2,j}u^n_{i+1,j}\\&-\lambda_x\left(F^n_{i+1/2,j}(u^n_{ij},u^n_{ij})-F^n_{i-1/2,j}(u^n_{i,j},u^n_{ij})\right)\\\geq&\left(\frac{2}{3}-a^n_{i-1/2,j}-b^n_{i+1/2,j}\right)u^n_{ij}+a^n_{i-1/2,j}u^n_{i-1,j}+b^n_{i+1/2,j}u^n_{i+1,j}\geq 0.\end{aligned}$$

□

Proof of Lemma 3.2.4 Use (A.0.2) and (H1) in (A.1) and $f^n_{rs}(u_{ij})=f(t^n,x_r,y_s,u_{ij},A^n_{rs})$ to obtain:

$$\begin{aligned}&\left|F^n_{i+1/2,j}(u_{ij},u_{ij})-F^n_{i-1/2,j}(u_{ij},u_{ij})\right|=\left|\frac{f^n_{i+1,j}(u_{ij})-f^n_{i-1,j}(u_{ij})}{2}\right|\\\leq&\frac{1}{2}\left[2\Delta x|\partial_x f(t^n,\bar{x}_i,y_j,u_{ij},\bar{A}^n_{ij})|\right.\\&\left.+\left(\|A^n_{i+1,j}-A^n_{ij}\|+\|A^n_{ij}-A^n_{i-1,j}\|\right)\|\nabla_A f(t^n,\bar{x}_i,y_j,u_{ij},\bar{A}^n_{ij})\|\right]\\\leq&\frac{1}{2}\left[2\Delta xMu_{ij}+2\Delta x\|\partial_x\eta\|_{\mathbf{L}^\infty}\|u_\Delta(t^n)\|_{\mathbf{L^1}}Mu_{ij}\right]\\\leq&\Delta xMu_{ij}\left(\|\partial_x\eta\|_{\mathbf{L}^\infty}\|u_\Delta(t^n)\|_{\mathbf{L^1}}+1\right),\end{aligned} \tag{A.4}$$

with $\bar{x}_i\in I(x_{i-1},x_{i+1})$ and $\bar{A}^n_{ij}\in I(A^n_{i-1,j},A^n_{i+1,j})$.
Now using Lemma 3.2.3, (A.2) and (A.4), we get

$$\begin{aligned}u^{n+1/2}_{ij}\leq&(1-a^n_{i-1/2,j}-b^n_{i+1/2,j})u^n_{ij}+a^n_{i-1/2,j}u^n_{i-1,j}\\&+b^n_{i+1/2,j}u^n_{i+1,j}+Mu_{ij}\Delta t(\|\partial_x\eta\|_{\mathbf{L}^\infty}\|u_\Delta(t^n)\|_{\mathbf{L^1}}+1)\\&\leq(1-a^n_{i-1/2,j}-b^n_{i+1/2,j})\|u^n_\Delta(t^n)\|_{\mathbf{L}^\infty}+a^n_{i-1/2,j}\|u^n_\Delta(t^n)\|_{\mathbf{L}^\infty}\\&+b^n_{i+1/2,j}\|u^n_\Delta(t^n)\|_{\mathbf{L}^\infty}+M\|u^n_\Delta(t^n)\|_{\mathbf{L}^\infty}\Delta t(\|\partial_x\eta\|_{\mathbf{L}^\infty}\|u_\Delta(0)\|_{\mathbf{L^1}}+1)\\&\leq\|u_\Delta(t^n)\|_{\mathbf{L}^\infty}(1+M\Delta t(\|\partial_x\eta\|_{\mathbf{L}^\infty}\|U^0\|_{\mathbf{L^1}}+1)),\end{aligned}$$

which is true for all i, j, therefore

$$\|u_\Delta(t^{n+1/2})\|_{\mathbf{L}^\infty}\leq(1+M(\|\partial_x\eta\|_{\mathbf{L}^\infty}\|U^0\|_{\mathbf{L^1}}+1)\Delta t)\|u_\Delta(t^n)\|_{\mathbf{L}^\infty}.$$

Applying the same procedure for the y component gives

$$\|u_\Delta(t^{n+1})\|_{\mathbf{L}^\infty}\leq(1+M(\|\partial_y\theta\|_{\mathbf{L}^\infty}\|U^0\|_{\mathbf{L^1}}+1)\Delta t)\|u_\Delta(t^{n+1/2})\|_{\mathbf{L}^\infty},$$

and by Lemma (A.0.1) we have the $\mathbf{L}^\infty$ bound

$$\|u_\Delta(t^n)\|_{\mathbf{L}^\infty}\leq\|U^0\|_{\mathbf{L}^\infty}[1+M(\max\{\|\partial_x\eta\|_{\mathbf{L}^\infty}\|,\|\partial_y\theta\|_{\mathbf{L}^\infty}\}\|U^0\|_{\mathbf{L^1}}+1)\Delta t]^{2n}.$$

Remarking that $\Delta t = \frac{t}{n}$ and passing to the limit yields:

$$\lim_{n\to+\infty}\left[1 + M(\max\{\|\partial_x\eta\|_{\mathbf{L}^\infty}\|, \|\partial_y\theta\|_{\mathbf{L}^\infty}\}\|U^0\|_{\mathbf{L^1}} + 1)\frac{t}{n}\right]^{2n}$$
$$= e^{2tM(\max\{\|\partial_x\eta\|_{\mathbf{L}^\infty},\|\partial_y\theta\|_{\mathbf{L}^\infty}\}\|U^0\|_{\mathbf{L^1}}+1)}.$$

We have

$$\max\{\|\partial_x\eta\|_{\mathbf{L}^\infty}, \|\partial_y\theta\|_{\mathbf{L}^\infty}\}\|U^0\|_{\mathbf{L^1}} + 1$$
$$\leq (1 + \|U^0\|_{L^1})(1 + \max\{\|\partial_x\eta\|_{\mathbf{L}^\infty}\|, \|\partial_y\theta\|_{\mathbf{L}^\infty}\},$$

therefore the estimate in Lemma 3.2.4 holds with

$$\mathcal{C} = 2M(1 + \max\{\|\partial_x\eta\|_{\mathbf{L}^\infty}\|, \|\partial_y\theta\|_{\mathbf{L}^\infty}\}). \tag{A.5}$$

□

Proof of Lemma 3.2.5 Consider first the term $\sum_{ij}\left|u_{i+1,j}^{n+1/2} - u_{ij}^{n+1/2}\right|\Delta y$ and set $u_{i+1,j}^{n+1/2} - u_{ij}^{n+1/2} = C_{ij}^n + \lambda_x D_{ij}^n$, where

$$\begin{aligned}
C_{ij}^n &= (u_{i+1,j}^n - u_{ij}^n) - \lambda_x\left(F_{i+3/2,j}^n(u_{i+1,j}^n, u_{i+2,j}^n) - F_{i+1/2,j}^n(u_{ij}^n - u_{i+1,j}^n)\right)\\
&\qquad -\lambda_x\left(-F_{i+3/2,j}^n(u_{ij}^n, u_{i+1,j}^n) + F_{i+1/2,j}(u_{i-1,j}^n, u_{ij}^n)\right),\\
D_{ij}^n &= -F_{i+3/2,j}^n(u_{ij}^n, u_{i+1,j}^n) + F_{i+1/2}^n(u_{ij}^n, u_{i+1,j}^n)\\
&\quad -F_{i-1/2,j}^n(u_{i-1,j}^n, u_{ij}^n) + F_{i+1/2,j}^n(u_{i-1,j}^n, u_{ij}^n).
\end{aligned}$$

We estimate the various terms above separately. Consider the term C_{ij}^n (and drop the n)

$$\begin{aligned}
C_{ij}^n =&(u_{i+1,j} - u_{ij})\left(1 + \lambda_x\frac{F_{i+1/2,j}(u_{ij}, u_{i+1,j}) - F_{i+1/2,j}(u_{ij}, u_{ij})}{u_{i+1,j} - u_{ij}}\right)\\
&+ (u_{i+1,j} - u_{ij})\left(-\lambda_x\frac{F_{i+3/2,j}(u_{i+1,j}, u_{i+1,j}) - F_{i+3/2,j}(u_{ij}, u_{i+1,j})}{u_{i+1} - u_i}\right)\\
&+ (u_{i+2,j} - u_{i+1,j})\left(-\lambda_x\frac{F_{i+3/2,j}(u_{i+1,j}, u_{i+2,j}) - F_{i+3/2,j}(u_{i+1,j}, u_{i+1,j})}{u_{i+2} - u_{i+1}}\right)\\
&+ (u_{ij} - u_{i-1,j})\left(\lambda_x\frac{F_{i+1/2,j}(u_{ij}, u_{ij}) - F_{i+1/2,j}(u_{i-1,j}, u_{ij})}{u_{ij} - u_{i-1,j}}\right)\\
=&(u_{i+1,j} - u_{ij})(1 - b_{i+1/2,j} - \hat{a}_{i+1/2,j})\\
&+ (u_{i+2,j} - u_{i+1,j})b_{i+3/2,j} + (u_{ij}^n - u_{i-1,j})\hat{a}_{i-1/2,j},
\end{aligned}$$

where $\hat{a}_{i-1/2,j} = \lambda_x \frac{F_{i+1/2,j}(u_{ij},u_{ij}) - F_{i+1/2,j}(u_{i-1,j},u_{ij})}{u_{ij}-u_{i-1,j}}$ and $\hat{a}_{i-1/2,j} \in [0,1/3]$ can be proven exactly as was done for $a_{i-1/2,j}$. By convexity, we have

$$\begin{aligned}
&\sum_{ij} |C_{ij}^n| \Delta y \\
&\quad \leq \Delta y \sum_{ij} |u_{i+1,j} - u_{ij}| (1 - b_{i+1/2,j} - \hat{a}_{i+1/2,j}) \\
&\qquad + |u_{i+2,j} - u_{i+1,j}| b_{i+3/2,j} + |u_{ij} - u_{i-1,j}| \hat{a}_{i-1/2,j} \\
&\quad = \sum_{ij} |u_{i+1,j} - u_{ij}| \, \Delta y. \qquad \text{(A.6)}
\end{aligned}$$

Concerning D_{ij}^n (we drop the n)

$$\begin{aligned}
D_{ij}^n &= -\frac{1}{2} \left[f_{i+2,j}(u_{i+1,j}) - f_{i+1,j}(u_{i+1,j}) - (f_{ij}(u_{i-1,j}) - f_{i-1,j}(u_{i-1,j})) \right] \\
&= -\frac{1}{2} \big[\Delta x \partial_x f(t^n, \bar{x}_{i+1/2,j}, y_j, u_{i+1,j}, \bar{A}_{i+1/2,j}) \\
&\quad + (A_{i+2,j} - A_{i+1,j}) \nabla_A f(t^n, \bar{x}_{i+1/2,j}, y_j, u_{i+1,j}, \bar{A}_{i+1/2,j}) \\
&\quad - \Delta x \partial_x f(t^n, \bar{x}_{i-1/2,j}, y_j, u_{i-1,j}, \bar{A}_{i-1/2,j}) \\
&\quad - (A_{ij} - A_{i-1,j}) \nabla_A f(t^n, \bar{x}_{i-1/2,j}, y_j, u_{i-1,j}, \bar{A}_{i-1/2,j}) \big] \\
&= -\frac{\Delta x}{2} \Big[(\bar{x}_{i+1/2} - \bar{x}_{i-1/2}) \partial_{xx} f(t^n, \bar{\bar{x}}_i, y_j, \bar{u}_{ij}, \bar{\bar{A}}_{ij}) \\
&\quad + (u_{i+1,j} - u_{i-1,j}) \partial_u \partial_x f(t^n, \bar{\bar{x}}_i, y_j, \bar{u}_{ij}, \bar{\bar{A}}_{ij}) \\
&\quad - (\bar{A}_{i+1/2} - \bar{A}_{i-1/2}) \nabla_A \partial_x f(t^n, \bar{\bar{x}}_{ij}, y_j, \bar{u}_{ij}, \bar{\bar{A}}_{ij}) \Big] \\
&\quad + \frac{1}{2} \Big[(x_{i+1/2} - x_{i-1/2}) \overline{\Delta A}_{i+1/2,j} \partial_x \nabla_A f(t^n, \bar{\bar{x}}'_i, y_j, \bar{u}'_{ij}, \bar{\bar{A}}'_{ij}) \\
&\quad + (u_{i+1} - u_{i-1}) \overline{\Delta A}_{i+1/2,j} \partial_u \nabla_A f(t^n, \bar{\bar{x}}'_i, y_j, \bar{u}'_{ij}, \bar{\bar{A}}'_{ij}) \\
&\quad + (\bar{A}_{i+1/2,j} - \bar{A}_{i-1/2,j}) \overline{\Delta A}_{i+1/2,j} \nabla^2_{AA} f(t^n, \bar{\bar{x}}'_i, y_j, \bar{u}'_{ij}, \bar{\bar{A}}'_{ij}) \\
&\quad + (A_{i+2,j} - A_{i+1,j} - A_{ij} + A_{i-1,j}) \nabla_A f(t^n, \bar{\bar{x}}'_i, y_j, \bar{u}'_{ij}, \bar{\bar{A}}'_{ij}) \Big],
\end{aligned}$$

with suitable $\bar{x}_{i+1/2} \in I(x_i, x_{i+1})$, $\bar{A}_{i+1/2,j} \in I(A_{ij}, A_{i+1,j})$, $\bar{\bar{x}}_i, \bar{\bar{x}}'_i \in I(\bar{x}_{i-1/2}, \bar{x}_{i+1/2})$ and $\bar{\bar{A}}_{ij}, \bar{\bar{A}}'_{ij} \in I(\bar{A}_{i-1/2,j}, \bar{A}_{i+1/2,j})$.
Therefore,

$$\begin{aligned}
|D_{ij}^n| \leq &\frac{1}{2} \Delta x^2 M |\bar{u}_{ij}| \left(1 + \|\partial_x \eta\|_{\mathbf{L}^\infty} \|u_\Delta(t^n)\|_{\mathbf{L}^1}\right) \\
&+ \frac{1}{2} \Delta x^2 M |\bar{u}'_{ij}| \big(\|\partial_x \eta\|_{\mathbf{L}^\infty} \|u_\Delta(t^n)\|_{\mathbf{L}^1} + (\|\partial_x \eta\|_{\mathbf{L}^\infty} \|u_\Delta(t^n)\|_{\mathbf{L}^1})^2 \\
&+ 2\|\partial^2_{xx} \eta\|_{\mathbf{L}^\infty} \|u_\Delta(t^n)\|_{\mathbf{L}^1} \big) \\
&+ \frac{1}{2} \Delta x |u_{i+1,j} - u_{i-1,j}| \left(\|\partial_u \partial_x f\|_{\mathbf{L}^\infty} + |\partial_u \nabla_A f\|_{\mathbf{L}^\infty} \|\partial_x \eta\|_{\mathbf{L}^\infty} \|u_\Delta(t^n)\|_{\mathbf{L}^1} \right),
\end{aligned}$$

and

$$
\begin{aligned}
\sum_{ij} \lambda_x |D_{ij}^n| \Delta y \leq & \sum_{ij} \frac{\Delta t}{2} \Delta x \Delta y M |\bar{u}_{ij}| \left(1 + \|\partial_x \eta\|_{\mathbf{L}^\infty} \|u_\Delta(t^n)\|_{\mathbf{L}^1}\right) \\
& + \sum_{ij} \frac{\Delta t}{2} \Delta x \Delta y M |\bar{u}'_{ij}| \left(\|\partial_x \eta\|_{\mathbf{L}^\infty} \|u_\Delta(t^n)\|_{\mathbf{L}^1}\right. \\
& \left. + (\|\partial_x \eta\|_{\mathbf{L}^\infty} \|u_\Delta(t^n)\|_{\mathbf{L}^1})^2 + 2\|\partial_{xx}^2 \eta\|_{\mathbf{L}^\infty} \|u_\Delta(t^n)\|_{\mathbf{L}^1}\right) \\
& + \sum_{ij} \frac{\Delta t}{2} \Delta y |u_{i+1,j} - u_{i-1,j}| \left(\|\partial_u \partial_x f\|_{\mathbf{L}^\infty}\right. \\
& \left. + \|\partial_u \nabla_A f\|_{\mathbf{L}^\infty} \|\partial_x \eta\|_{\mathbf{L}^\infty} \|u_\Delta(t^n)\|_{\mathbf{L}^1}\right) \\
\leq & \Delta t M \|u_\Delta(t^n)\|_{\mathbf{L}^1} \left(1 + 2\|\partial_x \eta\|_{\mathbf{L}^\infty} \|u_\Delta(t^n)\|_{\mathbf{L}^1}\right. \\
& \left. + (\|\partial_x \eta\|_{\mathbf{L}^\infty} \|u_\Delta(t^n)\|_{\mathbf{L}^1})^2 + 2\|\partial_{xx}^2 \eta\|_{\mathbf{L}^\infty} \|u_\Delta(t^n)\|_{\mathbf{L}^1}\right) \\
& + \Delta t \left(\|\partial_u \partial_x f\|_{\mathbf{L}^\infty}\right. \\
& \left. + |\partial_u \nabla_A f\|_{\mathbf{L}^\infty} \|\partial_x \eta\|_{\mathbf{L}^\infty} \|u_\Delta(t^n)\|_{\mathbf{L}^1}\right) \sum_{ij} |u_{i+1,j} - u_{ij}| \Delta y \\
\leq & K_0 \Delta t + K_1 \Delta t \sum_{ij} |u_{i+1,j} - u_{ij}| \, \Delta y.
\end{aligned}
$$

Adding (A.6) to the expression above, we get

$$
\sum_{ij} \left| u_{i+1,j}^{n+1/2} - u_{ij}^{n+1/2} \right| \Delta y \leq K_0 \Delta t + (1 + K_1 \Delta t) \sum_{ij} \left| u_{i+1,j}^n - u_{ij}^n \right| \Delta y.
$$

Now we pass to $\sum_{ij} |u_{i,j+1}^{n+1/2} - u_{ij}^{n+1/2}| \Delta x$, setting

$$
\begin{aligned}
& u_{i,j+1}^{n+1/2} - u_{ij}^{n+1/2} \\
= & u_{i,j+1}^n - u_{ij}^n - \lambda_x \Big[F_{i+1/2,j+1}^n (u_{i,j+1}^n, u_{i+1,j+1}^n) - F_{i-1/2,j+1}^n (u_{i-1,j+1}^n, u_{i,j+1}^n) \\
& - F_{i+1/2,j}^n (u_{ij}^n, u_{i+1,j}^n) + F_{i-1/2,j}^n (u_{i-1,j}^n, u_{ij}^n) \\
& + F_{i+1/2,j+1}^n (u_{ij}, u_{i+1,j}) - F_{i+1/2,j+1}^n (u_{ij}, u_{i+1,j}) \\
& + F_{i-1/2,j+1}^n (u_{i-1,j}, u_{i,j}) - F_{i-1/2,j+1}^n (u_{i-1,j}, u_{i,j}) \Big] \\
= & \tilde{C}_{ij}^n + \lambda_x \tilde{D}_{ij}^n,
\end{aligned}
$$

where (we drop the index n)

$$
\begin{aligned}
\tilde{C}_{ij}^n = & u_{i,j+1} - u_{ij} \\
& - \lambda_x \left[F_{i+1/2,j+1}(u_{i,j+1}, u_{i+1,j+1}) - F_{i+1/2,j+1}(u_{ij}, u_{i+1,j}) \right. \\
& \left. + F_{i-1/2,j+1}(u_{i-1,j}, u_{ij}) - F_{i-1/2,j+1}(u_{i-1,j+1}, u_{i,j+1}) \right], \\
\tilde{D}_{ij}^n = & F_{i+1/2,j}(u_{ij}, u_{i+1,j}) - F_{i+1/2,j+1}(u_{ij}, u_{i+1,j}) \\
& + F_{i-1/2,j+1}(u_{i-1,j}, u_{ij}) - F_{i-1/2,j}(u_{i-1,j}, u_{ij}).
\end{aligned}
$$

Following the same treatment of C_{ij}^n, we obtain:

$$\begin{aligned}
\tilde{C}_{ij}^n &= (u_{i,j+1} - u_{ij}) \left(1 - \lambda_x \frac{F_{i+1/2,j+1}(u_{i,j+1}, u_{i+1,j+1}) - F_{i+1/2,j+1}(u_{i,j}, u_{i+1,j+1})}{u_{i,j+1} - u_{ij}}\right) \\
&-\lambda_x (u_{i+1,j+1} - u_{i+1,j}) \frac{F_{i+1/2,j+1}(u_{i,j}, u_{i+1,j+1}) - F_{i+1/2,j+1}(u_{i,j}, u_{i+1,j})}{u_{i+1,j+1} - u_{i+1,j}} \\
&-\lambda_x (u_{i,j+1} - u_{ij}) \frac{F_{i-1/2,j+1}(u_{i-1,j}, u_{i,j}) - F_{i-1/2,j+1}(u_{i-1,j}, u_{i,j+1})}{u_{i,j+1} - u_{ij}} \\
&-\lambda_x (u_{i-1,j+1} - u_{i-1,j}) \frac{F_{i-1/2,j+1}(u_{i-1,j}, u_{i,j+1}) - F_{i-1/2,j+1}(u_{i-1,j+1}, u_{i,j+1})}{u_{i-1,j+1} - u_{i-1,j}} \\
&= (u_{i,j+1} - u_{ij})(1 - a_{i+1/2,j+1} - b_{i-1/2,j+1}) + a_{i-1/2,j+1}(u_{i-1,j+1} - u_{i-1,j}) \\
&+b_{i+1/2,j+1}(u_{i+1,j+1} - u_{i+1,j}),
\end{aligned}$$

where

$$\begin{aligned}
a_{i+1/2,j+1} &= -\lambda_x \frac{F_{i+1/2,j+1}(u_{i,j+1}, u_{i+1,j+1}) - F_{i+1/2,j+1}(u_{i,j}, u_{i+1,j+1})}{u_{i,j+1} - u_{ij}}, \\
b_{i-1/2,j+1} &= -\lambda_x \frac{F_{i-1/2,j+1}(u_{i-1,j}, u_{i,j+1}) - F_{i-1/2,j+1}(u_{i-1,j}, u_{i,j})}{u_{i,j+1} - u_{ij}}.
\end{aligned}$$

As in C_{ij}^n, (3.7) implies that $a_{i+1/2,j+1}$, $b_{i-1/2,j+1} \in [0, 1/3]$ for all i, j and

$$\sum_{ij} \tilde{C}_{ij}^n \leq \sum_{ij} |u_{i,j+1} - u_{ij}|, \tag{A.7}$$

by convexity. Passing to $\tilde{D}_{ij}^n$, we have:

$$\begin{aligned}
\tilde{D}_{ij}^n =& F_{i+1/2,j}(u_{ij}, u_{i+1,j}) - F_{i+1/2,j+1}(u_{ij}, u_{i+1,j}) \\
&+ F_{i-1/2,j+1}(u_{i-1,j}, u_{ij}) - F_{i-1/2,j}(u_{i-1,j}, u_{ij}) \\
=& \frac{1}{2} \left[f_{i+1,j}(u_{i+1,j}) - f_{i+1,j+1}(u_{i+1,j}) \right. \\
&\left. - \left(f_{i-1,j}(u_{i-1,j}) - f_{i-1,j+1}(u_{i-1,j}) \right) \right] \\
=& \frac{1}{2} \left[\Delta y \partial_y f(t^n, x_{i+1}, \bar{y}_{j+1/2}, u_{i+1,j}, \bar{A}_{i+1,j+1/2}) \right. \\
&+ (A_{i+1,j+1} - A_{i+1,j}) \nabla_A f(t^n, x_{i+1}, \bar{y}_{j+1/2}, u_{i+1,j}, \bar{A}_{i+1,j+1/2}) \\
&- \Delta y \partial_y f(t^n, x_{i-1}, \bar{y}'_{j+1/2}, u_{i-1,j}, \bar{A}_{i-1,j+1/2}) \\
&\left. - (A_{i-1,j+1} - A_{i-1,j}) \nabla_A f(t^n, x_{i-1}, \bar{y}'_{j+1/2}, u_{i-1,j}, \bar{A}_{i-1,j+1/2}) \right],
\end{aligned}$$

with $\bar{y}_{j+1/2} \in [y_j, y_{j+1}]$ and $\bar{A}_{i+1,j+1/2} \in I(A_{i+1,j}, A_{i+1,j+1})$ on $(y, A_1, A_2) \mapsto f(t^n, x, y, u, A_1) - f(t^n, x, y, u, A_2)$.

Introducing suitable $\bar{x}_i,\ \bar{x}'_i \in [x_{i-1}, x_{i+1}],\ \bar{u}_{ij},\ \bar{u}'_{ij} \in I(u_{i-1,j}, u_{i+1,j}),\ \bar{\bar{A}}_{i,j+1/2},\ \bar{\bar{A}}'_{i,j+1/2} \in I(\bar{A}_{i-1,j+1/2}, \bar{A}_{i+1,j+1/2})$ and $\overline{\Delta A} \in I(A_{i-1,j+1} - A_{i-1,j}, A_{i+1,j+1} - A_{i+1,j})$, we have

$$
\begin{aligned}
&\frac{\Delta y}{2}\left[\partial_y f(t^n, x_{i+1}, \bar{y}_{j+1/2}, u_{i+1,j}, \bar{A}_{i+1,j+1/2})\right.\\
&\left.- \partial_y f(t^n, x_{i-1}, \bar{y}_{j+1/2}, u_{i-1,j}, \bar{A}_{i-1,j+1/2})\right]\\
&+ \frac{1}{2}\left[(A_{i+1,j+1} - A_{i+1,j})\nabla_A f(t^n, x_{i+1}, \bar{y}_{j+1/2}, u_{i+1,j}, \bar{A}_{i+1,j+1/2})\right.\\
&\left.- (A_{i-1,j+1} - A_{i-1,j})\nabla_A f(t^n, x_{i-1}, \bar{y}_{j+1/2}, u_{i-1,j}, \bar{A}_{i-1,j+1/2})\right]\\
=&\frac{\Delta y}{2}\Big[2\Delta x \partial_x \partial_y f(t^n, \bar{x}_i, \bar{y}_{j+1/2}, \bar{u}_{ij}, \bar{\bar{A}}_{i,j+1/2})\\
&+ (u_{i+1,j} - u_{i-1,j})\partial_u \partial_y f(t^n, \bar{x}_i, \bar{y}_{j+1/2}, \bar{u}_{ij}, \bar{\bar{A}}_{i,j+1/2})\\
&+ (\bar{A}_{i+1,j+1/2} - \bar{A}_{i-1,j+1/2})\nabla_A \partial_y f(t^n, \bar{x}_i, \bar{y}_{j+1/2}, \bar{u}_{ij}, \bar{\bar{A}}_{i,j+1/2})\Big]\\
&+ \frac{1}{2}\Big[2\Delta x \overline{\Delta A}\partial_x \nabla_A f(t^n, \bar{x}'_i, \bar{y}_{j+1/2}, \bar{u}'_{ij}, \bar{\bar{A}}'_{i,j+1/2})\\
&+ (u_{i+1,j} - u_{i-1,j})\overline{\Delta A}\partial_u \nabla_A f(t^n, \bar{x}'_i, \bar{y}_{j+1/2}, \bar{u}'_{ij}, \bar{\bar{A}}'_{i,j+1/2})\\
&+ (\bar{A}_{i+1,j+1/2} - \bar{A}_{i-1,j+1/2})\overline{\Delta A}\nabla^2_{AA} f(t^n, \bar{x}'_i, \bar{y}_{j+1/2}, \bar{u}'_{ij}, \bar{\bar{A}}'_{i,j+1/2})\\
&+ (A_{i+1,j+1} - A_{i+1,j} - A_{i-1,j+1} + A_{i-1,j})\nabla_A f(t^n, \bar{x}'_i, \bar{y}_{j+1/2}, \bar{u}'_{ij}, \bar{\bar{A}}'_{i,j+1/2})\Big].
\end{aligned}
$$

We bound it using (H1) and Lemma A.0.2

$$
\begin{aligned}
|A.8| \leq&\frac{\Delta y}{2}\left[2\Delta x M|\bar{u}_{ij}| + |u_{i+1,j} - u_{i-1,j}|\|\partial_u \partial_y f\|_{\mathbf{L}^\infty} + 2\Delta x M|\bar{u}_{ij}|\|\partial_x \eta\|_{\mathbf{L}^\infty}\|u_\Delta(t^n)\|_{\mathbf{L^1}}\right]\\
&+ \frac{1}{2}\Big[2\Delta x \Delta y M|\bar{u}'_{ij}|\|\partial_y \eta\|_{\mathbf{L}^\infty}\|u_\Delta(t^n)\|_{\mathbf{L^1}}\\
&+ \Delta y|u_{i+1,j} - u_{i-1,j}|\|\partial_y \eta\|_{\mathbf{L}^\infty}\|u_\Delta(t^n)\|_{\mathbf{L^1}}\|\partial_u \nabla_A f\|\\
&+ 2\Delta x \Delta y M|\bar{u}'_{ij}|\|\partial_x \eta\|_{\mathbf{L}^\infty}\|\partial_y \eta\|_{\mathbf{L}^\infty}\|u_\Delta(t^n)\|^2_{\mathbf{L^1}} + 2\Delta x \Delta y M|\bar{u}'_{ij}|\|\partial^2_{x,y}\eta\|\|u_\Delta(t^n)\|_{\mathbf{L^1}}\Big]\\
\leq&\Delta x \Delta y M|\bar{u}_{ij}|\left[1 + \|\partial_x \eta\|_{\mathbf{L}^\infty}\|u_\Delta(t^n)\|_{\mathbf{L^1}}\right]\\
&+ \frac{\Delta y}{2}|u_{i+1,j} - u_{i-1,j}|\left[\|\partial_u \partial_y f\|_{\mathbf{L}^\infty} + \|\partial_y \eta\|_{\mathbf{L}^\infty}\|u_\Delta(t^n)\|_{\mathbf{L^1}}\|\partial_u \nabla_A f\|_{\mathbf{L}^\infty}\right]\\
&+ \Delta x \Delta y M|\bar{u}'_{ij}|\Big[\|\partial_y \eta\|_{\mathbf{L}^\infty}\|u_\Delta(t^n)\| + \|\partial_x \eta\|_{\mathbf{L}^\infty}\|\partial_y \eta\|_{\mathbf{L}^\infty}\|u_\Delta(t^n)\|^2_{\mathbf{L^1}}\\
&+ \|\partial^2_{xy}\eta\|_{\mathbf{L}^\infty}\|u_\Delta(t^n)\|_{\mathbf{L^1}}\Big].
\end{aligned}
$$

Therefore we have K_2 and K_3 such that

$$
\begin{aligned}
\sum_{ij}\lambda_x|\tilde{D}^n_{ij}|\Delta x \leq&\Delta t\|U^0\|^2_{\mathbf{L^1}} M\Bigg(1 + \|\partial_x \eta\|_{\mathbf{L}^\infty} + \|\partial_y \eta\|_{\mathbf{L}^\infty}\\
&+ \|\partial_x \eta\|_{\mathbf{L}^\infty}\|\partial_y \eta\|_{\mathbf{L}^\infty}\|U^0\|_{\mathbf{L^1}} + \frac{1}{2}\|\partial^2_{xy}\eta\|_{\mathbf{L}^\infty}\Bigg)\\
&+ \Delta t\sum_{ij}|u_{i+1,j} - u_{ij}|\Delta y\left(\|\partial_u \partial_y f\|_{\mathbf{L}^\infty} + \|\partial_y \eta\|_{\mathbf{L}^\infty}\|U^0\|_{\mathbf{L^1}}\|\partial_u \nabla_A f\|_{\mathbf{L}^\infty}\right)\\
\leq&K_2\Delta t + K_3\Delta t\sum_{ij}|u_{i+1,j} - u_{ij}|\Delta y. \qquad \text{(A.8)}
\end{aligned}
$$

Collecting (A.7) and (A.8) above, we get

$$\sum_{ij}\left|u_{i,j+1}^{n+1/2}-u_{ij}^{n+1/2}\right|\Delta x\leq\sum_{ij}|u_{i,j+1}^{n}-u_{ij}^{n}|\Delta x$$
$$+K_2\Delta t+K_3\Delta t\sum_{ij}|u_{i+1,j}^{n}-u_{ij}^{n}|\Delta y.$$

It yields

$$\begin{aligned}&\sum_{ij}\left|u_{i+1,j}^{n+1/2}-u_{ij}^{n+1/2}\right|\Delta y+\left|u_{i,j+1}^{n+1/2}-u_{ij}^{n+1/2}\right|\Delta x\\ \leq&K_0\Delta t+(1+K_1\Delta t)\sum_{ij}\left|u_{i+1,j}^{n}-u_{ij}^{n}\right|\Delta y\\ &+\sum_{ij}|u_{i,j+1}^{n}-u_{ij}^{n}|\Delta x+K_2\Delta t+K_3\Delta t\sum_{ij}|u_{i+1,j}^{n}-u_{ij}^{n}|\Delta y\\ \leq&\Delta t(K_0+K_2)+(1+\Delta t(K_1+K_3))\sum_{ij}\left(|u_{i,j+1}^{n}-u_{ij}^{n}|\Delta x+|u_{i+1,j}^{n}-u_{ij}^{n}|\Delta y\right)\\ \leq&\mathcal{K}_2\Delta t+(1+\mathcal{K}_1\Delta t)\sum_{ij}\left(|u_{i,j+1}^{n}-u_{ij}^{n}|\Delta x+|u_{i+1,j}^{n}-u_{ij}^{n}|\Delta y\right).\end{aligned}\tag{A.9}$$

Entirely analogous estimates lead to the following total variation bound

$$\begin{aligned}\sum_{ij}\left(|u_{i+1,j}^{n+1}-u_{ij}^{n+1}|\Delta y+|u_{i,j+1}^{n+1}-u_{ij}^{n+1}|\Delta x\right)&=\mathbf{TV}(U^{n+1})\\ &\leq(1+\mathcal{K}_1\Delta t)\mathbf{TV}(U^{n+1/2})+\mathcal{K}_2\Delta t\\ &\leq(1+2\mathcal{K}_1\Delta t+(\mathcal{K}_1\Delta t)^2)\mathbf{TV}(U)^n+\mathcal{K}_2\Delta t(2+\mathcal{K}_1\Delta t).\end{aligned}$$

Applying Lemma A.0.1, we complete the proof

$$\begin{aligned}\mathbf{TV}(U^n)\leq&(1+\mathcal{K}_1\Delta t)^{2n}\mathbf{TV}(U^0)+\frac{(1+\mathcal{K}_1\Delta t)^{2n}-1}{\mathcal{K}_1\Delta t(2+\mathcal{K}_1\Delta t)}\mathcal{K}_2\Delta t(2+\mathcal{K}_1\Delta t)\\ \leq&(1+\mathcal{K}_1\Delta t)^{2n}\mathbf{TV}(U^0)+\frac{(1+\mathcal{K}_1\Delta t)^{2n}-1}{\mathcal{K}_1\Delta t}\mathcal{K}_2\Delta t\\ \leq&(1+\mathcal{K}_1\frac{t^n}{n})^{2n}\left(\mathbf{TV}(U^0)+\frac{\mathcal{K}_2}{\mathcal{K}_1}\right)-\frac{\mathcal{K}_2}{\mathcal{K}_1}\\ \leq&e^{2\mathcal{K}_1t^n}\left(\mathbf{TV}(U^0)+\frac{\mathcal{K}_2}{\mathcal{K}_1}\right)-\frac{\mathcal{K}_2}{\mathcal{K}_1}.\end{aligned}$$

□

Proof of Lemma 3.2.7 Following [5, Lemma 2.7], we have

$$\begin{aligned}\|u^{n+1/2}-u^n\|_{\mathbf{L^1}}=&\sum_{ij}\left|u_{ij}^{n+1/2}-u_{ij}^{n}\right|\Delta x\Delta y\\ \leq&\frac{\Delta t}{2}\Delta y\sum_{ij}\left|f_{i-1,j}(u_{i-1,j}^n)-f_{i+1,j}(u_{i+1,j}^n)\right|\\ &+\Delta t\Delta y\frac{\alpha}{\lambda_x}\sum_{ij}\left|u_{i+1,j}^{n}-u_{ij}^{n}\right|.\end{aligned}\tag{A.10}$$

We introduce suitable $\bar{x}_i \in [x_{i-1}, x_{i+1}]$, $\bar{u} \in I(u_{i-1,j}, u_{i+1,j})$ and $\bar{A}_{ij} \in I(\bar{A}_{i-1,j}, \bar{A}_{i+1,j})$ in (A.10) (and drop the n)

$$\begin{aligned}
\text{(A.10)} \leq & \frac{\Delta t}{2} \Delta y \sum_{ij} \left[2\Delta x \left\| \partial_x f(t^n, \bar{x}_i, y_j, \bar{u}_{ij}, \bar{A}_{ij}) \right\| \right. \\
& + |u_{i+1,j} - u_{i-1,j}| \left\| \partial_u f(t^n, \bar{x}_i, y_j, \bar{u}_{ij}, \bar{A}_{ij}) \right\| \\
& \left. + \|A_{i+1,j} - A_{i-1,j}\| \left\| \nabla_A f(t^n, \bar{x}_i, y_j, \bar{u}_{ij}, \bar{A}_{ij}) \right\| \right] \\
\leq & \Delta t M \|U^0\|_{\mathbf{L^1}} (1 + \|\partial \eta\|_{\mathbf{L}^\infty} \|U^0\|_{\mathbf{L^1}}) \\
& + \Delta t \|\partial_u f\|_{\mathbf{L}^\infty} \sum_{ij} \Delta y |u_{i+1,j} - u_{ij}|,
\end{aligned}$$

so that

$$\begin{aligned}
\|u^{n+1/2} - u^n\|_{\mathbf{L^1}} \leq & \Delta t M \|U^0\|_{\mathbf{L^1}} (1 + \|\partial \eta\|_{\mathbf{L}^\infty} \|U^0\|_{\mathbf{L^1}}) \\
& + \Delta t \left(\frac{\alpha}{\lambda_x} + \|\partial_u f\|_{\mathbf{L}^\infty} \right) \sum_{ij} \Delta y |u_{i+1,j} - u_{ij}|,
\end{aligned}$$

which, together with the analogous estimate for $\|u^{n+1} - u^{n+1/2}\|_{\mathbf{L^1}}$, yields

$$\begin{aligned}
& \|u^{n+1} - u^n\|_{\mathbf{L^1}} \leq \Delta t M \|U^0\|_{L^1} \left(2 + (\|\partial_x \eta\|_{\mathbf{L}^\infty} + \|\partial_y \theta\|_{\mathbf{L}^\infty}) \|U^0\|_{\mathbf{L^1}} \right) \\
& \quad + \Delta t \left(\|\partial_u f\|_{\mathbf{L}^\infty} + \frac{\alpha}{\lambda_x} + \|\partial_u g\|_{\mathbf{L}^\infty} + \frac{\beta}{\lambda_y} \right) \left(\sum_{ij} \Delta x |u_{i,j+1} - u_{i,j-1}| + \Delta y |u_{i+1,j} - u_{i-1,j}| \right) \\
& \quad \leq \Delta t M \|U^0\|_{L^1} \left(2 + (\|\partial_x \eta\|_{\mathbf{L}^\infty} + \|\partial_y \theta\|_{\mathbf{L}^\infty}) \|U^0\|_{\mathbf{L^1}} \right) \\
& \quad + \Delta t \left(\|\partial_u f\|_{\mathbf{L}^\infty} + \frac{\alpha}{\lambda_x} + \|\partial_u g\|_{\mathbf{L}^\infty} + \frac{\beta}{\lambda_y} \right) \left(e^{2\mathcal{K}_1 t^n} \mathbf{TV}(U^0) + \frac{\mathcal{K}_2}{\mathcal{K}_1} (e^{2\mathcal{K}_1 t^n} - 1) \right).
\end{aligned}$$

We denote the bounding constant

$$\begin{aligned}
C(t^n) = & M \|U^0\|_{L^1} \left(2 + (\|\partial_x \eta\|_{\mathbf{L}^\infty} + \|\partial_y \theta\|_{\mathbf{L}^\infty}) \|U^0\|_{\mathbf{L^1}} \right) \\
& + \left(\|\partial_u f\|_{\mathbf{L}^\infty} + \frac{\alpha}{\lambda_x} + \|\partial_u g\|_{\mathbf{L}^\infty} + \frac{\beta}{\lambda_y} \right) \left(e^{2\mathcal{K}_1 t^n} \mathbf{TV}(U^0) + \frac{\mathcal{K}_2}{\mathcal{K}_1} (e^{2\mathcal{K}_1 t^n} - 1) \right).
\end{aligned} \tag{A.11}$$

□

Proof of Theorem 3.2.1 The **BV** estimate in Lemma (3.2.5) allows to use classical tools. Indeed, for instance, all properties 1. to 6. in [78] hold. More precisely, 1. follows from Lemma (3.2.3) through [78, Lemma 3.3], 2. follows from Lemma 3.2.5, 3. follows from Lemma 3.2.7, 4. follows from Lemma 3.2.4, 5. follows from 6. with $c = 0$, 6. follows from Lemma 3.2.6. Hence, for any sequence $(\Delta t)_w$, $(\Delta x)_w$, $(\Delta y)_w$ tending to 0 and satisfying for any w the CFL condition (3.7), [78, Proposition 3.1] ensures the convergence, up to a subsequence, of the approximations u_w^k to a solution U^k of (3.3), for $k = 1, \ldots, N$.
By [26, 28], the terms A and B converge to the respective convolutions integrals, ensuring that U^k solves (3.1) in the sense of Definition 3.2.1.
Finally, the uniformity of the bounds proved in the lemmas allows to pass each of these bounds to the solution, completing the proof.

□

Appendix B

Lagrange multipliers computation

In this part we give the details of the Lagrangian derivative computation. We recall that $f_{ij}^n = f(t^n, x_i, y_j, u_{ij}^n, \eta * U^n)$ where $U^n = \left\{u_{ij}^n\right\}_{\substack{1\leq i\leq N_x \\ 1\leq j\leq N_y}}$

$$
\begin{aligned}
&\Delta t \partial_{u_{ij}^n} L(\mathbf{u}^0, u_\Delta, \boldsymbol{\phi}) = \Delta x \Delta y \Delta t^2 + \phi_{ij}^{n-1/2} - \phi_{ij}^n \\
&+ \lambda_x \sum_{\substack{r\,\in\,[1\ldots N_x] \\ s\,\in\,[1\ldots N_y]}} \phi_{rs}^n \left[\partial_{u_{ij}} F_{r+1/2,s}^n \chi_{r+1/2,s}^F - \partial_{u_{ij}} F_{r-1/2,s}^n \chi_{r-1/2,s}^F\right] \\
&= \Delta x \Delta y \Delta t^2 + \phi_{ij}^{n-1/2} - \phi_{ij}^n \\
&+ \lambda_x \sum_{s\in[1\ldots N_y]} \Bigg[- \phi_{1,j} \partial_{u_{ij}^n} f_{1,s}^n \chi_{1/2,s}^F + \phi_{N,j} \partial_{u_{ij}^n} f_{N,s}^n \chi_{N+1/2,s}^F \\
&+ \sum_{r\in[1\ldots N_x-1]} (\phi_{rs}^n - \phi_{r+1,s}^n) \partial_{u_{ij}^n} F_{r+1/2,s}^n \chi_{r+1/2,s}^F \Bigg] \\
&= \Delta x \Delta y \Delta t^2 + \phi_{ij}^{n-1/2} - \phi_{ij}^n + \lambda_x \sum_{s\in[1\ldots N_y]} \Bigg[\\
&+ \frac{1}{2} \sum_{r\in[2\ldots N_x-1]} \partial_{u_{ij}^n} f_{rs}^n \left[(\phi_{rs}^n - \phi_{r+1,s}^n)\chi_{r+1/2,s}^F + (\phi_{r-1,s}^n - \phi_{rs}^n)\chi_{r-1/2,s}^F\right] \\
&+ \frac{1}{2} \partial_{u_{ij}^n} f_{1,s}^n (\phi_{1,s}^n - \phi_{2,s}^n)\chi_{3/2,s}^F + \frac{1}{2} \partial_{u_{ij}^n} f_{N,s}^n (\phi_{N-1,s}^n - \phi_{N,s}^n)\chi_{N-1/2,s}^F \\
&+ \left(\frac{-\alpha}{2\lambda_x}\right) \sum_{r\in[2\ldots N_x-1]} \partial_{u_{ij}^n} u_{rs}^n \left[-(\phi_{rs}^n - \phi_{r+1,s}^n)\chi_{r+1/2,s}^F + (\phi_{r-1,s}^n - \phi_{rs}^n)\chi_{r-1/2,s}^F\right] \\
&- \left(\frac{-\alpha}{2\lambda_x}\right) \partial_{u_{ij}^n} u_{1,s}^n (\phi_{1,s}^n - \phi_{2,s}^n)\chi_{3/2,s}^F + \left(\frac{-\alpha}{2\lambda_x}\right) \partial_{u_{ij}^n} u_{N,s}^n (\phi_{N-1,s}^n - \phi_{N,s}^n)\chi_{N-1/2,s}^F \Bigg].
\end{aligned}
$$

We recall

$$\Phi^f_{rs} = \left| \begin{array}{ll} \frac{1}{2}\left[(\phi^n_{rs} - \phi^n_{r+1,s})\chi^F_{r+1/2,s} + (\phi^n_{r-1,s} - \phi^n_{rs})\chi^F_{r-1/2,s}\right] & \forall r \in [2...N_x - 1], \\ \frac{1}{2}(\phi^n_{1,s} - \phi^n_{2,s})\chi^F_{3/2,s} - \phi^n_{1,s}\chi^F_{1/2,s} & \text{for } r = 1, \\ \phi^n_{N,s}\chi^F_{N+1/2,s} + \frac{1}{2}(\phi^n_{N-1,s} - \phi^n_{N,s})\chi^F_{N-1/2,s} & \text{for } r = N, \end{array} \right. \tag{B.1}$$

$$\Phi^\alpha_{rs} = \left| \begin{array}{ll} \left[-(\phi^n_{rs} - \phi^n_{r+1,s})\chi^F_{r+1/2,s} + (\phi^n_{r-1,s} - \phi^n_{rs})\chi^F_{r-1/2,s}\right] & \forall r \in [2...N_x - 1], \\ -(\phi^n_{1,s} - \phi^n_{2,s})\chi^F_{3/2,s} & \text{for } r = 1, \\ (\phi^n_{N-1,s} - \phi^n_{N,s})\chi^F_{N-1/2,s} & \text{for } r = N. \end{array} \right.$$

Then

$$\begin{aligned} &\Delta t \partial_{u^n_{ij}} L(u^0, u, \phi) \\ &= \Delta x \Delta y \Delta t^2 + \phi^{n-1/2}_{ij} - \phi^n_{ij} + \lambda_x \sum_{\substack{r \in [1...N_x] \\ s \in [1...N_y]}} \Phi^f_{rs} \partial_{u^n_{ij}} f^n_{rs} + \left(\frac{-\alpha}{2}\right) \Phi^\alpha_{ij} \\ &= \Delta x \Delta y \Delta t^2 + \phi^{n-1/2}_{ij} - \phi^n_{ij} + \left(\frac{-\alpha}{2}\right) \Phi^\alpha_{ij} + \Phi^f_{ij} \left(\nu_x + \mathcal{I}_x\right)_{ij} \partial_{u^n_{ij}} \bar{f}^n_{ij} \\ &+ \lambda_x \sum_{\substack{r \in [1...N_x] \\ s \in [1...N_y]}} \Phi^f_{rs} \bar{f}^n_{rs} \partial_{u^n_{ij}} \left[\mathcal{I}_x\right]_{rs}. \end{aligned}$$

Then we differentiate the deviation term $\mathcal{I}$

$$\begin{aligned} &\partial_{u^n_{ij}} (\mathcal{I}_x(U^n * \nabla\eta))_{rs} = \partial_{u^n_{ij}} \left[-\varepsilon \frac{(U^n * \partial_x \eta)_{rs}}{\sqrt{1 + (\|U^n * \nabla\eta\|^2)_{rs}}}\right] \\ &= \frac{-\varepsilon}{\sqrt{1 + (\|U^n * \nabla\eta\|^2)_{rs}}^3} \left[\partial_{u^n_{ij}} \left((U^n * \partial_x \eta)_{rs}\right) \left(1 + \|U^n * \nabla\eta\|^2\right)_{rs} \right. \\ &\quad \left. - \frac{(U^n * \partial_x \eta)_{rs}}{2} \partial_{u^n_{ij}} \left(\left(\|U^n * \nabla\eta\|^2\right)_{rs}\right)\right], \end{aligned}$$

$$\begin{aligned} \partial_{u^n_{ij}} \left((U^n * \partial_x \eta)_{rs}\right) &= \partial_{u^n_{ij}} \sum_{p,q \in \mathbb{Z}} u_{p,q} \left(\partial_x \eta\right)_{r-p+1, s-q+1} \Delta x \Delta y \\ &= \left(\partial_x \eta\right)_{\substack{r-i \\ s-j}} \Delta x \Delta y, \\ \partial_{u^n_{ij}} \left(\left(\|U^n * \nabla\eta\|^2\right)_{rs}\right) &= \partial_{u^n_{ij}} \left(|(U^n * \partial_x \eta)_{rs}|^2\right) + \partial_{u^n_{ij}} \left(|(U^n * \partial_y \eta)_{rs}|^2\right) \\ &= 2(U^n * \partial_x \eta)_{rs} \left(\partial_x \eta\right)_{\substack{r-i \\ s-j}} \Delta x \Delta y \\ &\quad + 2(U^n * \partial_y \eta)_{rs} \left(\partial_y \eta\right)_{\substack{r-i \\ s-j}} \Delta x \Delta y, \end{aligned}$$

$$
\begin{aligned}
&\partial_{u_{ij}^n}\left((\mathcal{I}_x(U^n * \nabla\eta))_{rs}\right)\\
=&\frac{-\varepsilon}{\sqrt{1+(\|U^n * \nabla\eta\|^2)_{rs}}^3}\Bigg[\left(1+\|U^n * \nabla\eta\|^2\right)_{rs}(\partial_x\eta)_{\substack{r-i\\s-j}}\Delta x\Delta y\\
&-\Bigg(\left[(U^n * \partial_x\eta)_{rs}\right]^2(\partial_x\eta)_{\substack{r-i\\s-j}}\Delta x\Delta y\\
&-\ (U^n * \partial_x\eta)_{rs}(U^n * \partial_y\eta)_{rs}(\partial_y\eta)_{\substack{r-i\\s-j}}\Delta x\Delta y\Bigg)\Bigg]\\
=&\frac{-\varepsilon}{\sqrt{1+(\|U^n * \nabla\eta\|^2)_{rs}}^3}\Bigg[\left(1+((U^n * \partial_y\eta)_{rs})^2\right)(\partial_x\eta)_{\substack{r-i\\s-j}}\Delta x\Delta y\\
&-(U^n * \partial_x\eta)_{rs}(U^n * \partial_y\eta)_{rs}(\partial_y\eta)_{\substack{r-i\\s-j}}\Delta x\Delta y\Bigg].
\end{aligned}
$$

We denote

$$
\check{I}_{rs}^n = -\varepsilon\frac{1+(U^n * \partial_y\eta)_{rs}^2}{\sqrt{1+(\|U^n * \nabla\eta\|^2)_{rs}}^3},\ \hat{I}_{rs}^n = \varepsilon\frac{(U^n * \partial_x\eta)_{rs}(U^n * \partial_y\eta)_{rs}}{\sqrt{1+(\|U^n * \nabla\eta\|^2)_{rs}}^3}, \tag{B.2}
$$

so

$$
\partial_{u_{ij}^n}(\mathcal{I}_x(U^n * \nabla\eta))_{rs} = \check{I}_{rs}^n(\partial_x\eta)_{\substack{r-i\\s-j}}\Delta x\Delta y + \hat{I}_{rs}^n(\partial_y\eta)_{\substack{r-i\\s-j}}\Delta x\Delta y.
$$

Finally,

$$
\begin{aligned}
&\Delta t\partial_{u_{ij}^n}L(u^0,u,\phi) = \Delta x\Delta y\Delta t^2 + \phi_{ij}^{n-1/2} - \phi_{ij}^n + \left(\frac{-\alpha}{2}\right)\Phi_{ij}^\alpha\\
&+\lambda_x\Phi_{ij}^f(\nu_x+\mathcal{I}_x)_{ij}\partial_{u_{ij}^n}\bar{f}_{ij}^n\\
&+\lambda_x\sum_{\substack{r\in[1\ldots N_x]\\s\in[1\ldots N_y]}}\Phi_{rs}^f\bar{f}_{rs}^n\left[\check{I}_{rs}^n(\partial_x\eta)_{\substack{r-i\\s-j}}\Delta x\Delta y + \hat{I}_{rs}^n(\partial_y\eta)_{\substack{r-i\\s-j}}\Delta x\Delta y\right],
\end{aligned}
$$

so with

$$
\begin{aligned}
\overline{(\partial_x\eta)}_{\substack{i-r\\j-s}} &= (\partial_x\eta)_{\substack{r-i\\s-j}},\\
\overline{(\partial_y\eta)}_{\substack{i-r\\j-s}} &= (\partial_y\eta)_{\substack{r-i\\s-j}},
\end{aligned} \tag{B.3}
$$

and

$$
\begin{aligned}
\mathbf{\Phi}_{rs}^1 &= \Phi_{rs}^f\bar{f}_{rs}^n I_{rs}^n,\\
\mathbf{\Phi}_{rs}^2 &= \Phi_{rs}^f\bar{f}_{rs}^n P_{rs}^n,
\end{aligned} \tag{B.4}
$$

it leads to the final expression of the Lagrangian derivative (3.25)

$$
\begin{aligned}
&\Delta t\partial_{u_{ij}^n}L(u^0,u,\phi) = \Delta x\Delta y\Delta t^2 + \phi_{ij}^{n-1/2} - \phi_{ij}^n + \left(\frac{-\alpha}{2}\right)\Phi_{ij}^\alpha\\
&+\lambda_x\left(\Phi_{ij}^f(\nu_x+\mathcal{I}_x)_{ij}\partial_{u_{ij}^n}\bar{f}_{ij}^n c + (\mathbf{\Phi}^1 * (\partial_x\eta)')_{ij} + (\mathbf{\Phi}^2 * (\partial_y\eta)')_{ij}\right).
\end{aligned}
$$

Appendix C

Generating the velocity vector field using the eikonal equation

The eikonal equation is a partial differential equation regularly used in wave propagation problems like electromagnetism, granular matter and computer vision. The *potential objective* described by Hughes in [56] can be given by an eikonal equation, with an exit as the output on the boundary. The vector field directing the pedestrian's motion is obtain by differentiating the solution of the associated eikonal equation.
We recall here how to solve numerically the eikonal equation

$$\begin{cases} \|\nabla\varphi(x,y)\| = c(x,y), & \text{for } (x,y) \in \Omega, \\ \varphi(x,y) = 0, & \text{for } (x,y) \in \Gamma_o \end{cases}$$

with $\Omega \in \mathbb{R}^2$ and $\partial\Omega = \Gamma_w \cup \Gamma_o$, see Fig. C.1. $c : \Omega \mapsto \mathbb{R}$ is the *running cost* function.
We use a procedure based on the *fast sweeping* method developed by H. Zhao in [86]. It updates the solution φ after several sweepings of the domain. For $\|\nabla\varphi\| = 1$, the solution represents the distance function from Γ_o of any point in the domain. Then we get $\nabla\varphi$ by central differentiation.

C.1 Numerical method

The fast sweeping uses a Godunov upwind difference scheme to discretize the partial differential equation at interior points of the domain. We denote (x_i, y_j), $i = 1...N_x$ and $j = 1...N_y$, a grid point of the discretized domain, $\Delta x = \Delta y = h$ to denote the grid size and $\varphi^h_{ij} = \varphi(x_i, y_j)$:

$$\begin{gathered} [(\varphi^h_{ij} - \varphi^h_{xmin})^+]^2 + [(\varphi^h_{ij} - \varphi^h_{ymin})^+]^2 = c^2_{ij}h^2, \\ i = 2, ..., N_x - 1, j = 2, ..., N_y - 1, \end{gathered} \tag{C.1}$$

where $\varphi^h_{xmin} = \min(\varphi^h_{i-1,j}, \varphi^h_{i+1,j})$ and $\varphi^h_{ymin} = \min(\varphi^h_{i,j-1}, \varphi^h_{i,j+1})$ and

$$(x)^+ = \begin{cases} x, & x > 0, \\ 0, & x \leq 0. \end{cases}$$

The algorithm is described in [86, Sec. 2.1] and consists in initializing ϕ to zero on Γ_o and sufficiently large positive values at all other grid points. They are updated then by *sweeping*

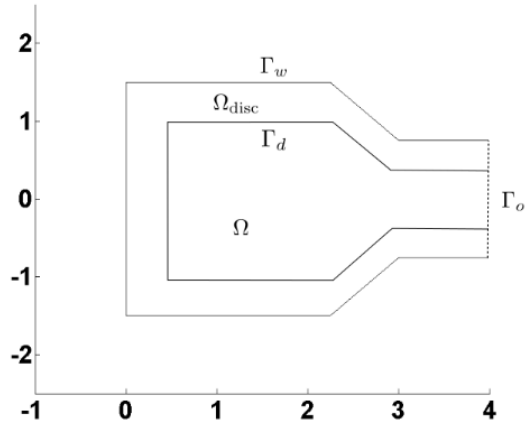

Figure C.1: The domain Ω, with $\Omega_{\text{disc}} \subset \Omega$ and the boundaries Γ_w, Γ_d and Γ_o.

the domain several times, taking the minimum of $\varphi_{ij}^{\text{old}}$, the previous value of the cell i, j, and $\varphi_{ij}^{\text{new}}$, given by the equation C.1

$$\varphi_{ij}^{\text{new}} = \begin{cases} \min(\varphi_{xmin}^h, \varphi_{ymin}^h) + c_{ij}h, & \left|\varphi_{xmin}^h - \varphi_{ymin}^h\right| \geq c_{ij}h, \\ \frac{\varphi_{xmin}^h + \varphi_{ymin}^h + \sqrt{2c_{ij}^2 h^2 - (\varphi_{xmin}^h - \varphi_{ymin}^h)^2}}{2}, & \left|\varphi_{xmin}^h - \varphi_{ymin}^h\right| < c_{ij}h. \end{cases}$$

It stops when the difference $\left\|\varphi^{\text{new}} - \varphi^{\text{old}}\right\|$ goes below a threshold defined by the user.

C.2 Convergence of the numerical scheme

In this section we analyze the $\mathbf{L^1}$ errors and convergence order for the *fast sweeping* used to solve the eikonal equation and to approximate its gradient. We compute the geodesics ($c = 1$) φ of a domain Ω, the union of a room $[0, 3] \times [-1.5, 1.5]$ and a corridor $[3, 4] \times [-0.75, 0.75]$ with an exit Γ_o at $x = 4$. The room is connected to the corridor by sliders orientated with $45°$.

Let Ω_{h_k} be a the mesh of $N_{k,x}$ cells in the x direction and $N_{k,y}$ cells in the y direction with space steps h_k. We consider the $\mathbf{L^1}$ error between a reference solution φ^{ref} and the approximate one φ^{h_k}

$$e_k = \sum_{i=1,j=1}^{N_{k,x},N_{k,y}} \left|\varphi_{ij}^{h_k} - \varphi_{ij}^{\text{ref}}\right| h_k^2$$

We assume that $e_k = Ch_k^\gamma + o(h_k^{\gamma+1})$ with C a constant, and estimate the order of convergence $\gamma = \log_2 \frac{\|e_k - e_{k+1}\|}{\|e_{k+1} - e_{k+2}\|}$.

We solve the following system on Ω

$$\begin{cases} \|\nabla\varphi(x, y)\| = 1, & \text{for } (x, y) \in \Omega, \\ \varphi(x, y) = 0, & \text{for } (x, y) \in \Gamma_o. \end{cases}$$

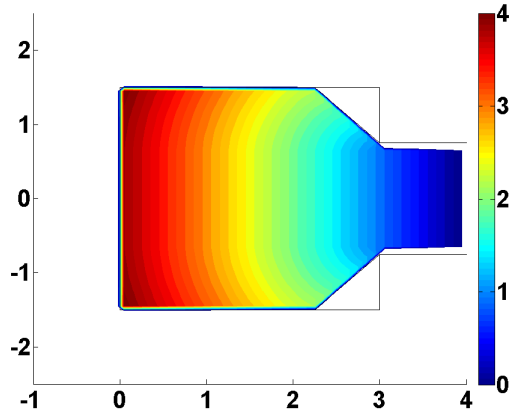

Figure C.2: The potential φ on Ω.

Δx	e_φ	γ_φ
0.20000	08.4722	0.97
0.10000	04.3211	0.91
0.05000	02.3004	1.03
0.02500	01.1189	1.02
0.01250	00.5515	1.15
0.00625	00.2485	

Table C.1: Order of convergence of φ.

Δx	$e_{\nabla_x\varphi}$	$\gamma_{\nabla_x\varphi}$	$e_{\nabla_y\varphi}$	$\gamma_{\nabla_y\varphi}$
0.20000	1.5198	1.01	3.0163	0.85
0.10000	0.7531	0.80	1.6772	0.87
0.05000	0.4330	1.12	0.9227	0.90
0.02500	0.1986	0.95	0.4960	0.96
0.01250	0.1028	1.08	0.2555	1.09
0.00625	0.0485		0.1197	

Table C.2: Order of convergence of $\nabla\varphi$.

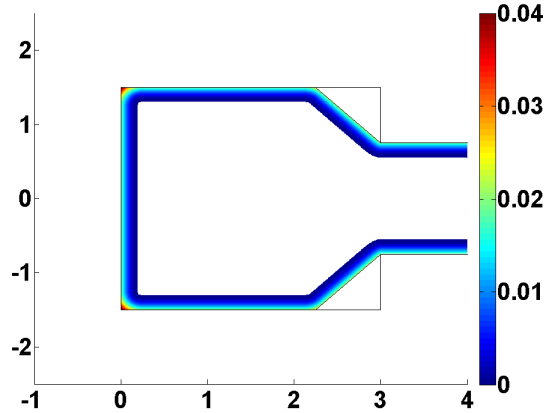

Figure C.3: The potentials φ_{disc}.

We perform 6 simulations starting with $\Delta x = 0.2$ successively halved.
The size of the space step $\Delta x = \Delta y = h$ goes from 0.2 to 0.00625 with a reference grid with a space step size 0.0015625 and a stop condition $\left\|\varphi^{\text{new}} - \varphi^{\text{old}}\right\| < 10^{-3}$. Then the gradient is obtained by central differentiation of the solution (and upward/backward at the boundary).
It computes the solution in 3 iterations. The order of convergence of the solution of the eikonal equation is approximately 1, as for its gradient. This superconvergence has been numerically notified in literature but still under investigation, see [13].

C.3 Computing the discomfort vector field

We want to create a linearly decreasing vector field along the walls in order to repulse pedestrians from walls and obstacle. On this purpose we set the subregion $\Omega_{\text{disc}} \subset \Omega_{\text{ped}}$, see Fig. C.1. We call the interior boundary $\Gamma_{\text{disc}} = \partial\Omega_{\text{disc}} \setminus (\Gamma_w \cup \Gamma_o)$.
The potential φ_{disc}, see Fig. C.3, associated to a linearly decreasing vector field from Γ_w to Γ_{disc} is the solution of the following eikonal equation which takes as cost function c_{disc} the distance to Γ_{disc}

$$\begin{cases} |\nabla\varphi_{\text{disc}}(x,y)| = c_d(x,y), & \text{for } (x,y) \in \Omega, \\ \varphi_{\text{disc}}(x,y) = 0, & \text{for } (x,y) \in \Gamma_{\text{disc}}. \end{cases}$$

Remark that c_{disc} is the solution of a previous eikonal equation on Ω_{disc} with $\partial\Omega_{\text{disc}}$ as output. ν is based on the potentials φ_{ped}, on Ω, and φ_{disc}, on Ω_{disc}.It is the normalized sum of the normalized vector field $\nu_{\text{ped}} = \frac{\nabla\varphi_{\text{ped}}}{\left\|\nabla\varphi_{\text{ped}}\right\|}$ and the linearly decreasing vector field $\nu_{\text{disc}} = k\frac{\nabla\varphi_{\text{disc}}}{\left\|\nabla\varphi_{\text{disc}}\right\|_{\mathbb{L}^\infty}}$, $k > 0$, see Fig. C.4. We compute them by central finite differentiation of the potentials φ_{ped}, see Fig. C.2 and φ_{disc}, see Fig. C.3.

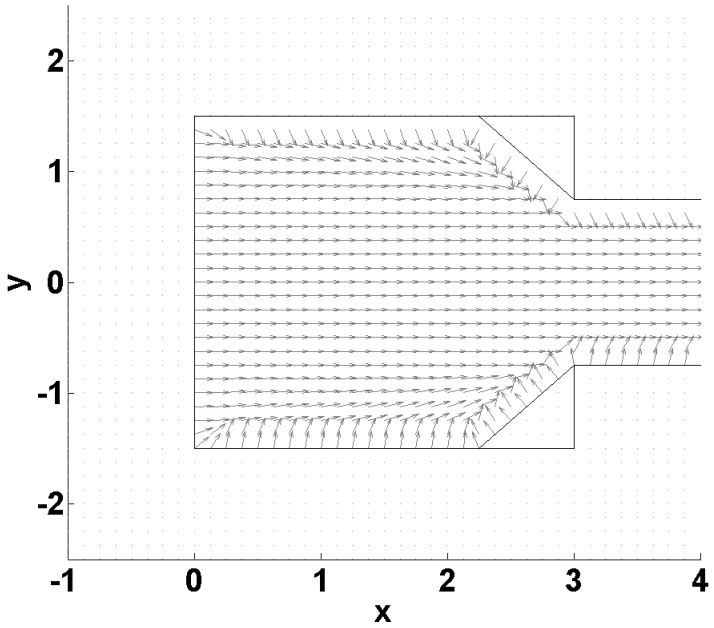

Figure C.4: The vector field ν.

Appendix D

Anisotropic convolution kernel

While walking, pedestrians evaluate inhomogeneously the density around them. They pay more attention to what is happening in front of them than to what is on their sides or their back. From a mathematical point of view, the density has to be processed through an anisotropic nonlocal operator orientated towards the flow direction.
We explore here the features of an anisotropic kernel $\mu_{\mathcal{S}}$ on the behavior of a crowd governed by [3.10,3.11]. The kernel will be the smoothed and normalized section of an homogeneous kernel μ. The expression of a section $\mathcal{S}$ centered at (x_0, y_0) for a given angle $2\bar{\alpha}$ and a direction $\nu_{\text{dir}} \in \mathbb{R}^2$ is

$$\mathcal{S}(x_0, y_0) = \Big\{(x, y) \in \mathbb{R}^2 : \|(x, y) - (x_0, y_0)\|_2 \leq r, \\ \frac{((x, y) - (x_0, y_0)) \cdot \nu_{\text{dir}}(x_0, y_0)}{\|(x, y) - (x_0, y_0)\| \|\nu_{\text{dir}}(x_0, y_0)\|} \geq \cos \bar{\alpha}\Big\}$$

The center (x_0, y_0) of the section will not necessarily be $(0, 0)$, the center of the kernel. For instance in the following, we choose to center the most influential part of the kernel on the pedestrian head by slightly shifting the center of her head, see Fig. D.2. The smoothing is made through a convolution with a gaussian $\exp(-\frac{x^2+y^2}{2\sigma^2})$ with $\sigma = 0.02$.

D.1 Numerical integrations

We consider the settings of Section 3.2.3. The crowd will move along a corridor $[0, 10] \times [-1, 1]$ and will be governed by the flux (3.10) and the vector field ν discribed in (3.11). The homogeneous kernel μ is described in (3.11):

$$\tilde{\mu}(x, y) = \left(0.16 - x^2 - y^2\right)^3 \chi_{\{]-0.4,0.4]\times[-0.4,0.4]\}}(x, y), \quad \mu(x, y) = \frac{\tilde{\mu}(x, y)}{\iint_{\mathbb{R}^2} \tilde{\mu}}.$$

The section will be different for each case. We shift the center of the section on a distance 0.15 in the opposite direction of ν_{dir}.
The constants and discretization are

$$\begin{array}{ll} U_{\max} = 1\,\text{ped}.m^{-2}, & \Delta x = \Delta y = 0.00625\,m, \\ V_{\max} = 1\,m.s^{-1}, & \lambda_x = \lambda_y = 1/7\,s.m^{-1}, \\ U_{\text{init}} = 5\text{ ped}, & \varepsilon = 0.5. \\ T_{\max} = 20\,s, & \end{array}$$

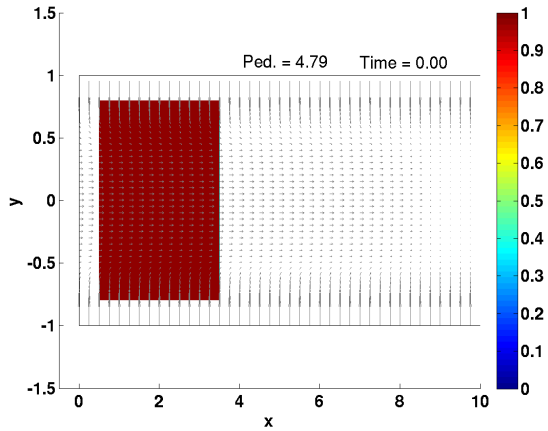

Figure D.1: Initial data and vector field for all tests.

We take as an initial value $U^0 \in (\mathbf{L^1} \cap \mathbf{L^\infty} \cap \mathbf{BV})(\mathbb{R}^2; [0,1])$

$$U^0(x,y) = \chi_{[0.5,3.5]\times[-0.8,0.8]}(x,y). \tag{D.1}$$

We proceed to six tests with different $\bar{\alpha}$ and ν_{dir}. For the formers we fix $\nu_{\text{dir}} = (1,0)$ and take $\bar{\alpha} = \frac{\pi}{16}$, $\frac{\pi}{8}$, $\frac{\pi}{4}$ and π. For the latters we fix $\bar{\alpha} = \frac{\pi}{8}$ and take $\nu_{\text{dir}} = (-1,0)$ and $(0,-1)$.
In the way of the numerical tests of Blandin and Goatin in [18, 4.1], we remark that the downstream kernel with $\bar{\alpha} = \frac{\pi}{4}$, see Fig. D.4 gives more diffusive profile than the isotropic kernel, see Fig. D.3, and conversely the upstream kernel does not lead to horizontal lane formation but to a vertically oscillating profile, see Fig. D.7. Those oscillations occur also with the sharper downstream kernels with $\bar{\alpha} = \frac{\pi}{8}$ and $\frac{\pi}{16}$, see Figs. D.5 and D.6, suggesting that the density's information on the sides of the pedestrian is crucial to the lane formation. The slightly distorted lanes in the last test, see Fig. D.8, advocate this interpretation.

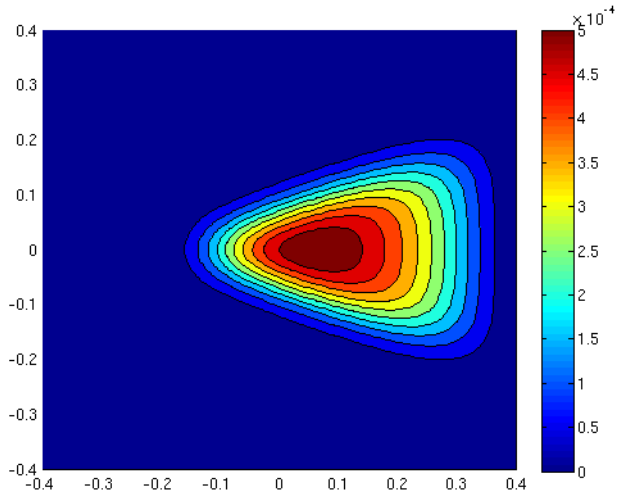

Figure D.2: Kernel for $\bar{\alpha} = \frac{\pi}{8}$ and $\nu_{\text{dir}} = (1, 0)$.

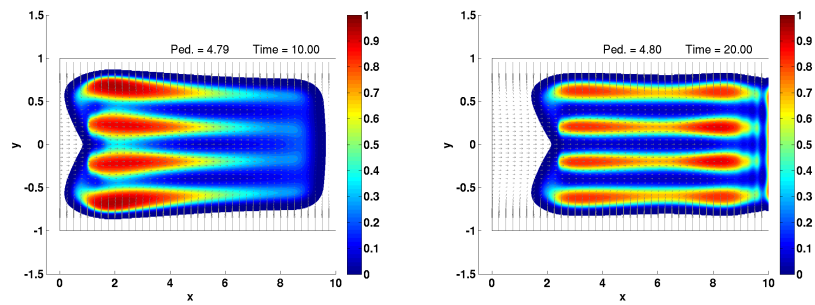

Figure D.3: Snapshots of the evacuation for $\bar{\alpha} = \pi$ and $\nu_{\text{dir}} = (1, 0)$ at $T = 10$ and $T = 20$.

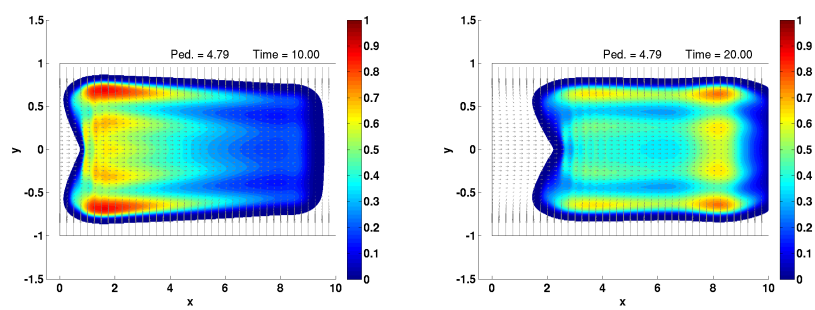

Figure D.4: Snapshots of the evacuation for $\bar{\alpha} = \frac{\pi}{4}$ and $\nu_{\text{dir}} = (1, 0)$ at $T = 10$ and $T = 20$.

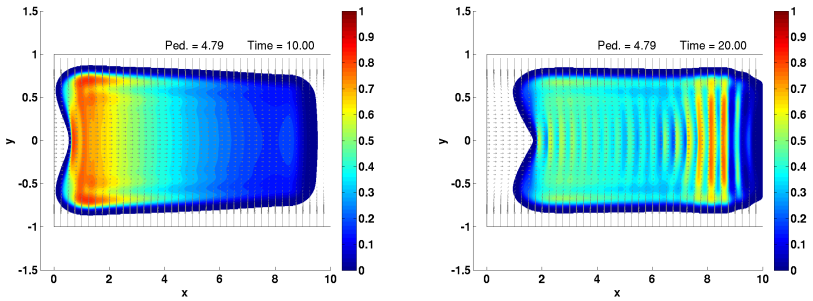

Figure D.5: Snapshots of the evacuation for $\bar{\alpha} = \frac{\pi}{8}$ and $\nu_{\text{dir}} = (1, 0)$ at $T = 10$ and $T = 20$.

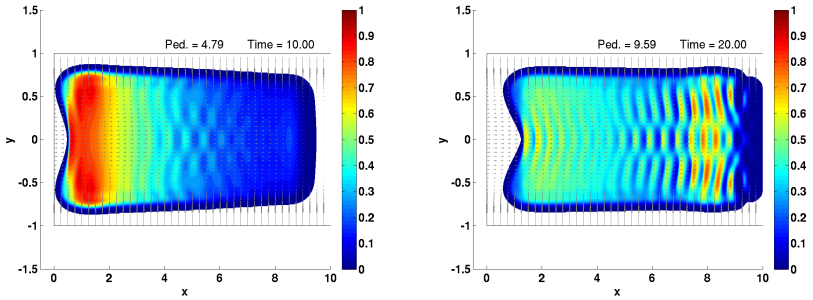

Figure D.6: Snapshots of the evacuation for $\bar{\alpha} = \frac{\pi}{16}$ and $\nu_{\text{dir}} = (1, 0)$ at $T = 10$ and $T = 20$.

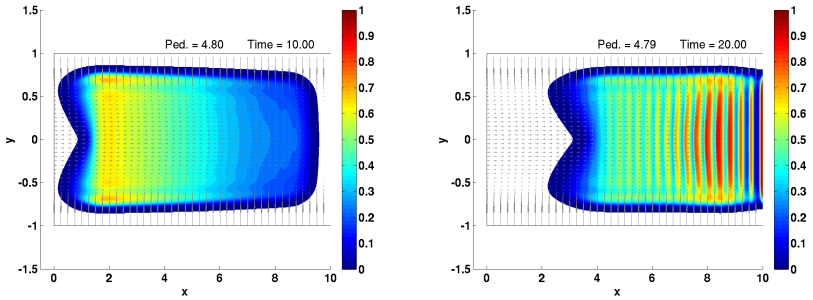

Figure D.7: Snapshots of the evacuation for $\bar{\alpha} = \frac{\pi}{8}$ and $\nu_{\text{dir}} = (-1, 0)$ at $T = 10$ and $T = 20$.

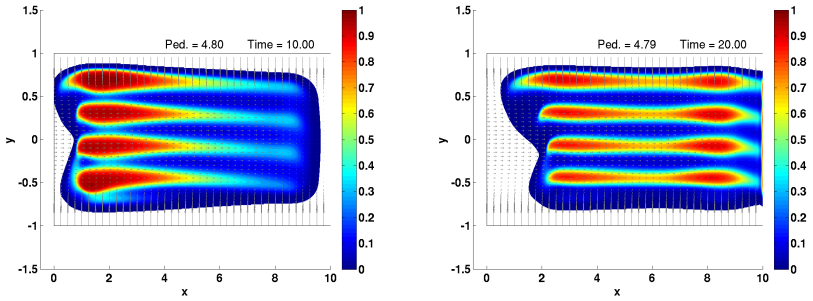

Figure D.8: Snapshots of the evacuation for $\bar{\alpha} = \frac{\pi}{8}$ and $\nu_{\text{dir}} = (0, -1)$ at $T = 10$ and $T = 20$.

Bibliography

[1] A. Aggarwal, R. M. Colombo, and P. Goatin. Nonlocal systems of conservation laws in several space dimensions. *SIAM Journal on Numerical Analysis*, 53(2):963–983, 2015.

[2] D. Amadori and M. Di Francesco. The one-dimensional Hughes model for pedestrian flow: Riemann-type solutions. *Acta Math. Sci. Ser. B Engl. Ed.*, 32(1):259–280, 2012.

[3] D. Amadori, P. Goatin, and M. D. Rosini. Existence results for Hughes' model for pedestrian flows. *J. Math. Anal. Appl.*, 420(1):387–406, 2014.

[4] D. Amadori and W. Shen. An integro-differential conservation law arising in a model of granular flow. *J. Hyperbolic Differ. Equ.*, 9(1):105–131, 2012.

[5] P. Amorim, R. M. Colombo, and A. Teixeira. On the numerical integration of scalar nonlocal conservation laws. *ESAIM: M2AN*, 49(1):19–37, 2015.

[6] C. Appert-Rolland, P. Degond, and S. Motsch. Two-way multi-lane traffic model for pedestrians in corridors. *Netw. Heterog. Media*, 6(3):351–381, 2011.

[7] D. Armbruster, P. Degond, and C. Ringhofer. A model for the dynamics of large queuing networks and supply chains. *SIAM J. Appl. Math.*, 66(3):896–920, 2006.

[8] D. Armbruster, D. E. Marthaler, C. Ringhofer, K. Kempf, and T.-C. Jo. A continuum model for a re-entrant factory. *Oper. Res.*, 54(5):933–950, Sept. 2006.

[9] C. Bardos, A. Y. le Roux, and J.-C. Nédélec. First order quasilinear equations with boundary conditions. *Comm. Partial Differential Equations*, 4(9):1017–1034, 1979.

[10] J. B. Bell, J. A. Trangenstein, and G. R. Shubin. Conservation laws of mixed type describing three-phase flow in porous media. *SIAM J. Appl. Math.*, 46(6):1000–1017, 1986.

[11] N. Bellomo and A. Bellouquid. On the modeling of crowd dynamics: Looking at the beautiful shapes of swarms. *Networks and Heterogeneous Media*, 6(3):383–399, 2011.

[12] N. Bellomo and C. Dogbé. On the modelling of crowd dynamics from scaling to hyperbolic macroscopic models. *Mathematical Models and Methods in Applied Sciences*, 18(supp01):1317–1345, 2008.

[13] J.-D. Benamou, S. Luo, and H. Zhao. A compact upwind second order scheme for the eikonal equation. *J. Comput. Math.*, 28(4):489–516, 2010.

[14] S. Benzoni-Gavage and R. M. Colombo. An n-populations model for traffic flow. *European J. Appl. Math.*, 14(5):587–612, 2003.

[15] S. Berres, R. Ruiz-Baier, H. Schwandt, and E. M. Tory. An adaptive finite-volume method for a model of two-phase pedestrian flow. *Netw. Heterog. Media*, 6(3):401–423, 2011.

[16] F. Betancourt, R. Bürger, K. H. Karlsen, and E. M. Tory. On nonlocal conservation laws modelling sedimentation. *Nonlinearity*, 24(3):855–885, 2011.

[17] J. Bick and G. F. Newell. A continuum model for two-directional traffic flow. *Q. Appl. Math.*, XVIII(2):191–204, 1960.

[18] S. Blandin and P. Goatin. Well-posedness of a conservation law with non-local flux arising in traffic flow modeling. *Numerische Mathematik*, pages 1–25, 2015.

[19] V. Blue and J. Adler. Emergent fundamental pedestrian flows from cellular automata microsimulation. *Transportation Research Record: Journal of the Transportation Research Board*, 1644:29–36, 1998.

[20] A. Bressan. *Hyperbolic systems of conservation laws*, volume 20 of *Oxford Lecture Series in Mathematics and its Applications*. Oxford University Press, Oxford, 2000. The one-dimensional Cauchy problem.

[21] G. Bretti and B. Piccoli. A tracking algorithm for car paths on road networks. *SIAM J. Appl. Dyn. Syst.*, 7(2):510–531, 2008.

[22] S. Buchmüller and U. Weidmann. Parameters of pedestrians, pedestrian traffic and walking facilities. Technical report, ETH Zürich, 2006.

[23] M. Burger, M. Di Francesco, P. A. Markowich, and M.-T. Wolfram. Mean field games with nonlinear mobilities in pedestrian dynamics. *Discrete Contin. Dyn. Syst. Ser. B*, 19(5):1311–1333, 2014.

[24] J. A. Carrillo, R. M. Colombo, P. Gwiazda, and A. Ulikowska. Structured populations, cell growth and measure valued balance laws. *J. Differential Equations*, 252(4):3245–3277, 2012.

[25] J. A. Carrillo, S. Martin, and M.-T. Wolfram. A local version of the Hughes model for pedestrian flow. *accepted for publication at M3AS*, Jan. 2015.

[26] R. M. Colombo, M. Garavello, and M. Lécureux-Mercier. A class of nonlocal models for pedestrian traffic. *Math. Models Methods Appl. Sci.*, 22(4):1150023, 34, 2012.

[27] R. M. Colombo, P. Goatin, and M. D. Rosini. On the modelling and management of traffic. *ESAIM: M2AN*, 45(5):853–872, 2011.

[28] R. M. Colombo, M. Herty, and M. Mercier. Control of the continuity equation with a non local flow. *ESAIM Control Optim. Calc. Var.*, 17(2):353–379, 2011.

[29] R. M. Colombo and M. Lécureux-Mercier. Nonlocal crowd dynamics models for several populations. *Acta Mathematica Scientia*, 32(1):177 – 196, 2012.

[30] R. M. Colombo and M. D. Rosini. Pedestrian flows and non-classical shocks. *Mathematical Methods in the Applied Sciences*, 28(13):1553–1567, 2005.

[31] M. G. Crandall and A. Majda. The method of fractional steps for conservation laws. *Numer. Math.*, 34(3):285–314, 1980.

[32] M. G. Crandall and A. Majda. Monotone difference approximations for scalar conservation laws. *Math. Comp.*, 34(149):1–21, 1980.

[33] E. Cristiani, B. Piccoli, and A. Tosin. *Multiscale Modeling of Pedestrian Dynamics*, volume 12 of *MS&A*. Springer, 2014.

[34] C. M. Dafermos. Polygonal approximations of solutions of the initial value problem for a conservation law. *Journal of Mathematical Analysis and Applications*, 38(1):33 – 41, 1972.

[35] M. Di Francesco, P. A. Markowich, J.-F. Pietschmann, and M.-T. Wolfram. On the Hughes' model for pedestrian flow: the one-dimensional case. *J. Differential Equations*, 250(3):1334–1362, 2011.

[36] R. J. DiPerna. Measure-valued solutions to conservation laws. *Arch. Rational Mech. Anal.*, 88(3):223–270, 1985.

[37] C. Dogbe. On the modelling of crowd dynamics by generalized kinetic models. *Journal of Mathematical Analysis and Applications*, 387(2):512 – 532, 2012.

[38] R. Eftimie. Hyperbolic and kinetic models for self-organized biological aggregations and movement: a brief review. *J. Math. Biol.*, 65(1):35–75, 2012.

[39] N. El-Khatib, P. Goatin, and M. Rosini. On entropy weak solutions of hughes' model for pedestrian motion. *Zeitschrift für angewandte Mathematik und Physik*, 64(2):223–251, 2013.

[40] R. Eymard, T. Gallouët, and R. Herbin. Finite volume methods. In *Handbook of numerical analysis, Vol. VII*, Handb. Numer. Anal., VII, pages 713–1020. North-Holland, Amsterdam, 2000.

[41] A. D. Fitt. The numerical and analytical solution of ill-posed systems of conservation laws. *Appl. Math. Modelling*, 13(11):618–631, 1989.

[42] U. S. Fjordholm, R. Käppeli, S. Mishra, and E. Tadmor. Construction of approximate entropy measure valued solutions for hyperbolic systems of conservation laws. Technical report, ETH Zürich, 2014.

[43] H. Frid and I.-S. Liu. Oscillation waves in Riemann problems inside elliptic regions for conservation laws of mixed type. *Z. Angew. Math. Phys.*, 46(6):913–931, 1995.

[44] A. Friedman. Conservation laws in mathematical biology. *Discrete Contin. Dyn. Syst.*, 32(9):3081–3097, 2012.

[45] E. Godlewski and P.-A. Raviart. *Hyperbolic systems of conservation laws*. Mathématiques et applications. Ellipses, Paris, 1991.

[46] S. K. Godunov. A difference method for numerical calculation of discontinuous solutions of the equations of hydrodynamics. *Mat. Sb. (N.S.)*, 47 (89):271–306, 1959.

[47] S. Göttlich, A. Klar, and S. Tiwari. Complex material flow problems: a multi-scale model hierarchy and particle methods. *Journal of Engineering Mathematics*, 92(1):15–29, 2015.

[48] P. Gwiazda, T. Lorenz, and A. Marciniak-Czochra. A nonlinear structured population model: Lipschitz continuity of measure-valued solutions with respect to model ingredients. *J. Differential Equations*, 248(11):2703–2735, 2010.

[49] D. Helbing. A fluid-dynamic model for the movement of pedestrians. *Complex Systems*, 6:391–415, 1992.

[50] D. Helbing and P. Molnar. Social force model for pedestrian dynamics. *Physical review E*, 51(5):4282, 1995.

[51] D. Helbing, P. Molnár, I. J. Farkas, and K. Bolay. Self-organizing pedestrian movement. *Environment and Planning B*, 28(3):361–383, 2001.

[52] L. Henderson. On the fluid mechanics of human crowd motion. *Transportation Research*, 8:509–515, 1974.

[53] H. Holden, L. Holden, and N. H. Risebro. Some qualitative properties of 2×2 systems of conservation laws of mixed type. In *Nonlinear evolution equations that change type*, volume 27 of *IMA Vol. Math. Appl.*, pages 67–78. Springer, New York, 1990.

[54] H. Holden and N. H. Risebro. *Front tracking for hyperbolic conservation laws*, volume 152 of *Applied Mathematical Sciences*. Springer-Verlag, New York, 2002.

[55] L. Huang, S. C. Wong, M. Zhang, C.-W. Shu, and W. H. K. Lam. Revisiting Hughes' dynamic continuum model for pedestrian flow and the developement of an efficient solution algorithm. *Transpn. Res.–B*, 43(1):127–141, 2009.

[56] R. L. Hughes. A continuum theory for the flow of pedestrians. *Transpn. Res.–B*, 36(6):507–535, 2002.

[57] R. L. Hughes. The flow of human crowds. In *Annual review of fluid mechanics, Vol. 35*, volume 35 of *Annu. Rev. Fluid Mech.*, pages 169–182. Annual Reviews, Palo Alto, CA, 2003.

[58] E. Isaacson, D. Marchesin, B. Plohr, and B. Temple. The Riemann problem near a hyperbolic singularity: the classification of solutions of quadratic Riemann problems. I. *SIAM J. Appl. Math.*, 48(5):1009–1032, 1988.

[59] Y. Jiang, T. Xiong, S. C. Wong, C.-W. Shu, M. Zhang, P. Zhang, and W. H. K. Lam. A reactive dynamic continuum user equilibrium model for bi-directional pedestrian flows. *Acta Math. Sci. Ser. B Engl. Ed.*, 29(6):1541–1555, 2009.

[60] K. H. Karlsen and J. D. Towers. Convergence of the Lax-Friedrichs scheme and stability for conservation laws with a discontinous space-time dependent flux. *Chinese Ann. Math. Ser. B*, 25(3):287–318, 2004.

[61] B. L. Keyfitz. A geometric theory of conservation laws which change type. *Z. Angew. Math. Mech.*, 75(8):571–581, 1995.

[62] B. L. Keyfitz. Singular shocks: retrospective and prospective. *Confluentes Math.*, 3(3):445–470, 2011.

[63] S. N. Kružkov. First order quasilinear equations with several independent variables. *Mat. Sb. (N.S.)*, 81 (123):228–255, 1970.

[64] G. Le Bon. *Psychologie des foules.* Alcan, 1895.

[65] R. J. LeVeque. *Numerical methods for conservation laws.* Lectures in mathematics : ETH Zürich. Birkhäuser, Basel, Boston, Berlin, 1992. Autres tirages : 1994, 1999, 2006, 2008.

[66] M. J. Lighthill and G. B. Whitham. On kinematic waves. II. A theory of traffic flow on long crowded roads. *Proc. Roy. Soc. London. Ser. A.*, 229:317–345, 1955.

[67] T. P. Liu. The Riemann problem for general 2×2 conservation laws. *Trans. Amer. Math. Soc.*, 199:89–112, 1974.

[68] B. Maury, A. Roudneff-Chupin, and F. Santambrogio. A macroscopic crowd motion model of gradient flow type. *Math. Models Methods Appl. Sci*, 20(10):1787–1821, 2010.

[69] M. Moussaïd, E. G. Guillot, M. Moreau, J. Fehrenbach, O. Chabiron, S. Lemercier, J. Pettré, C. Appert-Rolland, P. Degond, and G. Theraulaz. Traffic instabilities in self-organized pedestrian crowds. *PLoS Comput. Biol.*, 8(3):e1002442, 2012.

[70] S. Okazaki. A study of pedestrian movement in architectural space, part 1: pedestrian movement by the application of magnetic model. *Trans. A.I.J.*, 283:111–119, 1979.

[71] S. Okazaki. A study of pedestrian movement in architectural space, part 2: concentrated pedestrian movement. *Trans. A.I.J.*, 284,:101–110, 1979.

[72] S. Okazaki. A study of pedestrian movement in architectural space, part 3: along the shortest path, taking fire, congestion and unrecognized space into account. *Trans. A.I.J.*, 285:137–147, 1979.

[73] S. Okazaki and S. Matsushita. A study of pedestrian movement in architectural space, part 5: a probing walk and a guide walk by a guideboard. *Trans. A.I.J.*, 299:105–113, 1981.

[74] S. Okazaki and C. Yamamoto. A study of pedestrian movement in architectural space, part 4: pedestrian movement represented in perspective. *Trans. A.I.J.*, 302:87–93, 1981.

[75] J. Reilly, S. Samaranayake, M. Delle Monache, W. Krichene, P. Goatin, and A. Bayen. Adjoint-based optimization on a network of discretized scalar conservation laws with applications to coordinated ramp metering. *Journal of Optimization Theory and Applications*, pages 1–28, 2015.

[76] P. I. Richards. Shock waves on the highway. *Operations Res.*, 4:42–51, 1956.

[77] V. V. Rusanov. The calculation of the interaction of non-stationary shock waves with barriers. *Ž. Vyčisl. Mat. i Mat. Fiz.*, 1:267–279, 1961.

[78] R. Sanders. On convergence of monotone finite difference schemes with variable spatial differencing. *Math. Comp.*, 40(161):91–106, 1983.

[79] P. Schindler. *Continuous Modeling and Optimization Approaches for Manufacturing Systems.* Dipl.-math, Mannheim University, February 4 2014. PhD Thesis.

[80] H. B. Stewart and B. Wendroff. Two-phase flow: models and methods. *J. Comput. Phys.*, 56(3):363–409, 1984.

[81] L. Tartar. Compensated compactness and applications to partial differential equations. In *Nonlinear analysis and mechanics: Heriot-Watt Symposium, Vol. IV*, volume 39 of *Res. Notes in Math.*, pages 136–212. Pitman, Boston, Mass.-London, 1979.

[82] A. Tikhonov and A. Samarskii. Homogeneous difference schemes on non-uniform nets. *USSR Computational Mathematics and Mathematical Physics*, 2(5):927 – 953, 1963.

[83] J. D. Towers. Convergence of a difference scheme for conservation laws with a discontinuous flux. *J. Numer. Anal.*, 38(2):681–698, 2000.

[84] V. Vinod. *Structural stability of Riemann solutions for a multiple kinematic conservation law model that changes type.* PhD thesis, University of Houston, Houston, Texas, 1992. PhD Thesis, 77204-3476.

[85] W. J. Yu, R. Chen, L. Y. Dong, and S. Q. Dai. Centrifugal force model for pedestrian dynamics. *Phys. Rev. E*, 72:026112, Aug 2005.

[86] H. Zhao. A fast sweeping method for eikonal equations. *Math. Comp.*, 74(250):603–627 (electronic), 2005.